TEL AVIV UNIVERSITY

THE IBY AND ALADAR FLEISCHMAN FACULTY OF ENGINEERING

The Zandman-Slaner Graduate School of Engineering

HIGH POWER, STABLE AND EFFICIENT OPERATION OF AN ELECTROSTATIC ACCELERATOR FREE-ELECTRON LASER

By

Mark Volshonok

THESIS SUBMITTED FOR THE DEGREE OF “DOCTOR OF PHILOSOPHY”

SUBMITTED TO THE SENATE OF TEL-AVIV UNIVERSITY

May 2011

THE IBY AND ALADAR FLEISCHMAN FACULTY OF ENGINEERING
The Zandman-Slaner Graduate School of Engineering

HIGH POWER, STABLE AND EFFICIENT OPERATION OF AN ELECTROSTATIC ACCELERATOR FREE-ELECTRON LASER

By

Mark Volshonok

THESIS SUBMITTED FOR THE DEGREE OF "DOCTOR OF PHILOSOPHY"
SUBMITTED TO THE SENATE OF TEL-AVIV UNIVERSITY

This Research Work was Carried Out at Tel-Aviv University
In The Faculty of Engineering

Under The Supervision of Prof. Avraham Gover

May 2011

This research work was carried out at

Tel-Aviv University

in the **Faculty of Engineering**

under the supervision of

Prof. **Avraham Gover**

Acknowledgements

My first debt of gratitude is to my supervisor Prof. Avraham Gover who was a constant source of guidance and support. It was a privilege to work with so distinguished a scientist as Prof. Gover, whose contribution to the field was recognized in 2005 when he won the FEL prize. Prof. Gover was the driving force behind this research.

Arie Eichenbaum assisted in the English editing of this thesis, for which I wish to express my sincere thanks.

Finally I would like to acknowledge the immeasurable patience and support of my wife Mariane.

Abstract

Theoretical and experimental studies of the Israeli Electrostatic Accelerator Free electron laser (EA FEL) operation are reported in this dissertation.

This work starts with an historical survey of FEL's and subsequently relates to the EA FEL of Tel-Aviv University. The thesis includes detailed theoretical and experimental investigations of the EA-FEL parts: the electron injector (low energy section), electrostatic accelerator (high energy) section, decelerator section and the electron collector.

The electron beam transport of the EA-FEL in its various sections is simulated and analyzed by use of several simulation codes, in order to find the operating parameters permitting optimal electron beam transport through the entire FEL beam line. The results of the simulations were found to be in good agreement with to the experimental results. Several improvements in the electron beam transport simulation codes are proposed so as to make them more efficient in their use. The influence of the quality of electron beam transport on the FEL gain, power and lasing frequency was determined and will be described.

We describe experimental work and measurements made on the EA-FEL with 2kG wiggler and especially those that are related to the 45kV/2A electron gun, and the electron optic elements in the low and high energy sections. Measurements of the stray magnetic fields in the injector, section were performed; these were used in order to repair the trajectories of the beam in the injector thereby improving electron beam transport into the accelerator.

Further describe investigations and measurements on electron beam transport were carried out in the accelerator itself. In particular, the emittance of $3\pi\cdot$mm$\cdot$mrad was measured. We investigated the effects of the beam transport quality parameters on the spontaneous and stimulated emission of FEL radiation.

We also made theoretical and experimental investigations of the mode competition process and the conditions for single mode operation considering the variations in electron beam energy during the lasing pulse. The power or 900W at 97.2GHz was measured, as well as the spectrum of the single mode laser radiation such beam energy change was measured and the experimental results were compared to those predicted by simulations. The frequency tunability range of the Israeli EA-FEL and the frequency sweep (chirp) during the pulse duration were also measured in 80-110 GHz range. The dependence of the effects on the terminal voltage droop rate was evaluated and compared to simulation results

A number of suggestions are made for enhancement of the FEL radiation output power via improvements in electron beam transport, and via a process of “voltage ramping” in the high voltage section during the FEL saturation stage. Use of the Israeli EA-FEL with controlled high voltage ramping (in order to obtain a desired chirp rate) for spectroscopic applications is proposed.

Contents

Symbols

A_{em}	Electron cross section area
a_w	Wiggler parameter
$\boldsymbol{B}$	Magnetic field vector
B_w	Wiggler magnetic field amplitude
C_q	Field amplitude of q^{th} mode
c	Speed of light velocity in free space
$\boldsymbol{E}$	Magnetic field vector
E_k	Electron energy
F	Force
f	Frequency
f_{co}	Waveguide cutoff frequency
J	Electric current density
I	E-beam current
k	Wavenumber in free space
k_w	Wiggler wavenumber
k_β	Betatron wavenumber
m	Electron mass
P	Total electromagnetic power
R	Power reflectivity
r	The (x, y, z) coordinates
T	Power transmission coefficient
T	Time
V	Voltage
v_w	Wiggling velocity
v_{z0}	Electron axial velocity
x	Coordinate
y	Coordinate
Z	Mode impedance
z	Coordinate

Greek Letters

β	Relativistic factor
γ	Lorentz relativistic factor
θ	Detuning parameter
λ	Radiation wavelength
λ_w	Wiggler wavelength
μ	Permeability
τ	Slippage time
ω	Angular frequency

Acronyms

C	Coil
CT	Collector tube
EA	Electrostatic accelerator
FEL	Free electron laser
FEM	Free electron maser
HV	High voltage
IF	Intermediate frequency
LO	Local oscillator
Q	Quadrupol
RF	Radio frequency
S	Screen
TAU	Tel-Aviv University

List of Figures

List of Tables

Chapter 1 Introduction

The Free Electron Lasers (FEL) is a device that converts the kinetic energy of the free (unbound) electrons to electromagnetic radiation. FELs are high power tunable, coherent sources of electromagnetic radiation currently spanning wavelengths from microwaves and millimeter to ultraviolet lights wave and to X-rays. The FEL has properties of conventional laser such as high temporal and spatial coherence. It differs from conventional lasers by employing an electron beam as gain medium, instead of excited atomic states. FELs are characterized by high efficiency operation compared to conventional laser. By proper design, using an electron beam energy retrieval scheme, such as “depressed collector”, it may be possible to obtain high efficiency (over 50%). These features make the FEL an appropriate radiation source for a variety of scientific, technological, industrial and medical applications.

The research goal of this thesis was to study the performance of quasi-cw EA-FEL's. For this goal are used an existing electrostatic FEL facility, that was constructed earlier by researches from Tel-Aviv University and Ariel university center, based on Van-der-Graaf Weizmann Institute tandem EA accelerator, which was converted earlier into an electron accelerator with depressed collector configuration.

In the following chapters the characteristics of this accelerator and the FEL are described, including design, simulations and measurements of the e-beam transport and study of the FEL radiation characteristics and coherent properties.

1.1 Historical Survey of Radiation Devices and Free Electron Lasers

The term "Free Electron Laser" was coined by John Madey in 1971 (Madey 1971), pointing out that the radiative transitions of the electrons in this device are between free space (more correctly – unbound) electron quantum states, which are therefore states of continuous energy. This is in contrast to conventional atomic and molecular lasers, in which the electron performs radiative transition between bound (and therefore of distinct energy) quantum states. Based on these theoretical observations, Madey and his colleagues in Stanford University demonstrated FEL operation first as an amplifier (at λ= 10.6 μm) in 1976 and subsequently as an oscillator (at λ= 3.4 μm) in 1980.

From the historical point of view (Gover 2004) it turned out that Madey's invention was essentially an extension of a former invention in the field of microwave-tubes technology- *the Ubitron*. The Ubitron, a mm-wave electron tube amplifier based on a magnetic undulator, was invented and developed by Philips and Enderbry who operated it at high power levels in 1960. The early Ubitron development activity was not noticed by the FEL developers because of the disciplinary gap, and largely because its research was classified at the time. Renewed interest in high power mm-wave radiation emission started in the 1970's, triggered by the development of pulsed-line generators of "*Intense Relativistic Beams*" (IRB). This activity, led primarily by plasma-physicists in the defense establishment laboratories of Russia (mostly IAP in Gorky- Nizhny Novgorod) and the U.S. (mostly N.R.L. – DC), led to development of high gain high power mm-wave sources independently of the development of the optical FEL. The connection between these devices and between them to conventional microwave tubes (as Traveling Wave Tube – TWT) and other electron beam radiation schemes (like Cerenkov and Smith-Purcell Radiation), that may also be considered "Free Electron Lasers", was revealed in the mid-seventies, starting with the theoretical works of P. Spangle, A. Gover, A. Yariv, who identified that all these devices satisfy the same dispersion equation as the TWT derived by John Pierce in the fourties. Thus the optical FEL could be conceived as a kind of immense electron-tube, operating with a high energy electron beam in the low gain regime of the Pierce TWT dispersion equation.

The extension of the low-gain FEL theory to the general "electron-tube" theory is important because it led to development of new radiation schemes and new operating regimes of the optical FEL. This was exploited by physicists in the discipline of Accelerator Physics and Synchrotron Radiation, who identified, starting with the theoretical works of the groups of C. Pellegrini and R. Bonifacio in the early eighties that high current high quality electron beams, attainable with further development of accelerators technology, could make it possible to operate FELs in the high gain regime even at short wavelengths (Vacuum Ultra-Violet – VUV and soft X-ray), and that the high gain FEL theory can be extended to include amplification of the incoherent synchrotron spontaneous emission (shot noise) emitted by the electrons in the undulator. This led to the important development of the “Self (Synchrotron) Amplified Spontaneous Emission (SASE) FEL”, which promises to be an extremely high brightness radiation source, overcoming the fundamental obstacles of X-ray lasers development: lack of mirrors (for oscillators) and lack of high brightness radiation sources (for amplifiers).

A big boost to the development of FEL technology was given in the period of the American “Strategic Defence Initiative – SDI” (“Star-War”) program in the mid-eighties. The FEL was considered one of the main candidates for use in a ground-based or space-based “Directed Energy Weapon – DEW”, that can deliver Megawatts of optical power to hit attacking missiles. The program led to heavy involvement of major American Defence establishment laboratories (Lawrence–Livermore National Lab, Los-Alamos National Lab) and contracting companies (TRW,Boeing). Some of the outstanding results of this effort were the demonstration of high gain operation of an FEL amplifier in the mm-wavelength regime, utilizing an Induction Linac atLivermore 1985, and demonstration of enhanced radiative energy extraction efficiency in FEL oscillator, using a “tapered wiggler” in an RF–Linac driven FEL oscillator atLos-Alamos 1983. The program has not been successful in demonstrating the potential of FELs to operate at high average power levels needed for DEW applications. But after the cold war period, a small part of the program continues to support research and development of medical FEL application.

1.2 Free Electron Lasers

1.2.1 Principles of operation

Fig. 1.1 displays schematically a FEL oscillator. It is composed of three main parts: An electron accelerator, a magnetic wiggler (or undulator) and an optical resonator.

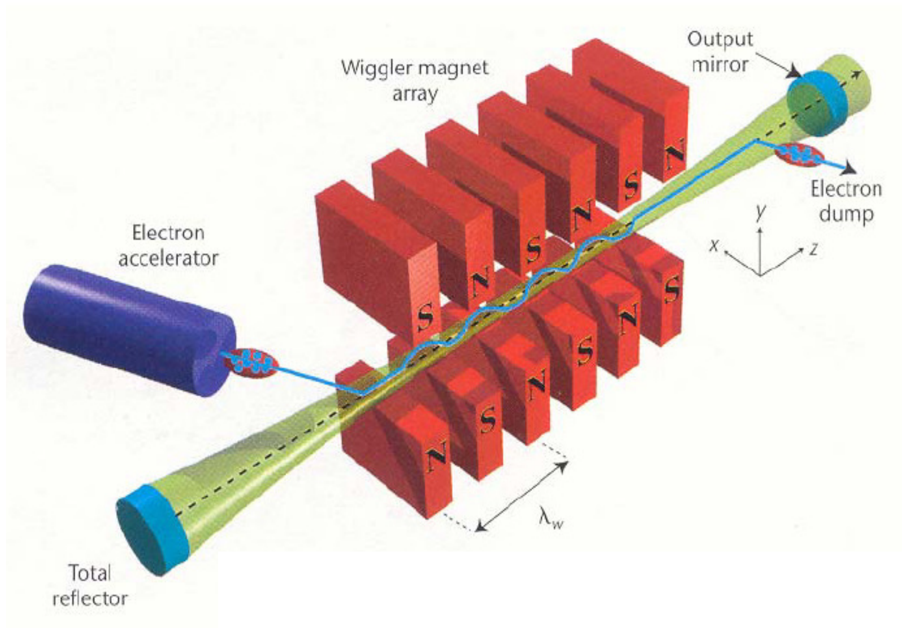

Fig.1.1 Components of a FEL oscillator (C.V. Benson Optics & Photonics News May 2003 – Illustration by Jaynie Martz)

Basically an FEL amplifier is composed of an accelerated electron beam traversing through a periodic magnetic structure called undulator or wiggler. An oscillator includes also two reflectors that provide feedback. Electrons are derived from an electron gun such as a thermionic cathode e-gun or a photo-cathode e-gun. The electrons are injected into an accelerator and are accelerated to high energy. The gun and the electron accelerator generate an electron beam of high energy and high beam quality which is then injected into the magnetic “wiggler” having period λ_w.

As electrons travel along the wiggler their motion is affected by the magnetic field of the wiggler causing them to oscillate transversely with a wave number $k_w = 2\pi/\lambda_w$ and angular frequency of $k_w v_{z0}$, where v_{z0} is the average velocity of the electrons in the axial (z) direction.

The oscillation motion of the electrons is perpendicular to the direction of propagation (z – axis), constituting a radiating dipole in motion. The radiation emitted by the fast transverse and oscillating electron beam is known as *Undulator Synchrotron Radiation* (Motz H. and Whitehurst R. 1953) and it is directed mainly in the forward direction if the electron velocity is relativistic (Jacson J. 1962). The power of Undulator Synchrotron Radiation is proportional to the number of electrons in the beam; the radiation wavelength in free space in the forward direction is given by following equation 1.4 for $\theta = 0$:

$$\lambda = \frac{\lambda_w}{\beta_{z0}(1+\beta_{z0})\gamma_{z0}^2} \tag{1.1}$$

where $\beta_{z0} = \frac{v_{z0}}{c}$ and $\gamma_{z0} = \frac{1}{\sqrt{1-\beta_{z0}^2}}$.

And for a planar wiggler (Gover A., et al 1984)

$$\gamma_{z0} = \frac{\gamma}{\sqrt{1+a_w^2/2}} \tag{1.2}$$

Where a_w - (also termed K)*"the wiggler parameter"* is the normalized transverse momentum:

$$a_w = \frac{eB_w}{k_w mc} = 0.093 B_w [\text{KGauss}] \lambda_w [\text{cm}] \tag{1.3}$$

Where B_w is amplitude of the magnetic field.

In Undulator Synchrotron Radiation the electrons enter the wiggler randomly. Each emits a coherent wave packet, and radiation packets from different electrons add up in energy and form a radiation beam which is partially coherent (spontaneous emission). In order to obtain coherent stimulated emission, an external radiation signal should be inserted into the interaction region at frequency near the frequency of spontaneous emission (1.1). The transverse field components of the inserted radiation field and the wiggler magnetic field produce a *pondermotive* force wave (Grananshtain V.L. and Alexoff I. 1987), which is an axial force bi-linear in the wiggler and radiation fields. The pondermotive wave has the same frequency as the radiation wave and wave number k_z+k_w (k_z is the axial wave number of the radiation mode). The pondermotive wave is responsible for an electron bunching process. Contrary to the incoherent spontaneous emission process the electrons get periodically bunched along the interaction region, and radiate at the same frequency and phase as the inserted radiation field that produces the bunching. In order to guarantee a continuous interaction along the wiggler between the pondermotive wave and the electrons and extraction of energy from electrons to the pondermotive wave, the electrons must be synchronized with the pondermotive wave through their flight along the wiggler. A measure of synchronism between the electrons and the pondermotive wave is given by the detuning parameter θ:

$$\theta \equiv \frac{\omega}{v_{z0}} - \left[k_z(\omega) + k_w\right] \tag{1.4}$$

At synchronism $\theta=0$ $\left(\mathrm{v}_{z0} = \omega/(\mathrm{k}_z + \mathrm{k}_w)\right)$. This conditions leads to the radiation wavelength expression (1.1) for the case of free-space propagation $(\mathrm{k} = \omega/\mathrm{c})$. However at exact synchronism there is no net energy exchange between the e-beam and the wave.

If the pondermotive wave is slightly slower than the electron velocity (i.e. the detuning parameter $\theta \leq 0$), electrons lose energy to the wave. As a result, the field amplitude of the electromagnetic eave grows and amplification (stimulated emission) occurs. For the case where $\theta \geq 0$, the field amplitude of the radiation wave decays and its energy is transferred to the electron beam, resulting in acceleration of electrons.

Fig. 1.2 displays the operating wavelengths of FEL projects all over the world vs. their e-beam energy. FELs were operated or planned to operate over a wide range of frequencies, from the microwave to X-ray – eight orders of magnitude. The data points fall on the theoretical FEL radiation curve (1.1, 1.2).

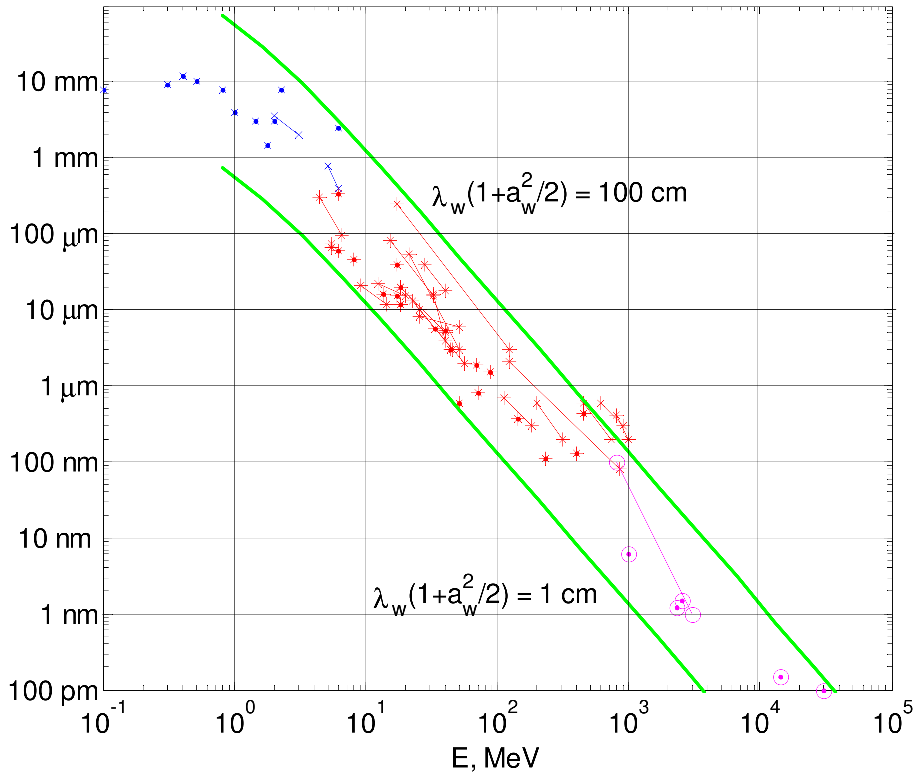

Fig. 1.2 Operating wavelengths of FELs around the world vs. their accelerator beam energy. The data points correspond in ascending order of accelerator energy to the following experimental facilities: NRL (USA), IAP (Russia), KAERI (Korea), IAP (Russia), JINR/IAP (Russia), INP/IAP (Russia), TAU (Israel), FOM (Netherlands), KEK/JAERI (Japan/Korea), CESTA (France), ENEA (Italy), KAERI-FEL (Korea), LEENA (Japan), ENEA (Italy), FIR FEL (USA), mm Fel (USA), UCSB (USA), ILE/ILT (Japan), MIRFEL (USA), UCLA-Kurchatov (USA/Russia), FIREFLY (GB), JAERI-FEL (Japan), FELIX (Netherlands), RAFEL (USA), ISIR (Japan), UCLA-Kurchatov-LANL (USA/RU), ELSA (France), CLIO (France), SCAFEL (GB), FEL (Germany), BFEL (China), KHI-FEL (Japan), FELI4 (Japan), iFEL1 (Japan), HGHG (USA), FELI (USA), MARKIII (USA), ATF (USA), iFEL2 (Japan), VISA (USA), LEBRA (Japan), OK-4 (USA), UVFEL (USA), iFEL3 (Japan), TTF1 (Germany), NIJI-IV (Japan), APSFEL (USA), FELICITAI (Germany), FERMI (Italy), UVSOR (Japan), Super-ACO (France), TTF2 (Germany), ELETTRA (Italy), Soft X-ray (Germany), SPARX (Italy), LCLS (USA), TESLA (Germany). X- long wavelengths, *-short wavelengths, circles – planned short wavelengths SASE-FELs. Data based in part on H. P. Freund, V. L. Granatstein, Nucl. Inst. and Methods In Phys. Res. A249, 33 (1999), W. Colson, Proc. of the 24th Int. FEL conference, Argone, Ill. (ed. K. J. Kim, S. V. Milton, E. Gluskin).

1.2.2 Classification of accelerators for Free Electron Lasers

The kind of accelerator used, is the most important factor in determining the FEL characteristics. Evidently, the higher the acceleration energy, the shorter is the FEL radiation wavelength. However, not only the acceleration beam energy determines the shortest operating wavelength of the FEL, but also the e-beam quality. If the accelerated beam has large energy spread or energy instability or large emittance (the product of the beam width with its angular spread), then it may have large axial velocity spread v_{z0}. This may prevent operating the FEL at high frequencies.

Other parameters of the accelerator determine different characteristics of the FEL. High current in the electron beam enables higher gain and higher power operation. The e-beam pulse shape (or CW) characteristics, affect, of course, the emitted radiation waveform, and may also affect the FEL gain and saturation characteristics. The following are the main accelerator technologies used for FEL construction. Their wavelength operating-regimes (1.1) (determined primarily by their beam acceleration energies) are displayed in Fig. 1.3.

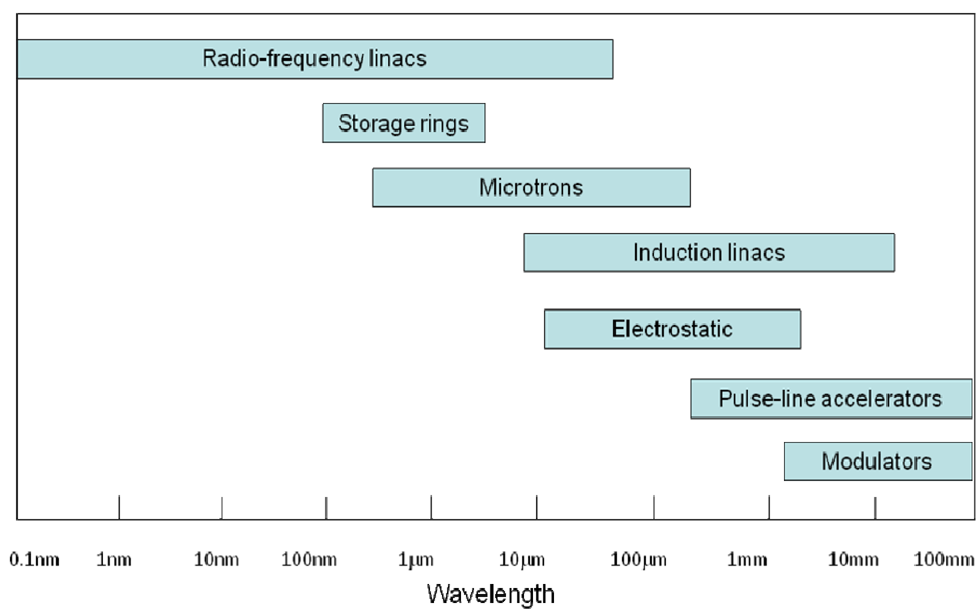

Fig. 1.3: Approximate wavelength ranges accessible with FELs based on current accelerator and wiggler technologies (based on H.P. Freund and T.M. Antonsen Jr.)

1) Modulators and Pulse-line Accelerators

These are usually single pulse accelerators, based on high voltage power supplies and fast discharge stored electric energy systems (e.g. Marx Generator), which produce short pulse (tens of nSec) *Intense Relativistic Beam (IRB)* of energy in the range of hundreds of keV to few MeV and high instantaneous current (order of kAmp), using explosive cathode (plasma field emission) electron guns. FELs (FEMs) based on such accelerators operated mostly in the microwave and mm-wave regimes. Because of their poor beam quality and single pulse characteristic, these FELs were, in most cases, operated only as Self Amplified Spontaneous Emission Sources, producing intense radiation beams of low coherence at instantaneous power levels in the range of 1-100MW. Some of the early pioneering work on FEMs was done in the nineteen seventies and eighties in the US (NRL, Columbia Univ., MIT), Russia (IAP) and France (Echole Politechnique) based on this kind of accelerators.

2) Induction Linacs

These are also single pulse (or low repetition rate) accelerators based on induction of electromotive potential over an acceleration gap by means of an electric-transformer circuit. They can be cascaded to high energy, and produce short pulse (tens to hundreds of nSec) high current (up to 10kA) electron beams, with relatively high energy (MeV to tens of MeV). The interest in FELs based on this kind of accelerator technology stemed in the nineteen-eighties, primarily from the SDI program, for the propose of development of a Directed Energy Weapon (DEW) FEL. The main development of this technology took place on a 50MeV accelerator – ATA (for operating at 10μm wavelength) and a 3.5 MeV accelerator – ETA (for operating at 8mm wavelength). The latter experiment, operating in the high gain regime, demonstrated record-high power (1GW) and energy extraction efficiency (35%).

3) Radio-Frequency (RF) Accelerator

RF-accelerators are by far the most popular electron-beam sources for FELs. In RF accelerators, short electron beam bunches (bunch duration 1-10pSec) are accelerated by the axial field of intense RF radiation (frequency about 1GHz), which is applied in the acceleration cavities on the injected short e-beam bunches, entering in synchronization with the accelerating-phase of the RF periods. In Microtrons the electron bunches perform circular motion, and get incremental acceleration energy every time they re-enter the acceleration cavity. In RF-LINACs (Linear Accelerator) the electron bunches are accelerated in a sequence of RF cavities or a slow-wave structure, which keep an accelerating-phase synchronization of the traversing electron bunches along a long linear acceleration length. The bunching of the electrons, prior to the acceleration step, is traditionally performed by bunching RF-cavities and a dispersive magnet (chicane) pulse compression system. Recent development of mode-locked UV solid state laser sources makes it possible nowadays to attain excellent initial bunching (picoseconds and sub-picoseconds pulse durations with hundreds of Ampere peak current) using photocathode electron-gun injectors (often integrated with a short accelerating RF cavity section.

Common normal-cavity RF-LINACS have energies of tens of MeV to GeV. Their electron beam current waveforms are determined by the characteristics of the Klystrons that supply the acceleration RF power. Continous acceleration of e-beam bunches at RF frequency is not possible with normal-cavity RF accelerators, and usually the accelerated electron beam bunches are produced in macropulses of few tens of microsecond duration, which are generated at repetition rate of 10-1000 Hz. These characteristics of RF accelerators are fit to drive FEL oscillators in the IR to UV range, in which the bunches repetition frequency (equal or sub-harmonic of the accelerator RF frequency) is synchronized with the round-trip circulation frequency of the radiation pulses in the FEL resonator

The FEL small signal gain, must be large enough to build-up the radiation field in the resonator from noise to saturation well within the macropulse duration.

RF-Linacs are essential facilities in synchrotron radiation centers, used to inject electron beam current into the synchrotron storage ring accelerator from time to time. Because of this reason, many FELs based on RF-LINACs were developed in Synchrotron Centers, and provide additional coherent radiation sources to the synchrotron center radiation users.

4) Storage Rings

Storage rings are circular accelerators in which a number of electron (or positron) beam bunches (typically of 50-500pS pulse duration and hundreds of Amper peak current) are circulated continuously by means of a lattice of bending magnets and quadrupole lenses. Typical energies of storage ring accelerators are in the hundreds of MeV to GeVs range. As the electrons pass through the bending magnets, they lose small amount of their energy due to emission of synchrotron radiation. This energy is replenished by a small RF acceleration cavity placed in one section of the ring. The electron beam bunch dimensions, energy spread and emittance parameters are set in steady state by a balance between the electrons oscillations within the ring lattice and radiation damping due to the random synchrotron emission process. This produces high quality (small emittance and energy spread) continuous train of electron beam bunches, that can be used to drive a FEL oscillator placed as an insertion device in one of the straight sections of the ring between two bending magnets.

Demonstrations of FEL oscillators, operating in a storage ring, were first reported by the French (LURE-Orsay) in 1987 (at the visible wavelength) and the Russians (VEPP-Novosibirsk) in 1988 (at the Ultra-violet). The short wavelength operation of storage-ring FELs is facilitated by the high energy and low emittance and energy spread parameters of the beam.

Since storage ring accelerators are at the heart of all synchrotron radiation centers, one could expect that they would be abounded in such facilities as inserted devices. There is, however, a problem of mutual interference between the FEL operation as an insertion device in the ring and the normal operation of the ring itself. The energy spread increase induced in the electron beam during interaction with the stored radiation in a saturated FEL oscillator cannot be controlled by the synchrotron radiation damping process, if the FEL operating power is too high. This limits the FEL power to be kept as a fraction of the synchrotron radiation power dissipation all around the ring (the “Renieri Limit”). Furthermore, the effect of the FEL on the e-beam quality, reduces the lifetime of the bunches in the storage ring and is distruptive to normal operation of the ring in a synchrotron radiation user facility.

To avoid the interference problems, it is most desirable to operate FELs in a dedicated storage ring. This also provides the option to leave long enough straight sections in which long enough wigglers provide sufficient gain for FEL oscillation

5) Superconducting (SC) RF-LINACS

When the RF cavities of the accelerator are superconducting, there are no RF power losses on the cavity walls, and it is possible to maintain continuous acceleration field in the RF accelerator with a moderate power continuous RF source, which delivers most of its power to the electron beam kinetic energy. Combining the SC-RF-LINAC technology with an FEL oscillator, pioneered primarily by Stanford University and Thomas Jefferson Lab (TJL) in the US and JAERI Lab in Japan, gave rise to an important scheme of operating such a system in a current recirculating energy retrieval mode. This scheme revolutionized the development of FELs in the direction of high power high efficiency operation, which is highly desirable, primarily for industrial applications (material processing, photochemical production etc.).

In the recirculating SC-RF-LINAC FEL scheme the wasted beam emerging out of the wiggler after losing a fraction of only few percents out of its kinetic energy, is not dumped into a beam-dump, as in normal cavity RF accelerators, but is re-injected, after circulation, into the SC-RF accelerator. The timing of the wasted electron bunches re-injection is such, that they experience a deceleration phase along the entire length of the accelerator cavities. Usually, they are re-injected at the same cell (RF period) with a fresh new electron bunch injected at an acceleration phase, and thus the accelerated fresh bunch receives its acceleration kinetic energy directly from the wasted beam bunch, that is at the same time decelerated. The decelerated wasted beam bunches are then dumped in the electron beam dump at much lower energy than without recirculation, at energies that are limited primarily just by the energy spread induced in the beam in the FEL laser-saturation process. This scheme not only increases many folds the over-all energy transformation efficiency from e-beam to radiation, but would solve significant heat dissipation and radioactivity activation problems in a high power FEL design.

The e-beam current recirculation scheme of SC-RF-LINAC FEL has a significant advantage over the e-beam recirculation in a storage ring. As in electrostatic accelerators, the electrons entering the wiggler are “fresh” cold-beam electrons from the injector, and not a wasted beam corrupted by the laser saturation process in a previous circulation through the FEL. This also makes it possible to sustain high average circulating current despite the disruptive effect of the FEL on the e-beam. This gave rise to a new concept for a radiation user facility light source-4GLS (fourth generation light source) which is presently in a pilot project development stage in Daresbury Lab in England. In such a scheme, IR and UV FEL oscillators and XUV SASE-FEL can be operated together with synchrotron magnet dipole and wiggler insertion devices without disruptive interference. Such a scheme, if further developed, can give rise to new radiation-user light-source facilities, which can provide a wider range of radiation parameters than synchrotron centers of previous generation.

6) Electrostatic Accelerators

These accelerators are DC machines, in which an electron beam, generated by a thermionic electron-gun (typically 1 – 10Amp) is accelerated electrostatically. The charging of the high voltage terminal can be done by mechanical charge transport (Van-der-Graaff) or electrodynamically (Crockford-Walton accelerator, Dynamitron). The first kind can be built at energies up to 25MeV, and the charging current is less than mAmp. The second kind have terminal voltage less than 5MeV, and the charging current can be hundreds of mAmps.

Because of their DC characteristics, FELs based on this kind of accelerators can operate at arbitrary pulse shape structure and in principle – continuously (CW). However, because of the low charging current, the high electron beam current (1-10Amp), required for FEL lasing must be transported without any interception along the entire way from the electron gun, through the acceleration tubes and the FEL wiggler, and then decelerated down to the voltage depressed beam-collector (multi-stage collector), closing the electric circuit back to the e-gun (current recirculation). The collector is situated at the e-gun potential, biased by moderate voltage high current power supplies, which deliver the current and power needed for circulating the e-beam and compensates for its kinetic energy loss in favor of the radiation field in the FEL cavity. This beam current recirculation is therefore also an *"Energy retrieval"* scheme, and can make the overall energy transfer efficiency of the Electrostatic-Accelerator FEL very high.

In practice, high beam transport efficiency in excess of 99.9% is needed for CW lasing, and has not been demonstrated yet. To avoid HV-terminal voltage drop during lasing, Electrostatic-Accelerator FELs are usually operated in a single pulse mode. Few FELs of this kind have been constructed over the world. The first and main facility is the UCSB FEL shown. It operates in the wavelength range of 30μm to 2.5mm (with three switchable wigglers) in the framework of a dedicated radiation user facility. This FEL operates in the negatively charged terminal mode, in which the e-gun and collector are placed in the negatively charged HV-terminal inside the pressurized insulating gas tank, and the wigglers are situated externally at ground potential. An alternative operating mode of positively charged terminal internal cavity Electrostatic Accelerator FEM was demonstrated in the Israeli Tandem–Accelerator FEM and the Dutch F.O.M. Fusion FEM projects. This configuration enables operating with long pulse, high coherence and very high average power. Linewidth of $\Delta\omega/\omega \cong 10^{-5}$ was demonstrated in the Israeli FEM and high power (730kW over few microseconds) was demonstrated in the Dutch FEM, both at mm-wavelengths. The goal of the latter development project (which was not completed) was quasi-continuous operation at 1 MW average power for application in fusion plasma heating.

Chapter 2 Description of the Israeli EA-FEL

This chapter describes all the parts of the Israeli EA-FEL. The low energy part (injector), is responsible for delivery of the electron beam to an accelerator section. The injector section includes an electron gun, focusing and steering coils and diagnostic screens. The high energy section includes a Van-der-Graaf electrostatic accelerator, which accelerates electrons up to an energy of about 1.4MeV, including focusing quadrupols and diagnostic screens, a wiggler, in which the undulating e-beam generates a millimeter wave radiation within a FEL resonator. The decelerator section and collector are responsible for electron beam energy recovery and for efficient FEL operation. The description of the injector section is supported by E-GUN (Herrmannsfeldt) code simulations. The electron beam propagation in the wiggler is described.

2.1 General description and schematic

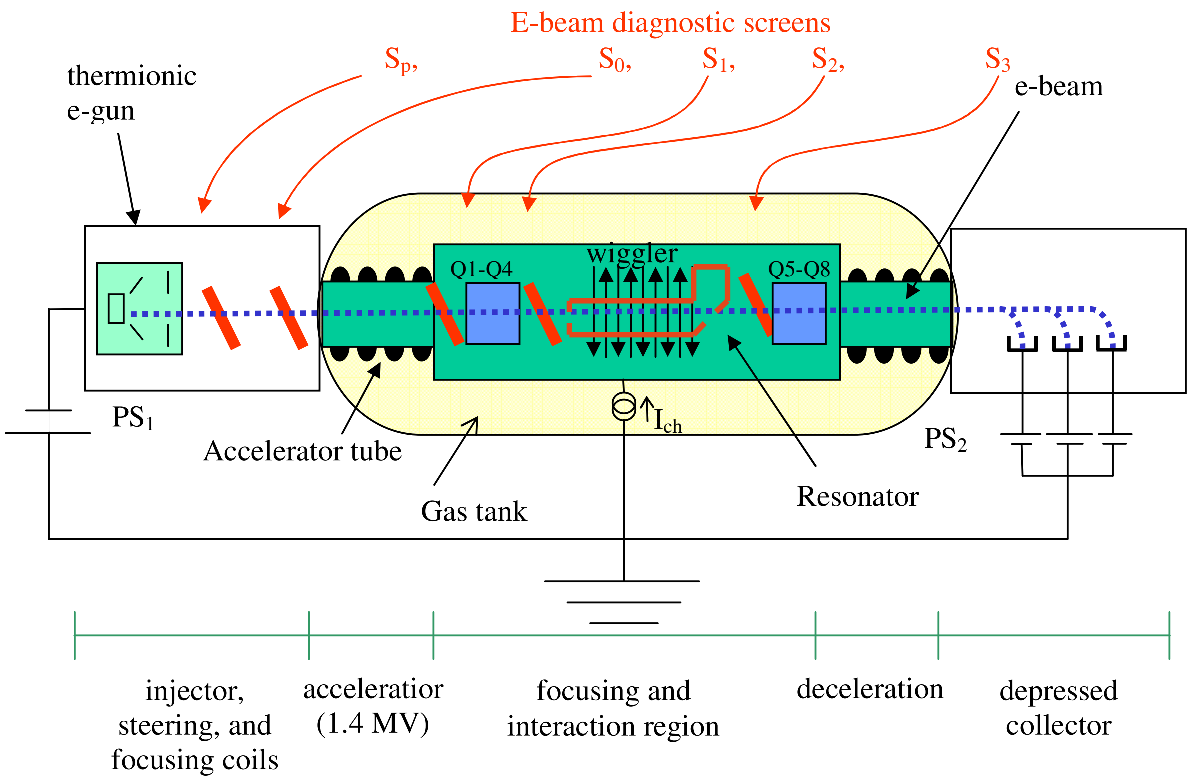

Fig.2.1 Scheme of the Israeli Electrostatic Accelerator FEL

The Israeli Tel-Aviv University Electrostatic Accelerator FEL (TAU EA-FEL) is based on a 6MeV Tandem Van-der-Graaf accelerator, which was originally used as an ion accelerator for nuclear physics experiments (Yakover et. al. 1996). In the present version of the FEL, the millimeter wave radiation generated in the resonator is separated from the electron beam by means of a perforated Talbot effect reflector (Kapelevich B et al. 2003, Gover A., et al. 1984). A quasi-optical delivery system transmits the out-coupled power through a window in the pressurized gas accelerator tank. Lasing was demonstrated first in August 2003.

The electron beam-line in the TAU Tandem FEL consists of 7 sections shown in Fig.2.1. The first section is the e-beam injector comprised of a 50 *keV* e-gun, focusing and steering coils, and two diagnostic screens S_P, and S_0. This is followed by a second section:

1.0-3.0 *MeV* electrostatic acceleration tube. The third section includes a diagnostic screen S_1 and four quadrupoles Q1 to Q4 for e-beam focusing before the beam enters the wiggler. The central section is the high voltage terminal charged by a current I_{ch} usually limited to several hundreds of μAmps; in this section, a waveguide resonator is placed inside of a planar wiggler. Two diagnostic screens S_2, S_3 were placed before and after the wiggler to allow beam crossection measurement. Section 5 consists of four quadropoles Q5 to Q8, which focus the e-beam into the sixth section (an electrostatic decelerating tube required for e-beam energy recovery). The beam is collected in the seventh section which is a depressed collector allowing e-beam energy recovery. The parameters of the TAU Tandem FEL are summarized in **table 2.1**:

Table 2.1 Parameters of the TAU EA FEL

ACCELERATOR:	
Electron beam energy	E_k=1.5MeV
Beam current	I_0=2A
UNDULATOR:	
Type:	Magneto-static planar wiggler
Magnetic induction:	$B_w=2KGauss$
Period length:	$\lambda_w=4.44cm$
Number of periods:	$N_w=26$
RESONATOR:	
Waveguide: Curved-parallel plates	
Transverse mode in resonator:	TE_{01}
Round-trip length:	L_c=2.62m
Out-coupling coefficient:	T=7%
Total round-trip reflectivity:	R=65%

2.2 Electron injector section

Good electron beam transport along the beam line of FEL oscillator is essential in order to enable efficient high power operation of the FEL, and also in order to obtain energy retrieval of the electron beam energy after interaction.

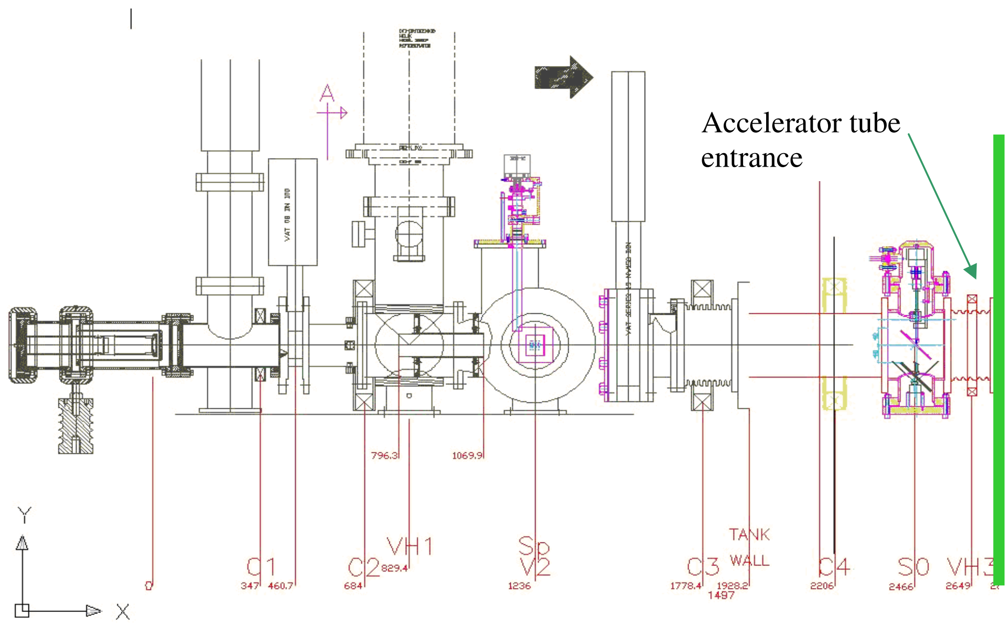

Fig.2.2 Layout of the electron optics elements in the injector section

The TAU EA-FEL injector section (Fig. 2.2) is 2m long; it is used to inject a *47kV*, *2A* electron beam into the accelerator tube (Fig 2.1) in which external magnetic fields were canceled. The e-beam is accelerated within the accelerator tube to 1.4*MeV*. The injector section includes two degaussing (Helmholtz) coils, focusing coils, steering coils, beam diagnostic screens and CCD cameras.

2.2.1 Schematic of beam line components and diagnostic means

The injector section layout is shown in Fig. 2.2. The geometry and performance of the beam line components is presented in table 2.2. Four focusing coils C1 to C4 are placed along the beam line to control the e-beam crossection; three steering coils (VH1-VH3) are placed along the beam line to correct deviations of the electron beam trajectory resulting from stray magnetic fields. Also two pairs of a Helmholz coils are placed along all injector section in order to repair an earth magnetic field influence on the electron beam transport. A steering coil set is composed of four circular coils located around the beam line (Fig 2.3).

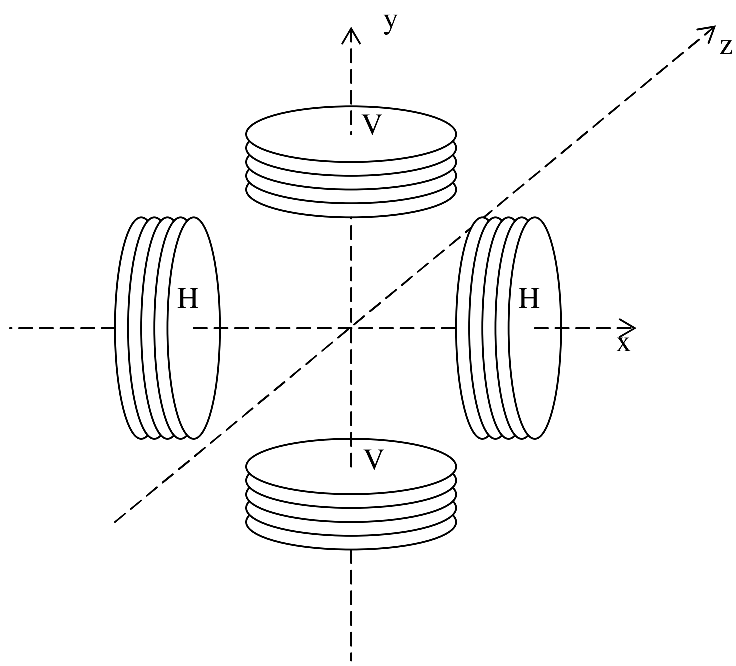

Fig 2.3 Schematic illustration of the injector vertical (V) and horizontal (H) steering coil pairs

Table 2.2 Details of the electron-optics elements placed in the FEL injector section (Fig 2.2) which was used for simulations.

Z (mm) from Cathode	Component
0	Cathode
241	Focusing coil C_1
475	Focusing coil C_2
553	Left end of Differential Tube
576	Steering coil VH_1
743	Right end of Differential Tube
859	Steering coil V_2
803	Screen S_P "Pepper Pot"
957	Steering Coil H_2
1235	Focusing coil C_3
1532	Focusing coil C_4
1713	Screen S_0
1840	Steering coil VH_3
1954	Left end of Accelerator Tube

Helmholz coil	Z (center) [mm]	Width [mm]	Length [mm]	Height [mm]
Hh	442	630	1730	310
Vh	442	310	1730	630

In order to monitor the electron beam in the injector section two diagnostic screens: S0 – ceramic screen and SP – titanium screen with aluminum oxide cover, were installed (Fig 2.4 a, b, c, d). The geometry of the beam was monitored using the fluorescence of the beam spot on the screens.

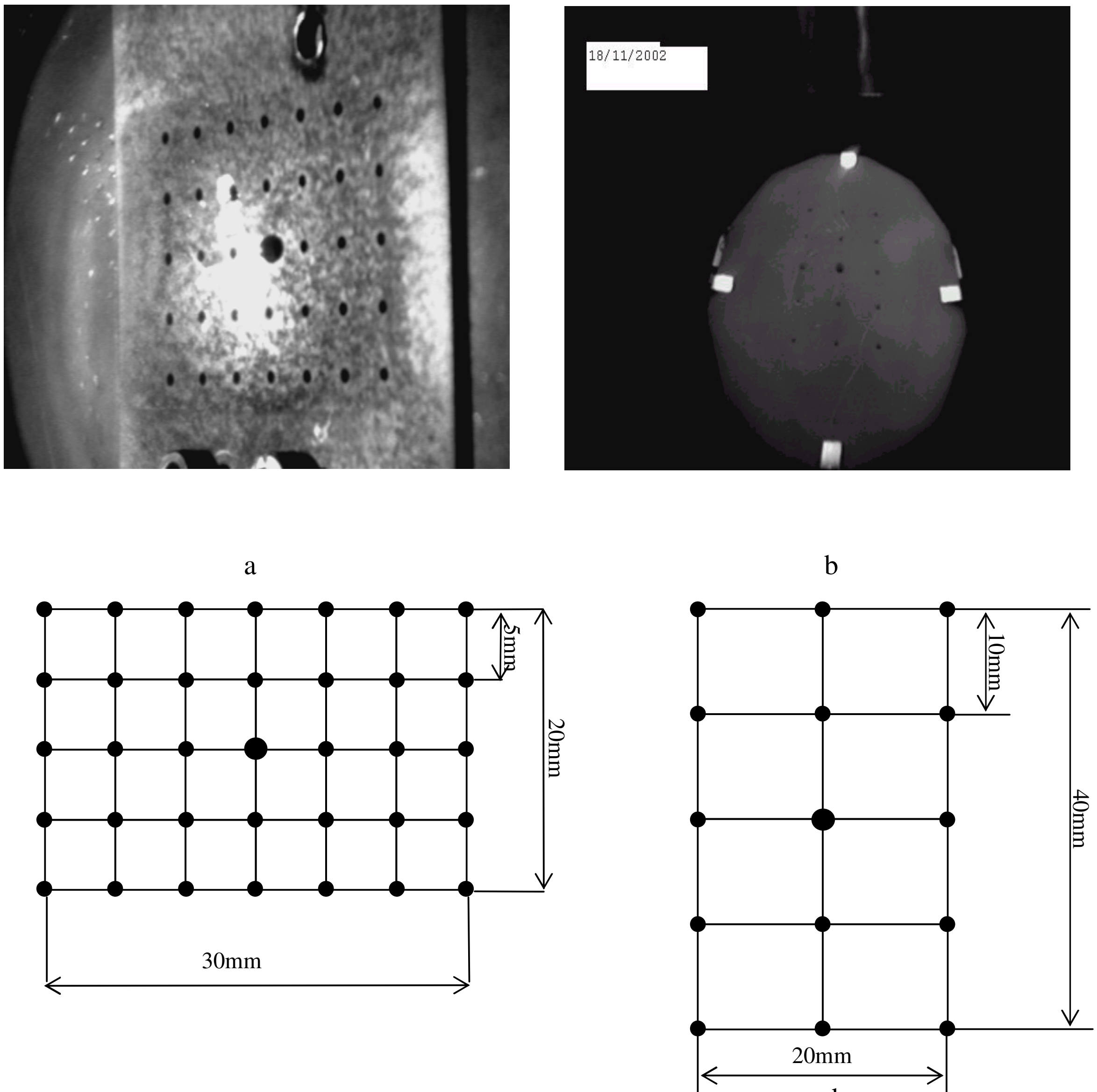

Fig 2.4 Photograph and schematic representation of the S0 (a,c) and SP (b,d) diagnostic screens

2.2.2 Electron-optics elements and electron beam transport simulations using E-GUN (Herrmannsfeldt) code

The design features of the triode electron Pierce gun which uses a thermionic cathode, (see table 2.3): It provides long cathode life in a moderate vacuum environment (10^{-6} mmHg), a top-hat current profile, and low emittance electron beam.

The cathode is a barium tungsten cathode (M-type). It operates at a temperature of 1100°C; which gun operates inspace-charge limited regime: At these conditions the beam current is 2A, the grid voltage is 20kV and the anode voltage is 47kV.

Table 2.3 Electron gun parameters

DC beam current	2 A
Anode Voltage	47 kV
Grid Voltage	6-20kV
Electron Gun Perviance	$0.195 \cdot 10^{-6} AV^{-3/2}$
Cathode radius	7.5 mm
Distance from Cathode to Grid	17 mm

For the design of the present gun the E-GUN simulation code was used (Herrmannsfeldt WB. 1988). The geometry of the electron gun and of the simulation results of current flow are shown at Fig. 2.5

The space-charge dominated transport in the gun follows quite well the Childs-Langmuir law. A thorough study of the gun transport characteristics was carried out experimentally and numerically in order to characterize ht gun. This is described in sections 3.1.2 and 4.1.

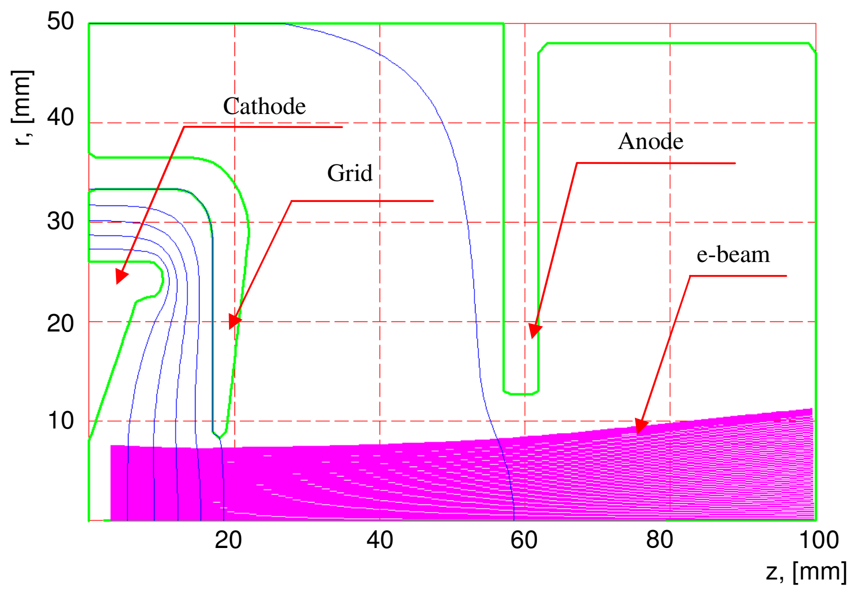

Fig.2.5 E-GUN simulation for FEL's electron gun geometry

Focusing lenses are required between the gun and accelerator input in order to overcome the space-charge field expansion right after the gun cathode, transport the beam all the way to the accelerator entrance and inject it into the accelerator with matched beam parameters. In particularly the beam must arrive to the accelerator entrance diverging and wide (see Fig. 2.6) in order to counteract the focusing effect at the accelerator entrance (see also Chapter 3). The magnetic field in the air core solenoids were simulated using one cylindrical current loop corresponding to the average coil radius Figs. (2.5, 2.6) display the beam transport in the gun and up to the accelerator entrance.

The electron beam expands due to space charge forces after exiting from the gun, and the e-beam is refocused by the large radius solenoids C1 to C4. The large radius electron beam ensures that the electron beam dynamics in the accelerator section is driven by the accelerator's focusing effect at its entrance, balanced by space-charge beam expansion effect. The e-beam injection into the accelerator region (see also Fig. 2.9) critically affects the electron beam characteristics along the beam line. Our choice was based on emittance minimization criteria; the emittance was measured in the terminal using the pepper-pot technique (see Chapter 4).

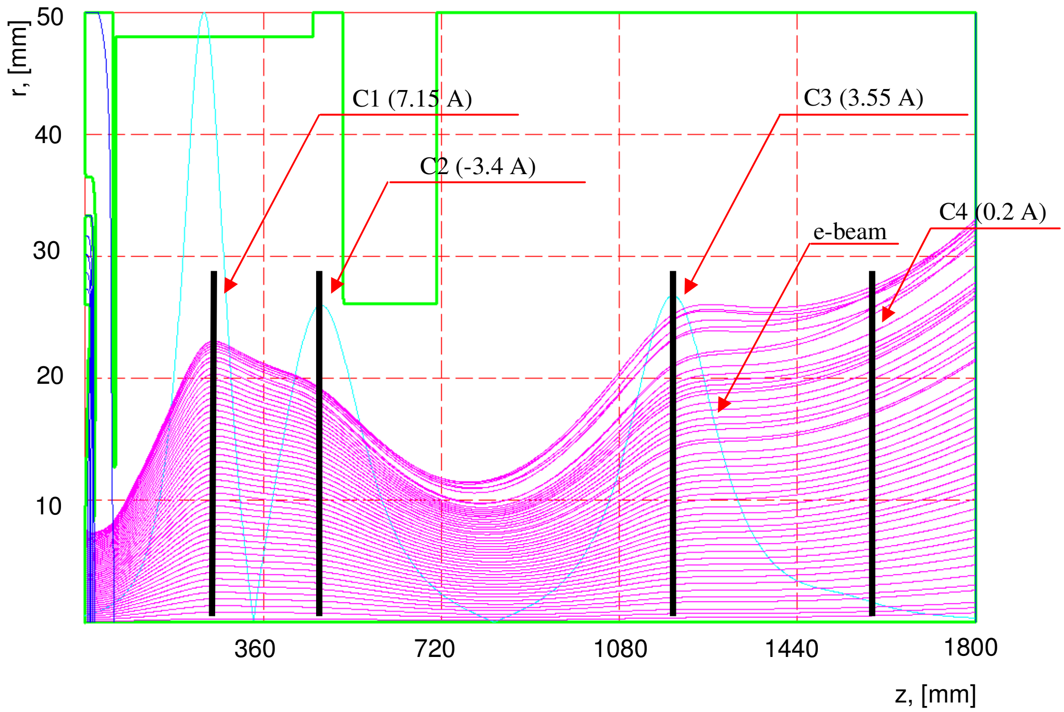

Fig 2.6 E-GUN simulation of the electron beam transport, from the cathode to the accelerator entrance (injector section). The accelerator field is off and the beam entrance diverging.

The E-GUN simulations can be carried out only for axi-symmetric geometry. They do not include stray magnetic fields effect, and do not simulate the effects of steering electron-optics elements.

2.3 Accelerator section

The accelerator section of the TAU EA-FEL includes electrostatic acceleration and deceleration tubes, quadrupoles, wiggler, Pearson coils (for current measurements), and steering coils (see Fig.2.7). Three diagnostic screens S_1, S_2, S_3 are placed at the acceleration section exit, at the wiggler entrance plane and at the wiggler exit plane respectively.

2.3.1 Schematic of beam line components and diagnostic means

The geometry and performance of the beam line components in the accelerating section are presented in table 2.4.

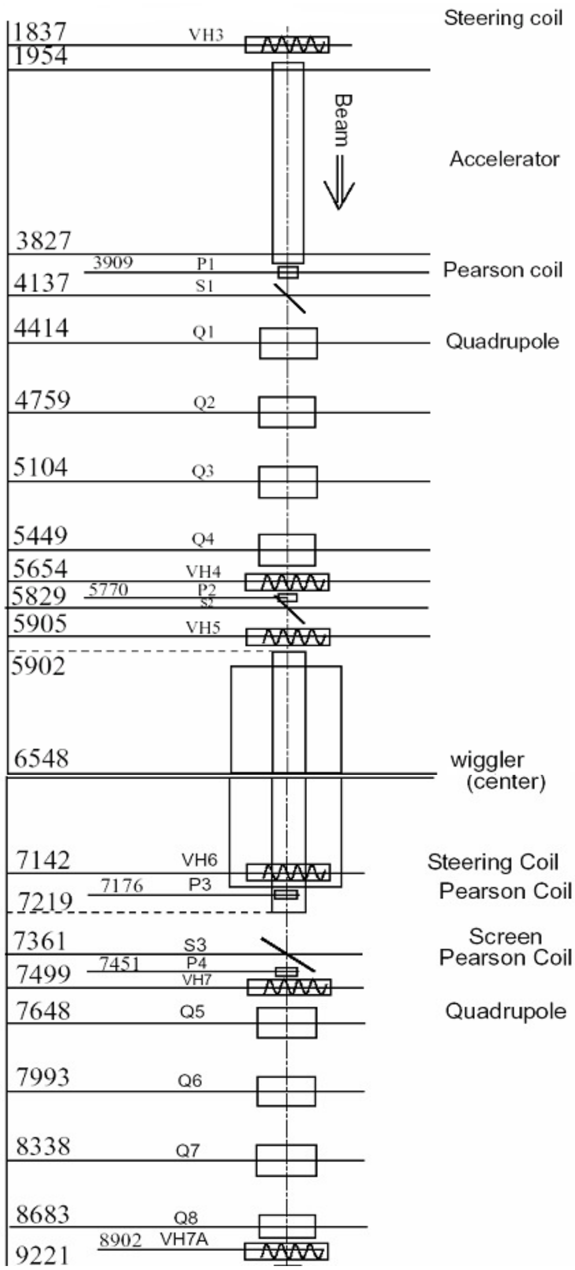

Fig 2.7 Layout of the electron-optics elements placed in accelerating section

Z (mm) from Cathode	Component
1837	Steering coil VH_3
1954	Left end of Accelerator Tube
3827	Right end of Accelerator Tube
3909	Pierson coil P_1
4137	Screen S_1
4414	Quadrupole Q_1
4759	Quadrupole Q_2
5104	Quadrupole Q_3
5449	Quadrupole Q_4
5654	Steering coil VH_4
5770	Pierson coil P_2
5829	Screen S_2
5905	Steering coil VH_5
7051	Steering coil VH_{5a}
7142	Steering coil VH_6
7176	Pierson coil P_3
7361	Screen S_3
7451	Pierson coil P_4
7499	Steering coil VH7
7648	Quadrupole Q_5
7993	Quadrupole Q_6
8338	Quadrupole Q_7
8683	Quadrupole Q_8
8902	Steering coil VH_{7a}

Table 2.4 Details of the electron-optics elements placed in the accelerating section (Fig 2.7) which was used for simulations.

2.3.2 The electrostatic accelerator

The electrostatic acceleration and deceleration tubes consist of 75 electrodes each, glued to each other with glass insulator ring spacers (Fig. 2.8). The distance between electrodes is 24mm and the potential difference between consecutive rings is 40 kV. The inner diameter of the electrode apertures is tapered (reduced) from the accelerator entrance plane to the end of accelerator tube (from 63 to 44mm) so as to enable large beam input diameter beam transport.

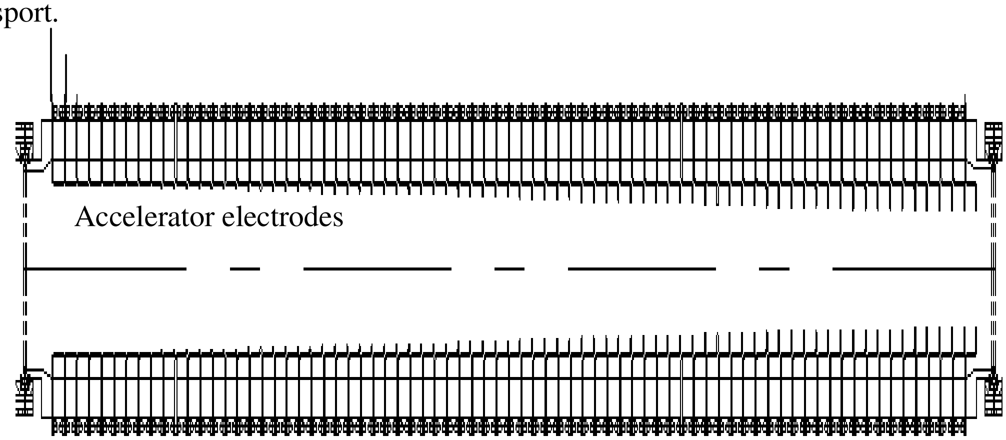

Fig 2.8 Layout of the FEL electrostatic accelerator

Simulation of the electron beam transport, trough the accelerator section was performed using E-GUN code (shown in Fig. 2.9)

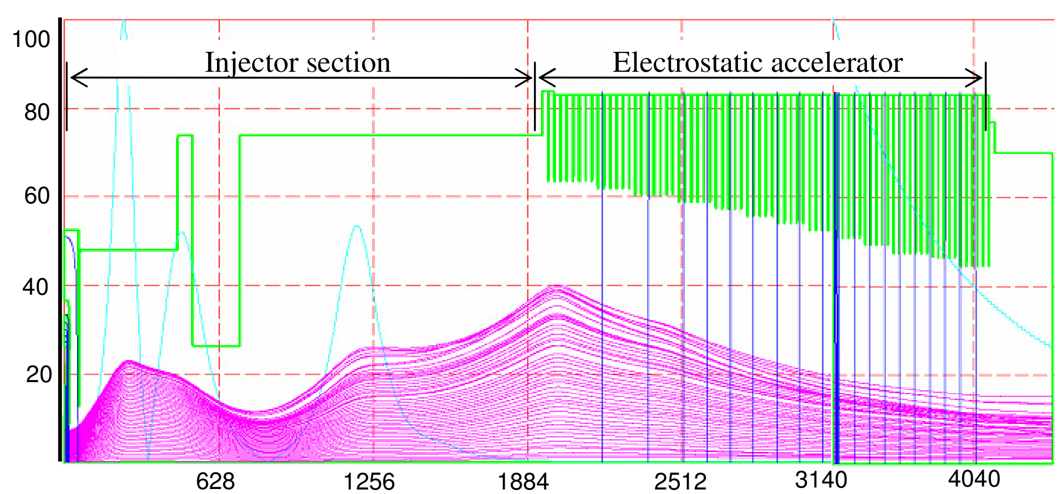

Fig 2.9 E-GUN Simulation of the electron beam transport, from the cathode to the accelerator exit

2.3.3 Wiggler schematic and description

The planar magnetic wiggler consists of 26 magnet periods (permanent SmCo magnets); where each magnet period contains 4 rectangular magnet pairs arranged in a Hallbach configuration (Hallbach K 1980). In addition there are additional half strength permanent matching magnet pairs at each end of the wiggler which control the of axis drift and angle drift of the electron beam, and two long magnets for horizontal focusing (see Fig 2.10, 2.11)

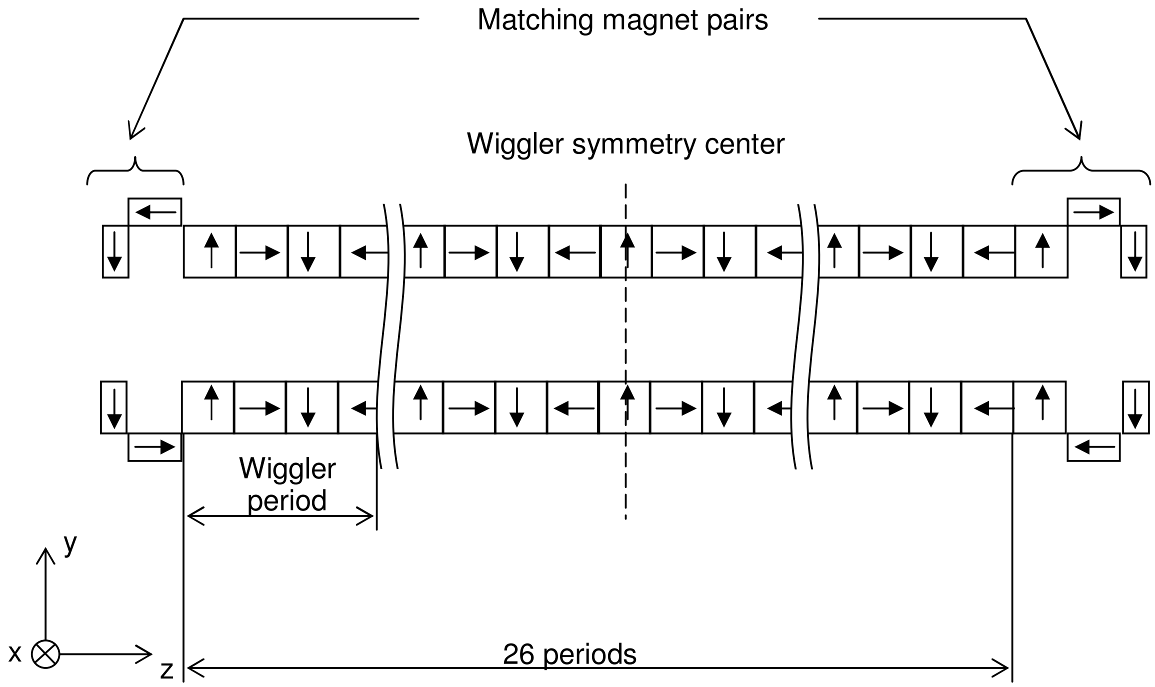

Fig 2.10 Scheme of the magnets orientation in the TAU FEL wiggler

The trajectory of a single electron inside the wiggler is determined from the relativistic Lorenz force equation:

$$\gamma m \frac{d\mathbf{v}}{dt} = -e\mathbf{E} \times \mathbf{v} \times \mathbf{B} \qquad (2.1)$$

The magnetic field of an ideal planar wiggler is given near the axis by (Gover A., et al. 1984):

$$\mathbf{B_w} = \hat{\mathbf{y}} B_w \cosh k_w y \cos k_w z - \hat{\mathbf{z}} B_W \mathrm{sinsh} k_w y \sin k_w z \tag{2.2}$$

where $\mathbf{B_w}$ is the peak amplitude of the magnetic field, $k_w = \dfrac{2\pi}{\lambda_w}$ is the wave number of the wiggler. If we assume that $v_{0z} >> v_y, B_y >> B_z$ and replace the time derivative d/dt with $v_{z0} d/dz$, we obtain using 2.2 the following equations:

$$\frac{dv_x}{dz} = v_w k_w \cosh k_w y \cos k_w z \tag{2.3}$$

$$\frac{dv_y}{dz} = -\frac{v_x}{v_{0z}} v_w k_w \sinh k_{wy} \sin k_w z \tag{2.4}$$

where $v_w = \dfrac{eB_w}{\gamma m k_w} = \dfrac{a_w c}{\gamma}$ is the transverse velocity amplitude in the *x*-direction and $a_w = \dfrac{eB_w}{mck_w}$ is the wiggler parameter. Averaging 2.3 and 2.4 over period a λ_w we find the average displacement $\bar{x}$ in the *x*- direction and $\bar{y}$ in the y direction as given by (Cohen M. 1995)

$$\bar{x} = \frac{v_{x0}}{v_{0z}} z + x_0 \tag{2.5}$$

the wiggling motion in the *y* direction is given by:

$$\bar{y} = y_0 \cos k_\beta z + \frac{v_{y0}}{v_{0z} k_\beta} \sin k_\beta z \tag{2.6}$$

where

$$k_\beta = \frac{a_w k_w}{\sqrt{2}\gamma\beta_{0z}} \tag{2.7}$$

is the betatron wavenumber. The wiggling motion of the electrons is superimposed on their average motion in the x dimension. The net displacement is

$$x(z) = \bar{x}(z) - x_w \cos k_w z \tag{2.8}$$

where

$$x_w = \frac{v_w}{v_{0z} k_w} = \frac{a_w}{\beta_{0z} \gamma k_w} \tag{2.9}$$

Inspection of the average displacement in the *x* and *y* directions show that vertical focusing is provided by the wiggler itself, while there is no focusing in the horizontal direction. In the *x*-direction the electron trajectory diverges from the wiggler axis if it has an initial transverse velocity component v_{x0}. In order to provide focusing in the *x* direction; a field $\mathbf{B}_y$ is used having a dependence on x given by:

$$\mathbf{B}_y(x) = -\alpha_R \hat{\mathbf{y}} \tag{2.10}$$

Because one must satisfy $\nabla \times B = 0$ there is also an opposite gradient B_z in the *y* direction:

$$\mathbf{B}_x(y) = \alpha_R y \hat{\mathbf{x}} \tag{2.11}$$

where α_R is the magnetic field gradient. A magnetic field gradient in the *x* direction is produced if two longitudinal magnets “A” and “B” in Fig. 2.11 are placed as shown in Fig.2.11. Such a field gradient produces a restoring force which focuses electrons which disperse in x direction close to z axis. The adjunct field gradient Eq. 2.11 produces a defocusing force in the *y* direction and reduces the focusing effect of the wiggler in this direction.

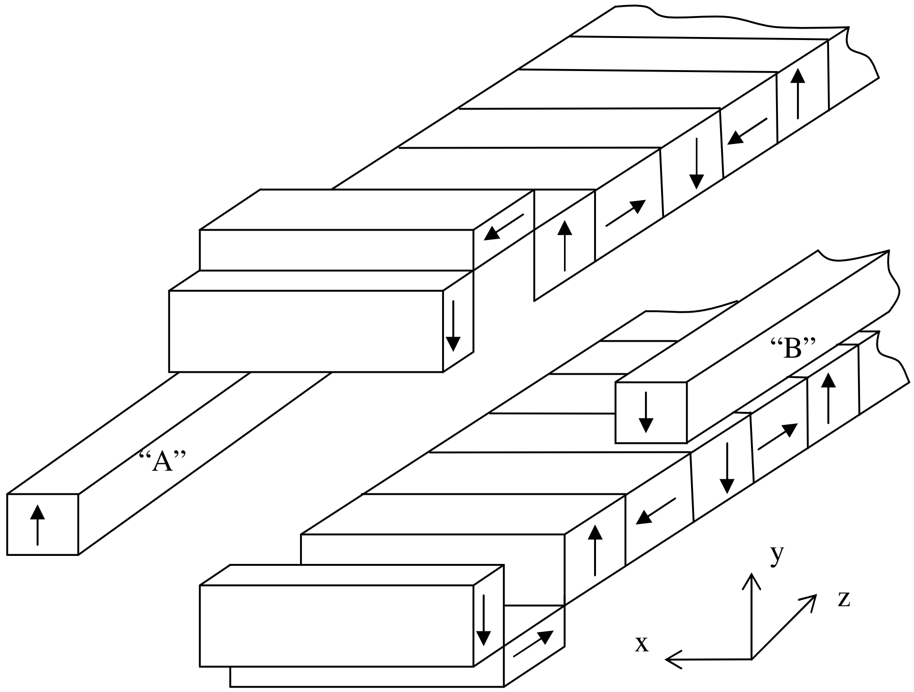

Fig 2.11 Scheme of a planar wiggler with two longitudinal magnets (A, B) providing a focusing in the horizontal dimension and matching magnets to control the of axis drift and angle drift of the electron beam

The average motion of electrons in the x direction, in the presence of the combined fields Eq.2.2, 2.10, is found to be (Cohen M. 1995):

$$\bar{x}(z) = \frac{v_{x0}}{v_{0z} k_{\beta x}} \sin k_{\beta x} z + \left(x_0 + \frac{\sqrt{2} k_\beta}{k_w^2 - k_{\beta x}^2} \right) \cos k_{\beta x} z \qquad (2.12)$$

where:

$$k_{\beta x} = \sqrt{\frac{e\alpha_R}{\gamma m v_{0z}}} \qquad (2.13)$$

is the horizontal betatron wavenumber. The full trajectory of the electron in the x-z dimension consists of a superposition of the wiggling motion and the average motion (Eq. 2.8); however this wiggling amplitude is slightly modified (Kugel A., 1996)

$$x_w = \frac{x_w^0}{1 - k_\beta^2 / k_w^2} \tag{2.14}$$

where x_w^0 is the wiggling amplitude for $\alpha_R = 0$

is replaced by (Kugel A., 1996):

$$k_{\beta y}^2 = \frac{k_\beta^2}{1 - \left(\dfrac{k_{\beta x}}{k_w}\right)^2} - k_{\beta x}^2 \tag{2.15}$$

If the ratio between $k_{\beta x}$ and $k_{\beta y}$ is equal to unity one obtains a circular cross-section of the e-beam; otherwise, an elliptical cross-section beam is obtained.

2.4 The deceleration section and the collector

Beyond the interaction section, particularly after beam deceleration the beam transport is deteriorated. This is of significant rematch during lasing, because of the energy spread of the spent beam which amounts to 110-120 keV. A set of quadrupoles (Q5 to Q8) is employed to transport the beam into the deceleration tube so as to generate a round beam at the entrance with a relatively large beam radius (~30mm) and with identical converging slopes in both the horizontal and the vertical planes. The quadrupole field strengths are set to focus the beam into the beam pipe located at the end of the decelerator column where the potential is chosen to be 65kV. Four solenoids (C5 to C8) are required to ensure the beam transport in the drift section between the decelerator exit and the depressed collector entrance. In this part of the beam line, the beam optics design requires an energy acceptance of 55-180 keV.

A schematic of the beam transport system following the undulator section and the two-stage collector is shown in Figure 2.12, the position and performance of the beam line components is presented in table 2.5. The present configuration of the collector assembly consists of 2 inch diameter vacuum pipes assembled in sequence in the low voltage end of the decelerating tube serving as the current colleting electrodes. The present two-stage collector allows achievement of 99% current recovery and 28% energy recovery efficiency (Tecimer 2004).

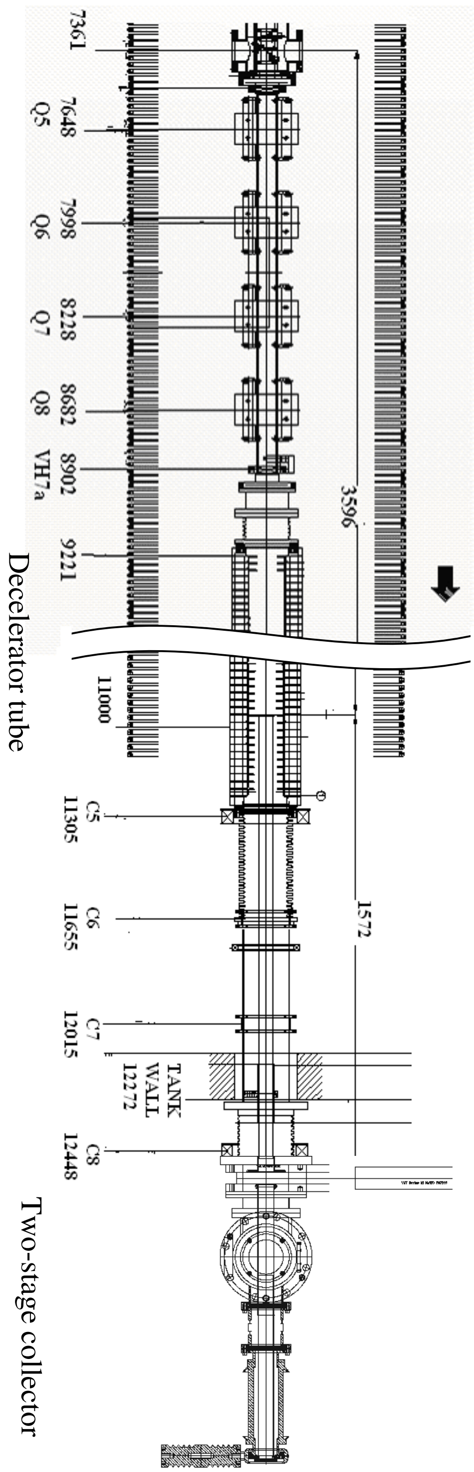

Fig.2.12 Layout of the beamline section from the undulator exit to the two-stage collector entrance

7648	Quadrupole Q_5
7998	Quadrupole Q_6
8228	Quadrupole Q_7
8682	Quadrupole Q_8
8902	Steering coil VH_{7a}
9221	Left end of Decelerator Tube
11233	Right end of Decelerator Tube
11305	Focusing coil C_5
11687	Steering coil VH_8
11723	Focusing coil C_6
12213	Focusing coil C_7
12448	Focusing coil C_8

Table 2.5 Details of the the beamline section from the undulator exit to the two-stage collector entrance (Fig 6.4) which was used for simulations.

In order to improve energy recovery efficiency a new multistage collector was designed and constructed, but not yet assembled (Tecimer 2004). The present work was carried out with the accelerator operating with the two-stage collector. The characterization of this collector is described in section 4.4.

Chapter 3 Simulation and analysis of electron beam transport in the Israeli FEL

In this chapter we describe the electron beam transport in different parts of the FEL, and present the results of various simulation codes, which we used for the analysis of the electron beam transport. The electron beam transport in the injector section is analyzed using E-GUN and GPT simulation codes. A special code GUNDIST, was developed in order to take advantage of the E-GUN and GPT codes used complementary. The results of the simulation code predictions in the injector section compared well with experimental results. The electron transport in the high energy section was studied using ELOP, GPT and E-GUN simulation codes. Optimization of the electron beam transport including wiggler betatron oscillations and space-charge effects in the wiggler and the high voltage terminal are described. A model for the electrostatic accelerator analysis using the GPT code was developed and compared to the E-GUN model. Improvements of the initial electron sampling algorithm, for different simulation codes are proposed. The results of the electron beam transport analysis compared well to the experiments.

3.1. Electron beam transport in the e-gun and in the injector section (up to 50 keV)

The electron optics and electron beam transport design in the electrostatic accelerator FEL differ from other FELs because of the relatively low energy of the e-beam. This results in a non-negligible effect of space-charge on the electron beam transport, even at moderate beam currents (of 2 Amps).The injector section in which the electron beam is produced has to deliver it to the accelerator entrance under optimal acceptance conditions. In the injector section even weak magnetic fields (geomagnetic fields and stray magnetic fields of ion pump magnets) can apply substantial deflection forces on the e-beam. This causes deviations from the desired electron beam trajectory that can be corrected only in part by beam line steering coils. Consequently, the combined effect of such errors, electron-optical component aberration on the axis and space-charge effects are liable to cause deterioration of the e-beam quality and its emittance. The results of measurements and electron-optics improvements which were made will be described in this section. The experimental results will be compared to 3-D beam simulations including space-charge effects. The maim simulations were performed using the 3-D particle tracing code GPT. The results of these simulations were compared at different sections to the E-GUN code simulations and to the experimental results.

3.1.1 The GPT tracing code

The analysis of electron beam transport in the injector section is performed using a 3-D particle simulation code GPT, that allows (contrary to the 2D E-GUN simulation code) to take into account effects of steering electron-optic elements and of stray magnetic fields (Pulsar 2004). The equations of motion for a set of macro-particles are integrated in the time domain using the fifth order Runge-Kutta method with adaptive stepsize control (Press W.H. et. al 1992).

In GPT the beam space-charge fields are derived from the sum of forces experienced by each individual macro-particle due-to the Coulomb force of all others. The "*spacecharge2Dline*" option of GPT (Pulsar 2004) was used to simulate the electron dynamics in the EA-FEL beam line. This option corresponds to continuous coasting beam. This is a good approximation for an electrostatic accelerator in which the pulse duration is at least microseconds long. Every macro-particle is represented as a moving line-charge, directed in the particle's velocity. The space-charge fields are calculated assuming the electron beam to be composed of line-charges oriented in the direction of motion. The space charge fields at the position of a certain macro-particle are calculated as the sum of the fields produced by all line-charges corresponding to the other macro-particles and then substituted in the relativistic equation of motion.

There is also a 3-D space charge model (Pulsar 2004) is used in GPT, based on consideration of the coulomb field applied by the sample electrons on each other. The electric field produced by each macro-particle which applied on the other macro-particles is calculated in the electron rest frame, and transformed relativisticly back in to the laboratory frame. In the rest frame, each particle generates only electric fields: the transformation into the laboratory frame results in electric and magnetic fields (Jacson J. 1962). The total fields due to space-charge at the position of the generic particle are then calculated as the sum of the contributions of all the other particles. A disadvantage of this method is the price to be paid in terms of cpu-time because computation time particle-particle interaction is a N^2 process, where N is the number of particles.

The position $\boldsymbol{x}$ and the momentum $\mathbf{p} = \gamma m v$ of a set of macro-particles are used as the coordinates. The equations of motion for the *j-th* particle are given by:

$$\begin{aligned} \frac{d\mathbf{p}_j}{dt} &= \mathbf{F}_j \\ \frac{d\mathbf{x}_j}{dt} &= \mathbf{v}_j = \frac{\mathbf{p}_j c}{\sqrt{\mathbf{p}_j^2 + \left(mc^2\right)}} \\ \mathbf{F}_j &= e\left(\mathbf{E}_j + \mathbf{v}_j \times \mathbf{B}_j\right) \end{aligned} \tag{3.1}$$

where $\mathbf{F}_j$ is the total force (including the beam self-fields) at the location of the *j-th* particle, $\mathbf{E}_j$ and $\mathbf{B}_j$ are the total electric and magnetic field produced at the location of the *j-th* particle, by the electromagnetic fields, by the beam line components and by other charged particles. The GPT simulation code does not take into account the image charges fields due to conductor surfaces present at proximity to the e-beam.

3.1.2 Comparison of E-GUN and GPT simulations of electron trajectories in the injector section

It is not possible to simulate the electron trajectories in the electron gun using the GPT tracking code, since the gun contains conductive electrodes in close proximity to the e-beam, and GPT code does not take into account the image charges. On the other hand E-GUN code operates efficiently in this section and can be used there because the gun has cylindrical symmetry.

The solution we adopted, was to use E-GUN in the electron gun, and use its output (after the anode) as input for GPT simulation code in following transport sections.

In order to match the output of E-GUN to the input of GPT, a special code "GUNDIST' was written by us on a MATLAB base (see Appendix A). The purpose of the GUNDIST code is to make the output of E-GUN simulation suitable as an input for the GPT code calculations.

In E-GUN the electron beam emitted from the cathode is simulated by sample electrons, each representing the electrons emitted from a concentric ring on the cathode. The rings (and the sample particles) are equi-spaced at the cathode. There is no angular or radial electron momentum spread at the cathode except for possible uniform azimuthal angles related to each electron ring, resulting from external or self (axisymmetric) magnetic fields.

In the GUNDIST transformation program we re-sample the electron beam at a plane $z=const$, a few mm after the gun anode. Each E-GUN sample electron in this plane is replaced by multiple GPT sample electrons distributed randomly in a concentric circle with the same radius. The number of electrons in each ring is selected to be proportional to the radius of the E-GUN sample electron at this lane. (rounded up to an integer) the more correct algorithm would be proportionally to the radius of the sample electron at the cathode, but the difference is minute in laminar beam flow.

The angular distribution output of E-GUN contains the radial θ_r angle of each sample electron (representing a ring) with radius r and electron energy E at chosen $z=const$. The GUNDIST corresponds to each sample electron also a random azimuthal angle θ_φ and then translates the output E-GUN parameter to the velocity distribution input parameters and of GPT (β_x β_y β_z) assuming the same values to all the GPT sample electrons representing single E-GUN sample electron.

In order to test the efficiency of the codes connection procedure the electron beam trajectory simulations were performed by two ways: by the E-GUN code from the cathode into the injector section and by the GPT code from the anode into the injector section. The results showing the electron trajectories after exiting the electron gun Fig 3.1a, b show good agreement between E-GUN and GPT simulations.

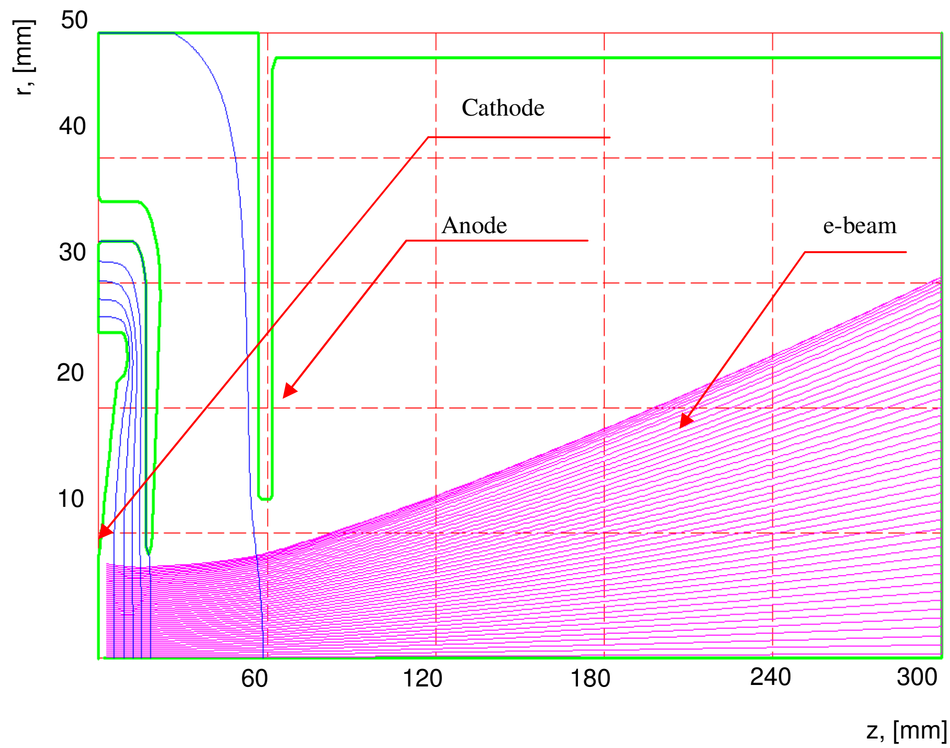

(a) E-GUN simulation of the electron beam propagation, from the cathode to a chosen plane at coordinate $z = 300$mm.

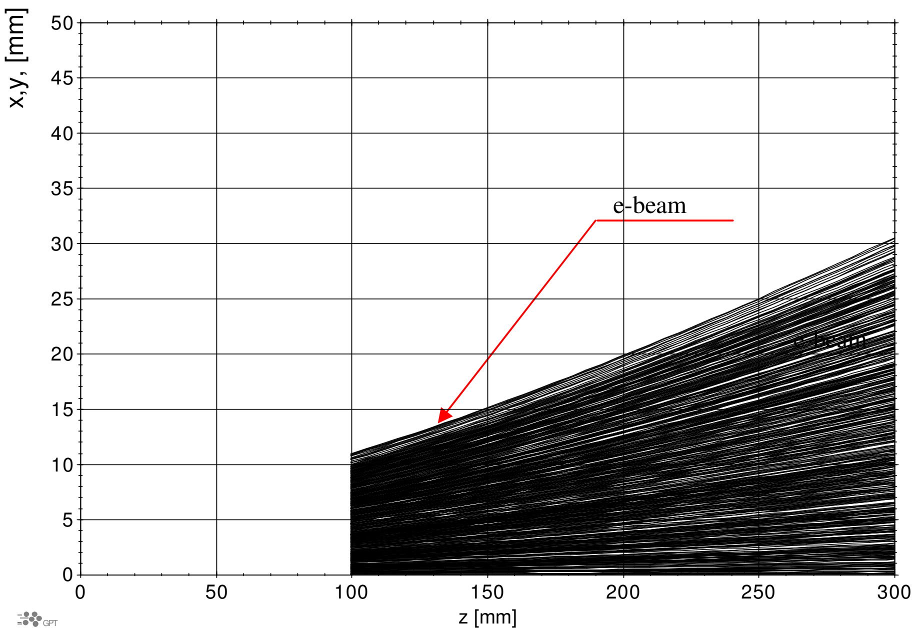

(b) GPT simulation of the electron beam propagation, from the electron gun exit z = 100mm to the chosen plane at coordinate z = 300mm

Fig 3.1 (a),(b) Comparison between the E-GUN and GPT simulation results

3.1.3 GPT simulations of electron transport in the injector region and comparison to experimental results

The aim of the simulation in the injector section (which starts from the cathode and ends at the accelerator tube entrance), is to attain optimal beam injection parameters namely dimensions and divergence angles at the accelerator tube entrance (Volshonok M. and Adam O. 2003). Other motivations are to avoid any electron interception in apertures, and attaining optimal electron beam parameters (3.4-3.5). The injector section includes four focusing coils C_1 to C_4, three steering coils VH_1 to VH_3, vertical and horizontal Helmholtz coils. Two diagnostic screens S_0 and S_p are placed in this section (Fig. 2.2 and Table 2.2). In order to achieve the optimal electron beam transport in the injector section we adjusted the currents of C_1 - C_4, and checked that the spot sizes on screens S_0, S_p were in good fit with the GPT simulations. Experimentally we also needed to adjust the steering and Helmholtz coils in order offsets the effects of the earth magnetic field and stray magnetic fields. Fig. 3.2 shows the results of GPT simulations along with the positions of the focusing coils and the steering coils (it can be verified that the GPT simulations match well also the E-GUN simulations). This should be compared to the E-GUN simulation results, shown on Fig. 2.6.

The simulated electron beam dynamics in the injector section using C1-C4 focusing coils have been found to be in good agreement with the experimental results. The results are summarized at Table 3.1 a, b

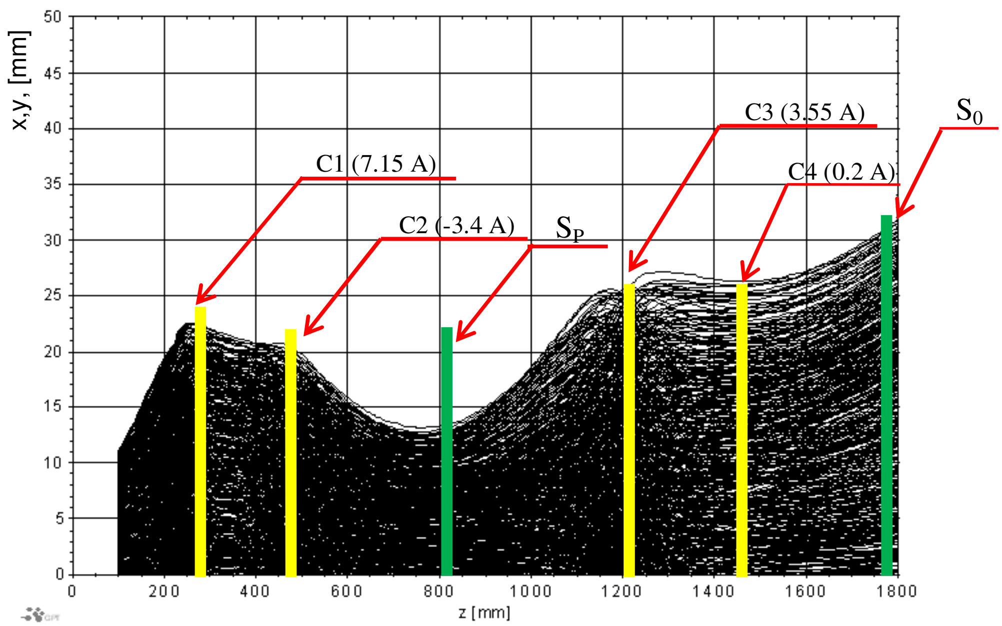

Fig. 3.2 GPT simulation of the optimal injection parameters of electron beam transport, from the gun exit z = 100 to the accelerator entrance (the accelerator field is turned off)

Table 3.1 Comparison between GPT simulation and experiment (Positive current corresponds to axial magnetic field in the + z direction)

Table 3.1a The measurements made on SP screen, (average error ~ 8%)

Current at C1, [Amp]	Current at C2, [Amp]	Beam diameter, Experiment X [mm]	Beam diameter, experiment Y [mm]	Beam diameter, simulation D [mm]
7.5	-3.2	33	34	35.5
7.8	-3.2	29	30	32
8	-3.2	28	28	29.5
8	-3	29	32	33
8	-3.5	25	25	27
8	-3.8	22	22	24
8	-4	20	19	22
8	-4.2	19	18	20

Table 3.1 b The measurements made on S0 screen, (X - average error~9%, Y - average ~12%)

Current at C1, [Amp]	Current at C2, [Amp]	Current at C3, [Amp]	Current at C4, [Amp]	Beam radius, Experiment X [mm]	Beam radius, Experiment Y [mm]	Beam radius Simulation, R [mm]
8	-4	3.3	2	35-33	32-33	34.5
8	-4	3.5	2	31-30	28-29	31
8	-4	3.6	2	29-27.5	27-28	30
8	-4	3.8	2	26-24.5	24-25	27
8	-4	3.8	1.5	26-25	23-24	28.5
8	-4	3.8	2.5	24-23.5	21-22	25
8	-4	3.8	3	42-41	36-37	44
8	-4	3.8	3.5	37.5-37	31-32	39
8	-4	3.8	4	27.5-27	23-24	34
8	-4	3.8	4.5	18.5-18	16-17	28

3.2 Electron beam transport in the high voltage terminal

3.2.1 Analysis and simulations of electron beam transport through the wiggler section using the ELOP simulation code

In order to simulate the electron trajectories in the HV-terminal of the FEL, a special simulation code "ELOP" was developed at TAU (Merhasin I. 1998). By use of this code one can solve the Lorenz force equation in three dimensions for each particle moving along the beamline.

The relevant equations are:

$$
\begin{aligned}
\frac{dv_{xi}}{dz} &= \frac{1}{\gamma_i}\left\{-\frac{e}{m}\frac{1}{v_{zi}}\left[E_x + \left(v_{yi}B_z - v_{zi}B_y\right)\right] - v_{xi}\frac{d\gamma_i}{dz}\right\} \\
\frac{dv_{yi}}{dz} &= \frac{1}{\gamma_i}\left\{-\frac{e}{m}\frac{1}{v_{zi}}\left[E_y + \left(v_{xi}B_z - v_{zi}B_x\right)\right] - v_{yi}\frac{d\gamma_i}{dz}\right\} \\
\frac{dv_{xi}}{dz} &= \frac{1}{\gamma_i}\left\{-\frac{e}{m}\frac{1}{v_{zi}}\left[E_x + \left(v_{xi}B_z - v_{yi}B_x\right)\right] - v_{zi}\frac{d\gamma_i}{dz}\right\} \\
\frac{d\gamma_i}{dz} &= -\frac{e}{mc^2}\frac{1}{v_{zi}}\left(v_{xi}E_x + v_{yi}Ey + v_{zi}Ez\right)
\end{aligned}
\tag{3.2}
$$

The magnetic field of each permanent rectangular magnet contained in the wiggler Fig 2.10 is calculated by using the surface current model of magnets (Elias L. 1983), wherein each magnet is replaced by a rectangular loop of sheet current.

Using the "ELOP" code we calculate the magnetic field along the beamline (z-direction). From this data, the three dimensional location of each particle is calculated by integrating (3.2). The code does not take into account space charge effects on the e-beam. In section 3.2.4 we use the electron beam transport GPT simulation in order to take into account the space-charge effects.

3.2.2 Optimization of electron beam transport through the wiggler section using the ELOP simulation code

We first determine the e-beam emittance – an important parameter for e-beam transport optimization. The emittance is a variable which characterizes the effective phase-space volume of the beam distribution (Humphries S. 1990). It is a measure of the beam divergence characteristic. At the beam waist it is equal to the product of the electron beam size and its angular divergence. The emittance is related to the volume occupied by the beam at given transport coordinate z in phase-space (x, x', y, y'), where (x, y) are the transverse electron coordinates and (x', y') are the transverse angles of the electron orbits. Often the effective beam phase-space volume is defined as the four dimensional volume of the minimum-volume hyper-ellipse that surrounds all the orbit vector points. When the motion in x and y directions are separable, the emittance may be defined independently in the (x, x') and in the (y, y') spaces:

$$\begin{aligned} \varepsilon_{xx'} &= \frac{1}{\pi}\int dx dx' \\ \varepsilon_{yy} &= \frac{1}{\pi}\int dy dy' \end{aligned} \tag{3.3}$$

The unit of emittance "ε" is [m rad] (sometimes [π m rad] to indicate an ellipse area).

In a thermionic cathode electron gun the temperature of the cathode ultimately limits the distribution of the electron transverse velocities and therefore the beam emittance. Space charge forces and acceleration process tend to increase it. In the paraxial beam optics approximation, in the absence of acceleration the emittance is a conserved quantity when a beam is subjected to linear electron-optical processes. Nonlinear processes may distort the elliptic boundary of the phase-space distribution. Even if interactions conserve the effective phase-space area (by Lowville's theorem), the phase-space shape distortion increases the effective emittance. The normalized emittance $\varepsilon_n = \gamma\beta\varepsilon$ takes into account the fact that the (x, x', y, y') phase-space volume deceases with beam acceleration (because the transverse momentum remains constant while the longitudinal momentum increases) while the phase-space volume (x, β_x, y β_y) remains constant. Often the notation "emittance" refers to normalized emittance.

The contribution of emittance to beam expansion becomes dominant at high energy, where the space-charge force is negligible. The emittance sets a lower limit to the minimal dimensions of the beam permitted by transport apertures.

Optimal beam transport through the wiggler requires specific initial beam injection conditions (namely specific phase-space acceptance ellipsoid parameters) at the wiggler entrance (Gover A. 1984). The beam envelope must be at its waist at the entrance (which means that the beam ellipsoid is erect in the 4-D phase-space) and the beam cross section dimensions are:

$$r_{bx0} = \sqrt{\frac{\varepsilon_x}{\pi k_{\beta x}}} \tag{3.4}$$

$$r_{by0} = \sqrt{\frac{\varepsilon_y}{\pi k_{\beta y}}} \tag{3.5}$$

The wave numbers of the planar wiggler betatron oscillations $k_{\beta x}$ and $k_{\beta y}$ can be calculated from the analytical expressions, Eq 2.13, Eq 2.15.

The analytical theory predicting of the optimal beam injection parameters into the wiggler was verified with ELOP code (see Fig. 3.3) which displays optimal (scallop-free) beam propagation of a finite emittance beam dimensions chosen according to (Eq. 3.4., 3.5). In this simulation the beam was started at symmetry point *z=0* and propagated to the +*z* and –*z* dimension. At optimal transport conditions the phase-space ellipsoid at this symmetry point must be erect. The initial conditions distribution inserted at this point was chosen accordingly.

The initial conditions of the electron beam (its crossection dimensions) at the wiggler entrance are controlled by the magnetic fields of quadrupoles Q1-Q4 i.e. by the current in each quadruple.

The magnetic field distribution of the quadrupoles is modeled by:

$$\begin{aligned} \mathbf{B}_x(x,y) &= \frac{\mathbf{B}_0}{L_{width}}\, y\, \mathrm{rect}[(z-z_i)/L] \\ \mathbf{B}_y(x,y) &= \frac{\mathbf{B}_0}{L_{width}}\, x\, \mathrm{rect}[(z-z_i)/L] \end{aligned} \tag{3.6}$$

where $\mathbf{B}_0$ is the maximal field of the quadrupole at edges of the linear region of the quadrupole $(x = \pm L_{width}/2 = y)$ and z_i is the center location of the quadrupole.

For a given beam entrance parameters into the HV-terminal were the quadrupole currents of Q1-Q4 optimized in order to satisfy optimal beam injection parameters (as given by eq. 3.4, 3.5) at the wiggler "virtual entrance point". The electron trajectories of the optimal beam in the quadrupoles and wiggler section are shown in Figs. 3.3, 3.4 for the election-optics parameters of the FEL design (Table 2.2). The procedure for determination of the wiggler "virtual entrance point" and the quad currents optimization is described in Appendix C.

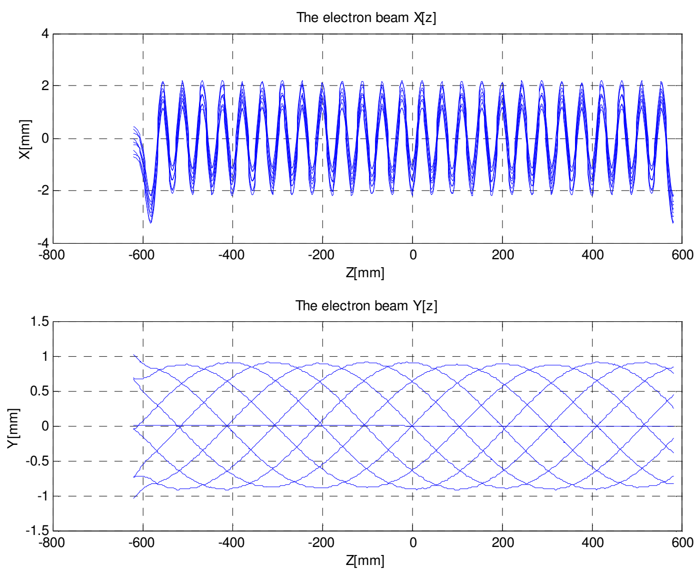

Fig 3.3 Optimal electron beam propagation inside the wiggler (ELOP simulation)

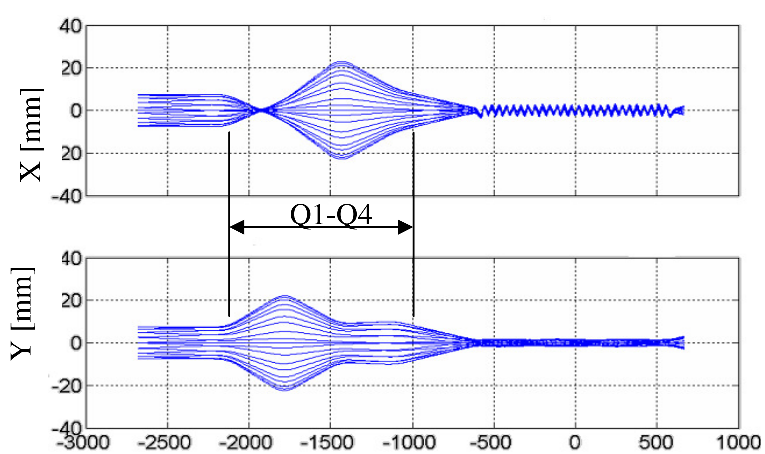

Fig 3.4 Optimal electron beam propagation inside the wiggler according to optimal chosen current values of the quadropols Q1-Q4 (ELOP simulation)

Non optimal electron beam cases betatron and scalloping oscillations of the electron beam inside the wiggler. The oscillation of an electron entering the wiggler off-axis in the x and y dimensions respectively is shown in Fig. 3.5. When a beam enters the on-axis but not with optimal beam injection acceptance parameters, the betatron oscillation of the individual electrons produces the “beam scalloping” effect inside the wiggler. This beam scalloping leads to current losses and resonator damages due to intercepted electrons, and also to FEL gain reduction, and to radiation frequency shifts. These effects will be studied in Chapter 5.

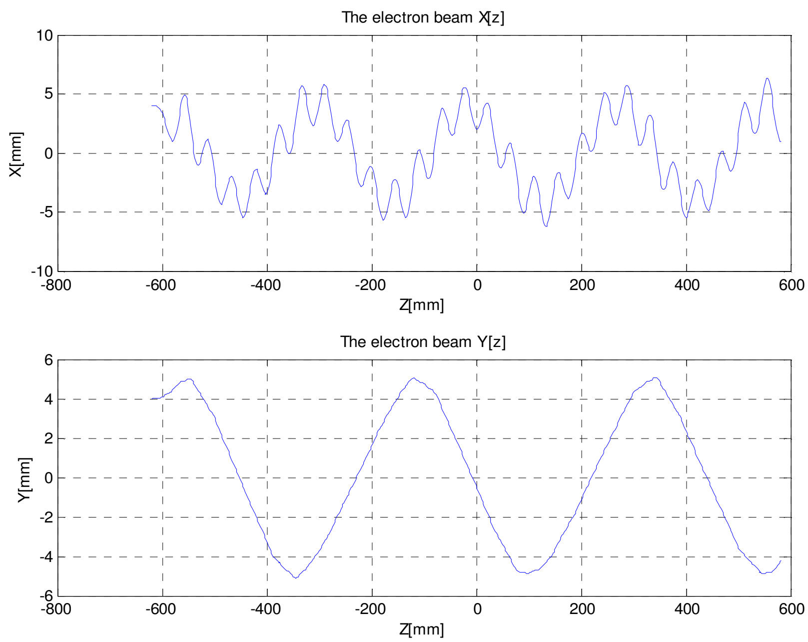

Fig 3.5 Betatron oscillation of the single off-axis electron inside the wiggler

3.2.3 Improvements in electron sampling algorithm for ELOP, GPT and other particle tracing simulation codes

The trajectories of electrons obtained by use of particle tracing codes depend on the initial distribution of electrons or macro-particles used in simulations. Due to the limited number of macro-particles which can be used in practice, particle codes have intrinsic statistical difficulties in modeling beams with multidimensional gaussian distributions, and particularly the tails of the gaussian distributions. In order to perform efficient electrons initial distribution a special code "BEAMDIST" was written (Volshonok M. et. al 2005) on a MATLAB base (see Appendix B).

The procedure applies for model of a uniformly distributed electrons distribution in phase-space ("water bag" model). It is compact also because it simulates only the electrons on the surface of the ellipsoid. This procedure applies also to a gaussian beam phase-space distribution, except that in this case the ellipsoid surface describes the *1/e* (or any other factor) phase-off point of the distribution.

The electrons should be evenly distributed on the surface of the four dimensional hyper ellipse in phase-space. An efficient algorithm for even 4-D sampling is proposed below (Averbuch A. et al 1997).

In the full 4-D electron distribution the electrons are distributed evenly on the surface of a 4-dimentinal ellipsoid schematically presented in Fig 3.6.

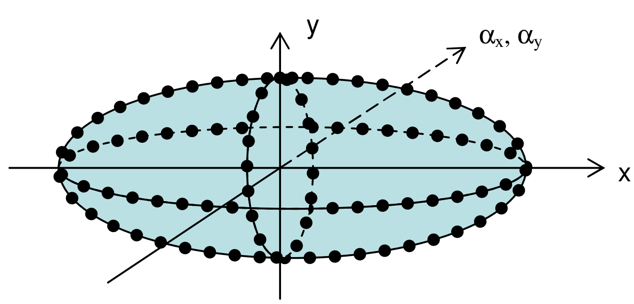

Fig 3.6 Illustration of the electron distribution on the phase-space ellipsoid

We position sampling particles only on the surface of the ellipsoid in order to save on sampling points. This is justified when our goal is only to find the envelope of the propagating beam. Due to Liounwill's theorem only the surface particle determine the beam on envelope (particle within the ellipsoid can never go out if have any transformation)

The ellipsoid equation is given by:

$$\left(\frac{x}{x_b}\right)^2 + \left(\frac{y}{y_b}\right)^2 + \left(\frac{\alpha_x}{\alpha_{xb}}\right)^2 + \left(\frac{\alpha_y}{\alpha_{yb}}\right)^2 = 1 \tag{3.6}$$

where *x, y, z* are the electron coordinates, $\alpha_x = v_x/v$, $\alpha_y = v_y/v$, x_b, y_b are the beam radii, α_{xb}, α_{yb} – are half width initial angular spread.

We use an assumption (Averbuch A. et al 1997), that the solutions of equation

$$\tilde{x}^2 + \tilde{y}^2 + \tilde{\alpha}_x{}^2 + \tilde{\alpha}_y{}^2 = n \tag{3.7}$$

where n is a large integer and $\tilde{x}, \tilde{y}, \tilde{\alpha}_x, \tilde{\alpha}_y$, are integers, gives the optimal (most even) sampling of the surface of a sphere of radius $\sqrt{n}$. Therefore for an ellipsoid we can use sampling as follows:

$$x_i = \frac{x_b \cdot \tilde{x}_i}{\sqrt{n}}; \alpha_{xi} = \frac{\alpha_{xb} \cdot \tilde{\alpha}_{xi}}{\sqrt{n}}; y_i = \frac{y_b \cdot \tilde{y}_i}{\sqrt{n}}; \alpha_{xi} = \frac{\alpha_{y_b} \cdot \tilde{\alpha}_{y_i}}{\sqrt{n}}; \text{ i=1…N}_\text{n}$$

where *Nn* is the number of solutions of (3.7) for given *n*. The set of solutions $(\tilde{x}_i, \tilde{y}_i, \tilde{\alpha}_{xi}, \tilde{\alpha}_{yi})$ with $i = 1...N_n$ found from (3.6) by the BEAMDIST code.

The 4-D sampling algorithm is the optimal way to sample and display the beam propagation features in a 4-D phase space. However, in order to save computation time, we have sometimes assumed that the *(x, x')* and *(y, y')* subspaces are uncorrelated. In this case we sample electrons only on the circumferences of the ellipses created by the intersection of the 4-D ellipsoid (Fig 3.6) with planes (x, α_x), (y, α_y), *(x,y)*: The cross-sectional sampling algorithm is simpler and requires only $N_{xx'}$+ $N_{yy'}$+ N_{xx}+ $N_{yy}+1$ particles. Instead BEANDIST, we use the following algorithm for electron sampling:

1) Phase-space plane (x, α_x), $(y=0, \alpha_y=0)$

$x_i=x_b cos\varphi_i$

$\underline{\alpha}_{xi}=\underline{\alpha}_{xb} sin\varphi_i$

$\varphi_i=2\pi(i-1)/(N_{xx'}-1)\ i=1\ldots N_{xx'}-1$

2) Phase-space plane (y, α_y), $(x=0, \alpha_x=0)$

$y_i=y_b cos\varphi_i$

$\underline{\alpha}_{xi}=\underline{\alpha}_{yb} sin\varphi_i$

$\varphi_i=2\pi(i-1)/(N_{yy'}-1)\ i=1\ldots N_{yy'}-1$

3) Phase-space plane (x, y), $(\alpha_y=0, \alpha_x=0)$

$\underline{x}_{xi}=\underline{x}_{yb} sin\varphi_i$

$y_i=y_b cos\varphi_i$

$\varphi_i=2\pi(i-1)/(N_{xy}-1)\ i=1\ldots N-1$

4) On axis electron $x_0=0,\ y_0=0,\ \alpha_{x0}=0,\ \alpha_{y0}=0$

This shorter algorithm usually with $N_{xx}=N_{yy}=0$ was used most of the time with the ELOP and the GPT tracing codes, and was found very useful for simulation time reduction.

3.2.4 Electron beam transport simulations in the acceleration and wiggler sections with GPT

3.2.4.1. Electrostatic accelerator modeling at the entrance and exit of the acceleration section

In the early commercial version of GPT, the accelerating field is modeled using a constant longitudinal electric field. However, this is a crude approximation, which neglects possible axial and transverse field variation of the fields, especially at the entrance and exit regions of the accelerator tube. In reality the axial accelerating field is not turned on abruptly at the location of the first electrode of the accelerating tube, but varies gradually as a function of z. Moreover, since the accelerator field needs to satisfy Laplace equation, the axial variation of the acceleration field $E_z(z,r)$ implies also presence and radial variation of a radial field $E_r(z,r)$. These fields are important because they give rise to parasitic focusing effects at the entrance to the acceleration tube and its exit. We use a theorem that makes it possible to describe the 3-D field vector of the solution of Laplace equation in cylindrical symmetry in terms of the axial field on axis and its derivatives. Again we take advantage of options in E-GUN in order to enable subsequent computations with GPT. The geometry of the acceleration tube electrodes and their corresponding DC potentials (determined by a series of HV resistors voltage divider placed along the acceleration column) are recorded in E-GUN one by one, and it is possible to use an option of E-GUN (Laplace) to get a full two dimensional (r,z) field map within the acceleration tube. Out of this data it is possible to extract specifically the potential distribution on axis, and derive from it the axial field variation $E_z(z,0)$ on axis along the tube. This data is sufficient in principle to calculate all radial and axial fields off axis (near the axis) by using a Taylor expansion of the field in terms of r in the Laplace equation.

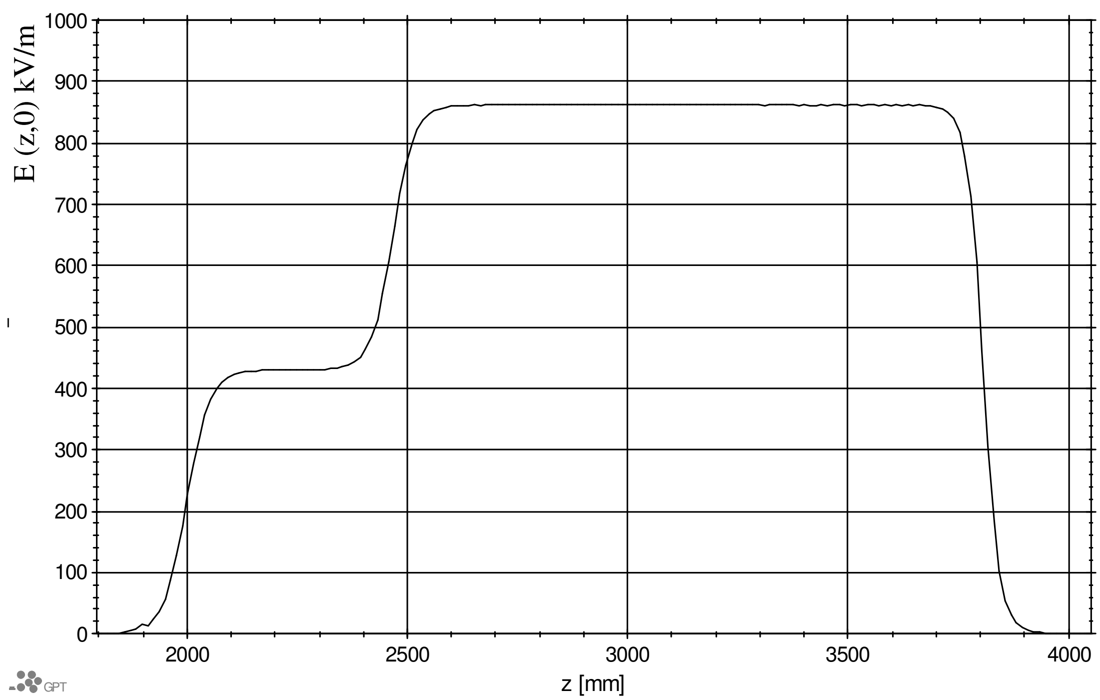

Fig 3.7 Result of the accelerator field on-axis electric field.

The off-axis axial and radial fields in the regions were there is axial field variation, and especially at the entrance/exit regions, can be calculated based on a Taylor expansion (Valentini M. 1997) of the axial field on axis:

$$E_z(z,r) = \sum_{k=0} (-)^k \frac{1}{(k!)^2} \left(\frac{r}{2}\right)^{2k} E(z)^{(2k)}$$

$$E_r(z,r) = \sum_{k=0} (-)^{k+1} \frac{1}{(k!)(k+1)!} \left(\frac{r}{2}\right)^{(2k+1)} E(z)^{(2k+1)} \qquad k = 0..2 \tag{3.8}$$

The new version of GPT that we have acquired has an option *map1D_E* to use this kind of expansion to calculate the 2D electric field near axis on the basis of the axial field data loaded into the program numerically.

Fig. 3.7 shows the axial field distribution on axis along a section starting before the tube (z=1794mm) and ending after the tube (z=4051mm) that was extracted from the EGUN LAPLACE calculation. The field in the first part of the acceleration seems to be smaller that in the rest of the tube (this is certainly a result of the way the resistors were set in the voltage divider in the original accelerator design).

Based on the data of the axial field distribution (Fig. 3.7) we were able to run GPT in the acceleration tube and the injector regions starting from the anode with an initial e-beam distribution as in Sect. 3.1.2. The GPT simulation results shown in Fig 3.7, 3.8b, are found to be in good agreement with the results of simulation with E-GUN - Fig 3.7, 3.8a. The focusing coils currents used in both the GPT and EGUN simulations of this example were: C1(1450 A·turns), C2(-11575 A·turns), C3(1260 A·turns), C4(840 A·turns)).

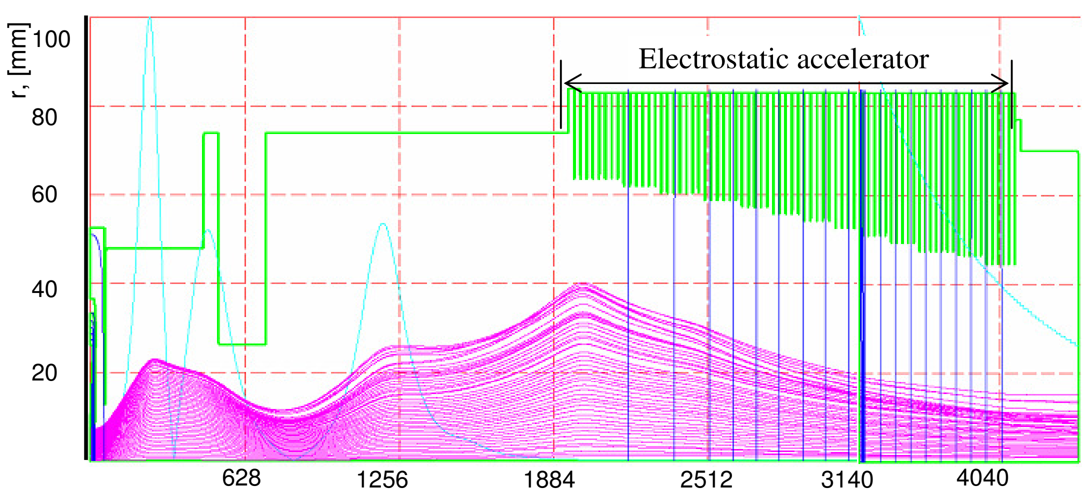

(a) E-GUN simulation of the electron beam propagation, from the cathode to the accelerator exit.

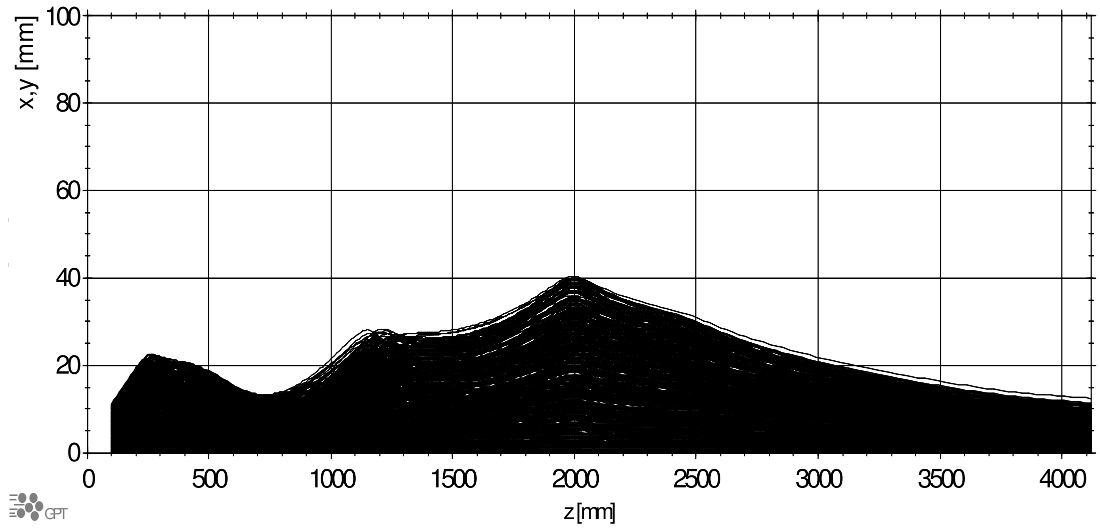

(b) GPT simulation of the electron beam propagation, from the electron gun exit z = 100mm to the accelerator exit.

Fig 3.8 (a),(b) Comparison between the E-GUN and GPT simulation results

3.2.4.2. GPT simulation of beam transport through the wiggler

While in the past we have used mostly ELOP in order o simulate the e-beam transport through the wiggler we have recently switched to simulation with GPT. The main reason for that were experimental measurement deviations from ELOP simulation predictions, which could be attributed to space-charge effects. These effects are not accounted in ELOP, but are taken into account in GPT.

In GPT computations, the field of the wiggler composed of rectangular permanent magnets is calculated as the sum of fields produced by a set of magnetic surface charge plates, each representing the surface of a pole piece of the real rectangular magnet of the wiggler. The field produced by a magnetic surface charge plate having coordinates $z' = 0, |x'| \le a/2, |y'| \le b/2$ (where a, b are dimensions of the plate), is given in compact form by (Valentini M. 1997).

$$\mathbf{B} = -grad\left[\frac{\mu_0 \sigma}{4\pi} \int_{-a/2}^{a/2} \int_{-b/2}^{b/2} \frac{dx'dy'}{\sqrt{(x-x')^2 + (y-y')^2 + z^2}}\right] \qquad (3.9)$$

where σ is the magnetic charge density at the pole piece surface. Dimensions "a" and "b", the location and orientation of each plate and the magnetic charge density (σ) on each plate is adjusted so as to reproduce the measured field of the actual wiggler are chosen so as to reproduce the field of the magnet block. The integrals and the gradient in Eq. (3.10) are calculated analytically. The wiggler field is then calculated as the sum of the magnetic field components of each magnetic plate. The field representation for each magnetic plate is thus obtained allowing for, the calculation of the total wiggler field. The space-charge calculation procedure is as already described in Chapter 3.1.3.

Contrary to previous calculations (Abamovich A. 2001), the GPT simulations show that the space-charge has a non-negligible effect also in the high energy part of the EA-FEL (E=1.4MeV, I=2A). The effect of space-charge is shown in Fig. 3.9a,b. Fig. 3.9a displays the GPT trajectories calculated without space-charge effect, with the current values of quadrupols Q_1 to Q_4 et according to produce the optimal beam injection parameters into the wiggler according to Eq. 3.4, 3.5. The electron beam propagates through the wiggler almost without scalloping. Fig. 3.9b displays the electron trajectories with the beam injected into the wiggler with the same conditions, but space charge option is taken into account. The electron beam propagates through the wiggler with quiet strong scalloping effect. This result shows, that it is important to take into account the space-charge effects in electron beam transport simulations of our FEL also in HV terminal.

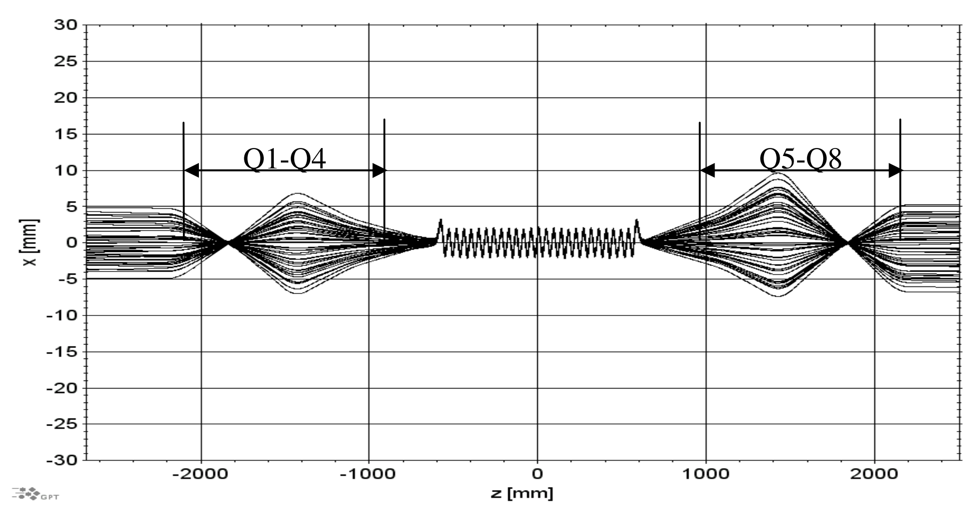

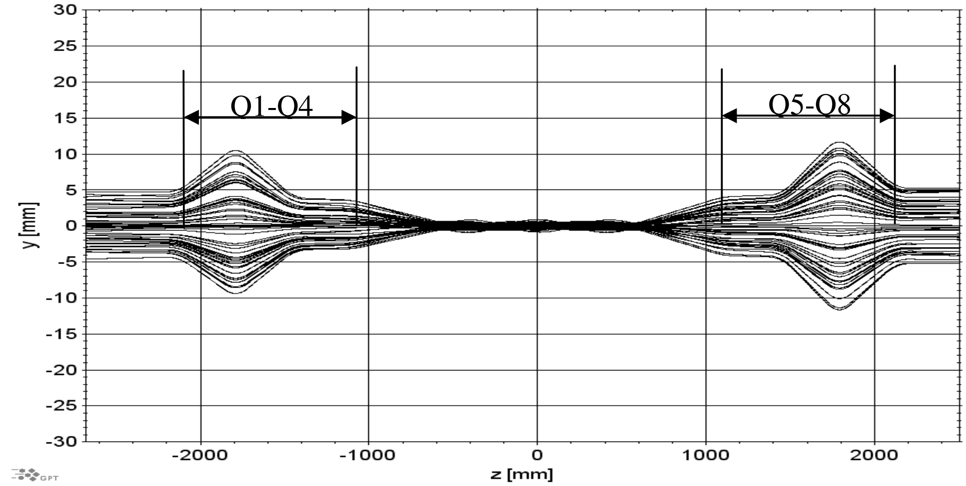

(a) GPT simulation of the electron beam propagation, trough the quadrupols and wiggler without space-charge effect

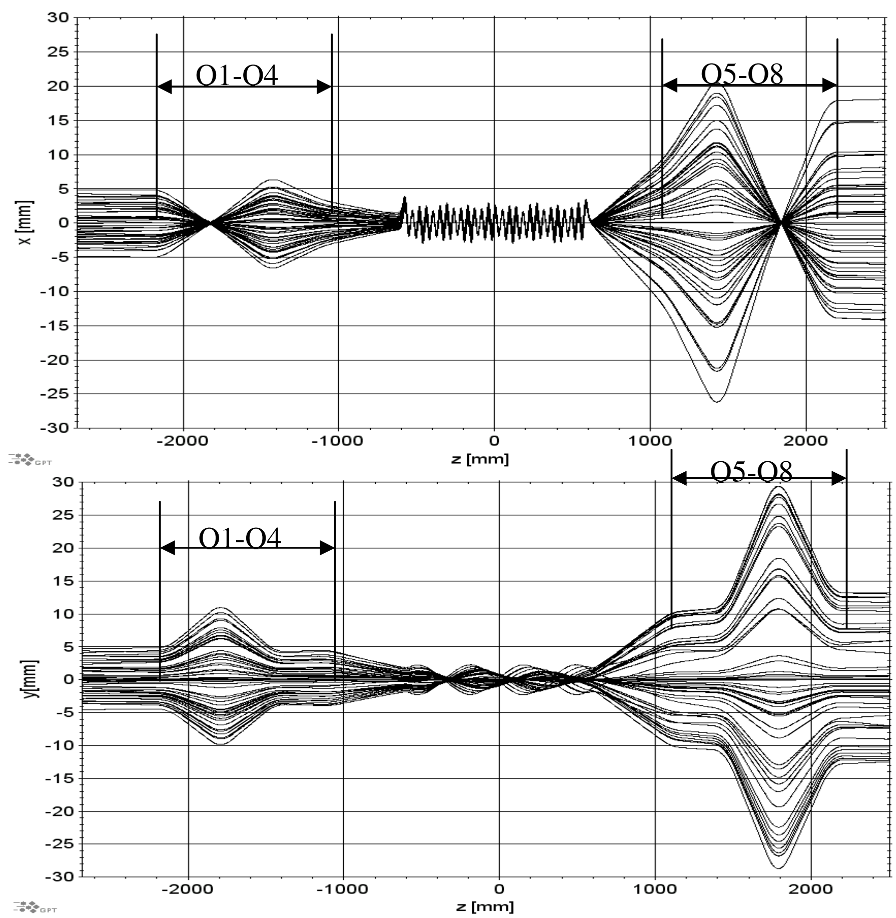

(b) GPT simulation of the electron beam propagation, trough the quadrupols and wiggler width space-charge effect

Fig 3.9 (a), (b) Space-charge influence on the electron beam transport

In order to check the simulation results we perform electron beam transport simulations from the cathode along the beam line. The electron beam diameters at S_1 and S_2 are calculated by GPT simulation. The electron beam crossection was monitored using the S_1 and S_2 screens; the beam current measured using three Pearson coils P_1, P_2, P_3 (see Fig 2.7, Table 2.4). The simulated electron beam dynamics in the high energy section was found to be in good agreement with experimental results (Appendix D).

Chapter 4 Experiments and measurements of the electron beam transport

4.1 The Electron gun

Measurements on the electron gun, described in 2.2.2 with a cathode STD 600 M-type (0.6'' diameter) were performed for a fixed cathode temperature of 1100°C and an anode – cathode voltage of V_{ac}=45 kV. The gun was pulsed with a pulse duration of t_p=13μs.
In the space-charge limited regime the electron gun current density is expected to follow the Child-Langmuir law for current density of a diode gun, (Langmuir and Irving 1923):

$$J_0 = 2.33 \cdot 10^{-6} \frac{V_g^{3/2}}{d^2} \; \left[A/m^2\right] \tag{4.1}$$

where: V_g-Grid potential [volt], d – distance from cathode to grid [m].
The cathode current is therefore:

$$I_c = \pi r^2 \cdot J_0 [A] = 2.33 \cdot 10^{-6} \pi r^2 \frac{V_g^{3/2}}{d^2} \; [A] \tag{4.2}$$

For the parameters of our gun (table 2.3):

$$I_c = 1.421 \cdot 10^{-6} \cdot V_g^{3/2} \; [A] \tag{4.3}$$

Fig 4.1 displays the characteristics of the cathode current $I_c = I_c(V_g)$ obtained in three different ways:

1. Prediction using the Child-Langmuir law (Eq. 4.3).
2. "E-GUN" simulations result carried out for various values of V_g for a fixed anode – cathode voltage V_{ac}=45 kV.
3. Laboratory measurements

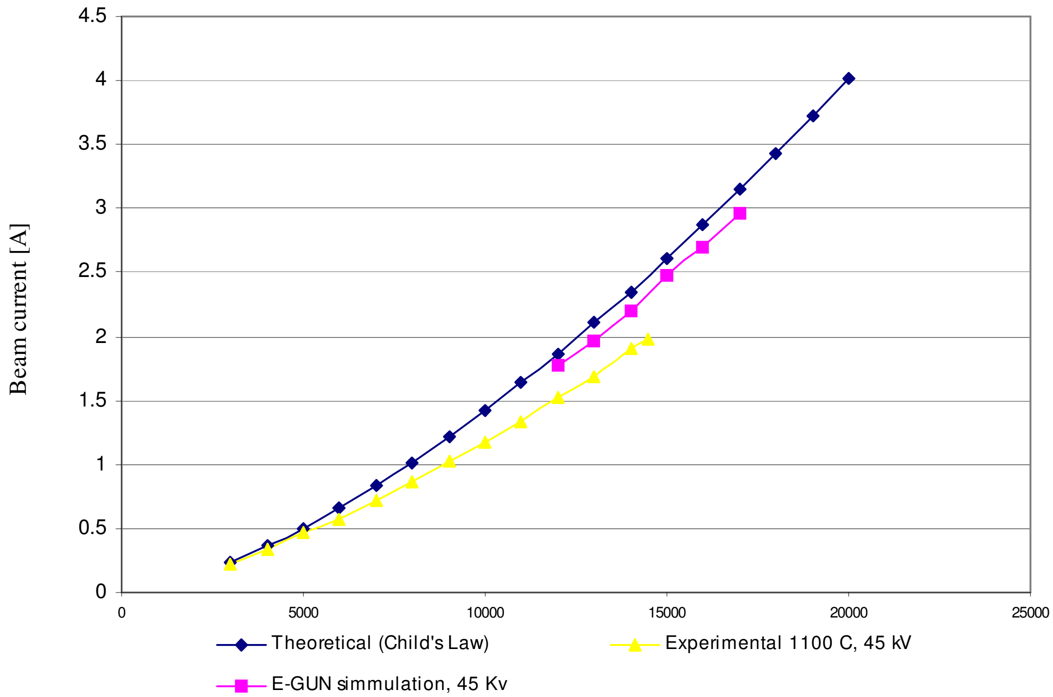

Fig 4.1 Electron gun current characteristics obtained experimentally, using E-GUN simulations and by using Child's-Langmuir low

The E–GUN simulations of $I_c(V_g)$ (Fig.4.1) is a little lower but close to Child-Langmuir law (Eq.4.3). The experimental results are lower than both predictions. A possible explanation: the grid–cathode spacing is in reality longer than 17mm (possibly e-gun flanges were not tightened face to face).

4.2 Stray magnetic fields in the injector section

In the 2m long injector section, stray (external) transverse magnetic field components have a non negligible influence on the electron beam transport, and on beam conditions at the entrance to the accelerator. In our injector section it is impossible to measure magnetic fields inside the drift tube without taking apart the e-gun. We measured the transverse and axial magnetic fields (geomagnetic and stray magnetic fields) along injector axis z as shown at Fig. 4.2 a,b. The results of background field measurements were inserted into the GPT program in order to simulate the stray field effect on the electron beam propagation. The effect of these fields on electron transport in the injector section is shown at Fig 4.3 a,b.

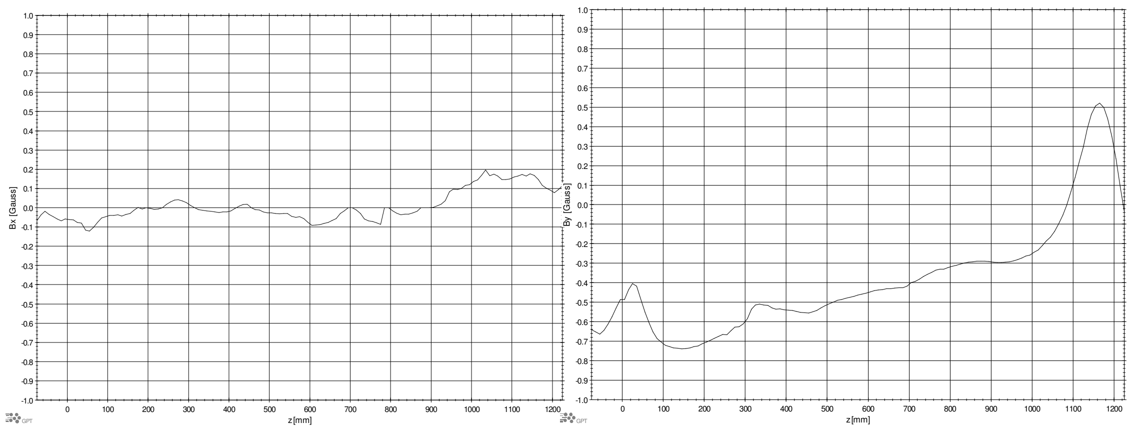

Fig 4.2 (a), (b) Results of the measurement of the stray magnetic fields B_x and B_y in the injector section

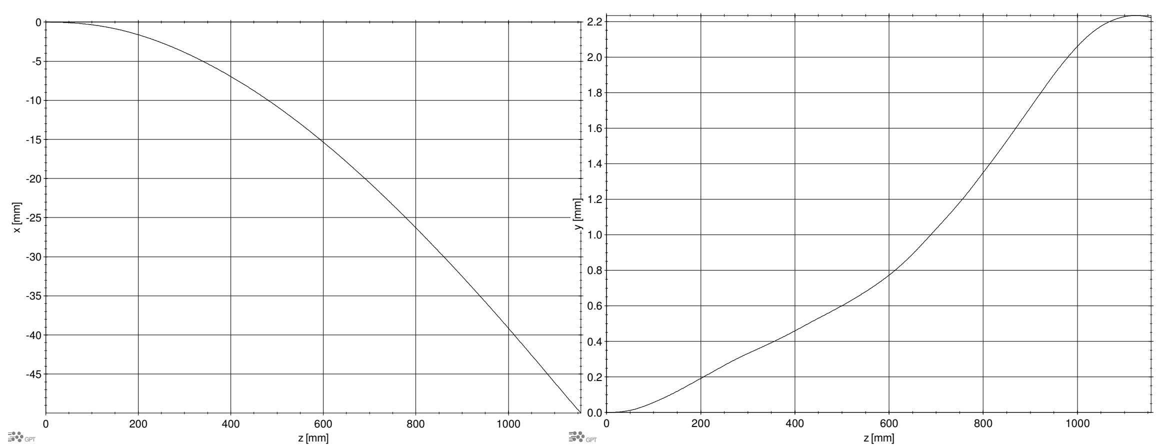

Fig 4.3 a, b Results of the effect of the stray magnetic fields B_x and B_y on the single electron propagation in the injector section

In order to compensate for the Earth magnetic field and for stray fields we introduced in the injector region Fig 2.2 two degaussing (Helmholtz) coils (HH, VH) , and three steering (H_1, H_2, H_3, V_1, V_2, V_3) coils . The use of these coils enables optimization of electron beam trajectory even if the stray magnetic fields are not determined accurately.

The beam line components which contain magnetic material (e.g. vacuum pumps) were screened with μ-metal cylinders. Fig.4.2 a,b shows the on-axis magnetic fields in the injector region, after screening the vacuum pumps and other magnetic elements near the beam line.

4.3 Electron beam emittance

A diagnostic screen S_1 was employed as a Pepper-Pot in order to measure electron beam emittance at the terminal. The S_1 screen (see Fig 4.4 a,b) is situated at the exit of the accelerator tube at 45 degree inclination when injected on the way of the beam. On the screen there are 35 holes, drilled in 45 degree angle to enable passage of e-beam beamlets. The distance between the holes is 5 mm on the screen plane in both the X and the Y directions. The central hole diameter is 1.5mm. Other hole diameters are 1mm. The electron beam penetrates trough the 1mm holes and passes the drift tube, until they hit the screen S_2, situated at distance L=1692mm ahead. We calculate the emittance from the size (d) of electron beamlet spots on screen S_1, and the distance L between S_1 and S_2 screens as follows: $\varepsilon =\sim \frac{D \cdot \alpha \cdot \pi}{4} \cdot mm \cdot mrad$, where D is the beam spot diameter at screen S_1 (~10mm), and α is the beamlet angular spread calculated from d and L as $\alpha = d / L$ (see Fig 4.5)

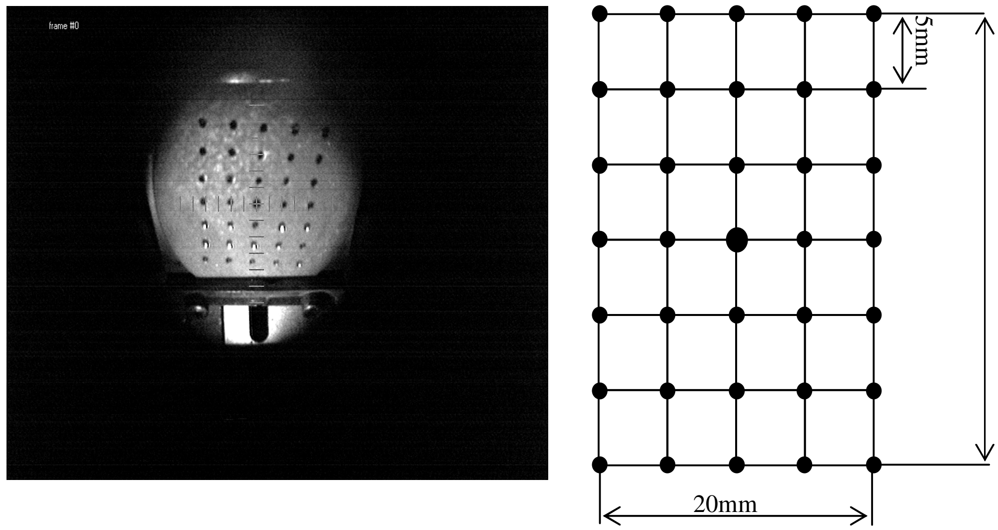

Fig 4.4a Photograph and schematic representation of the S1 diagnostic screen

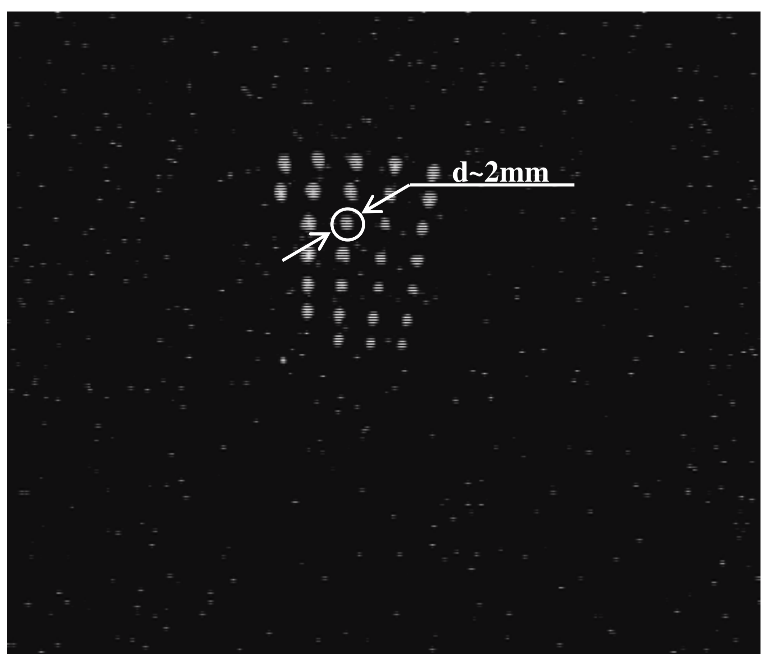

Fig 4.4b The spot diameters on the vertical axis of S2 screen is about~2mm

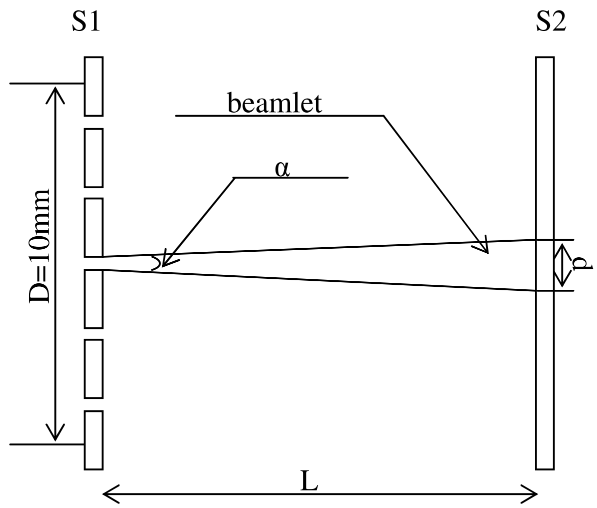

Fig 4.5 Electron beam angular spread calculation scheme

The value of the beam angular spread and therefore emittance was calculated according to D=10mm, d=2mm, α=1.18mrad is $\varepsilon = \sim 3\pi \cdot mm \cdot mrad$, and a normalized emittance value therefore $\varepsilon_n = \gamma\beta\varepsilon = 11\pi \cdot mm \cdot mrad$ (Einat M., Volshonok M. et al 2003).

4.4 Electron beam current through the FEL beam-line and to the collector

The beam current along the FEL beam-line was measured using three Pearson coils P_1, P_2, P_3 placed at accelerator tube exit, before the wiggler entrance, and after wiggler exit (see Fig 2.7, Table 2.4) and two-stage collector placed at the end of beam-line. The total beam current of 2A was measured at all Pearson coils (P_1-P_3) (Fig. 4.6). In order to calculate the beam current traveling through each Pearson coil from the oscilogram, the signal amplitude was multiplied to the specific calibration factor F for each Pearson coil (F_{P1}=0.01, F_{P2}=0.0831, F_{P3}=0.072)

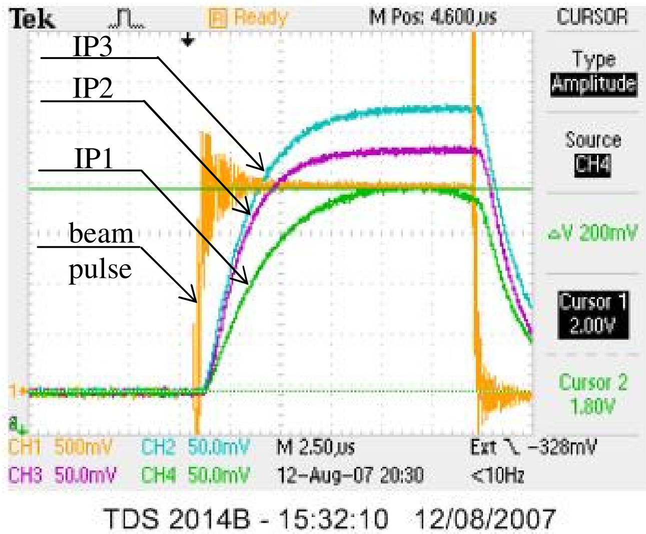

Fig 4.6 Oscilloscope measurements of the electron beam currents, which was measured at the Pearson coils

In order to measure the spectrum of the electrons, on the collector, several experiments were performed using two-stage collector is described in section 2.4.

The electric scheme of the two-stage collector is shown at Fig. 4.7. The first collector electrode CT1 is connected to the 11-th electrode of the accelerator tube Fig. 2.8, with the voltage about V_{11}=59kV. The second collector electrode CT2 is connected to CT1. To each collector was connected high voltage power supply (Hypotronics) as shown at Fig. 4.7. The electron beam current was measured using the Pearson coils with digital scope. Typical oscilograms are presented at Fig. 4.8.

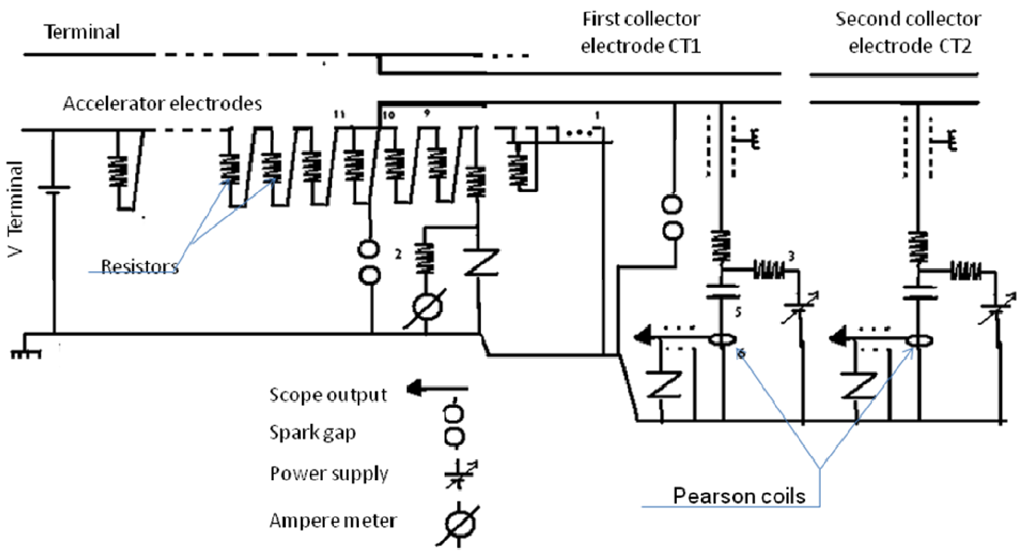

Fig 4.7 The electric scheme of the two stage collector connections

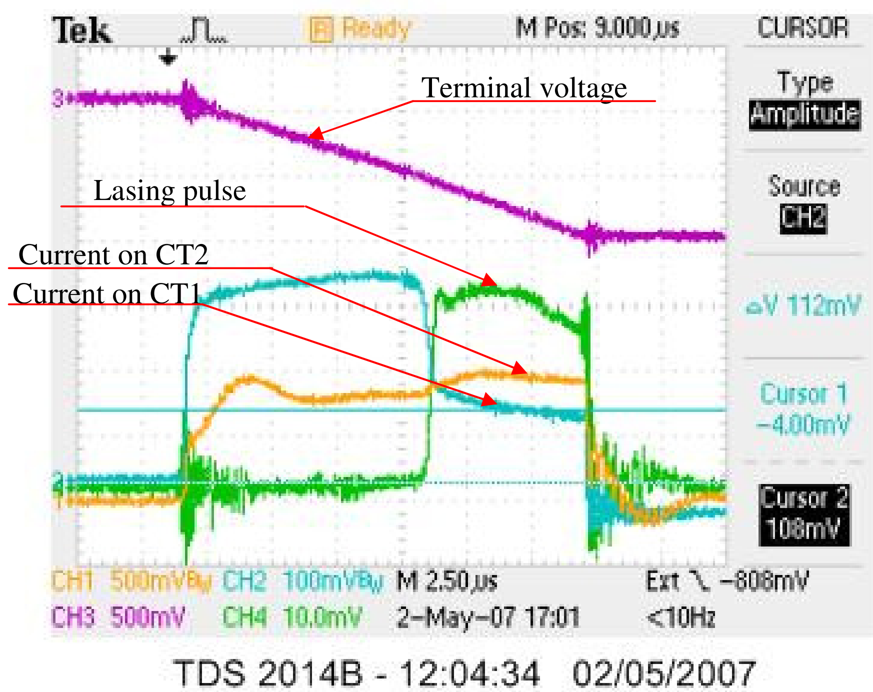

Fig. 4.8 Current measurements on two stage collector during the lasing

At the figure 4.9 presented a diagram of electron beam energy along the FEL beam-line: the red line presents a potential energy of the accelerator relative to the electron gun anode energy. The electron beam is emitted from the gun with the kinetic energy of 45kV (green line). During the interaction in the wiggler some electrons are accelerated (blue line) and some of the electrons decelerated (brown line). A distance between the blue and the brown line shows the spectrum of the electrons, which delivered to the collector.

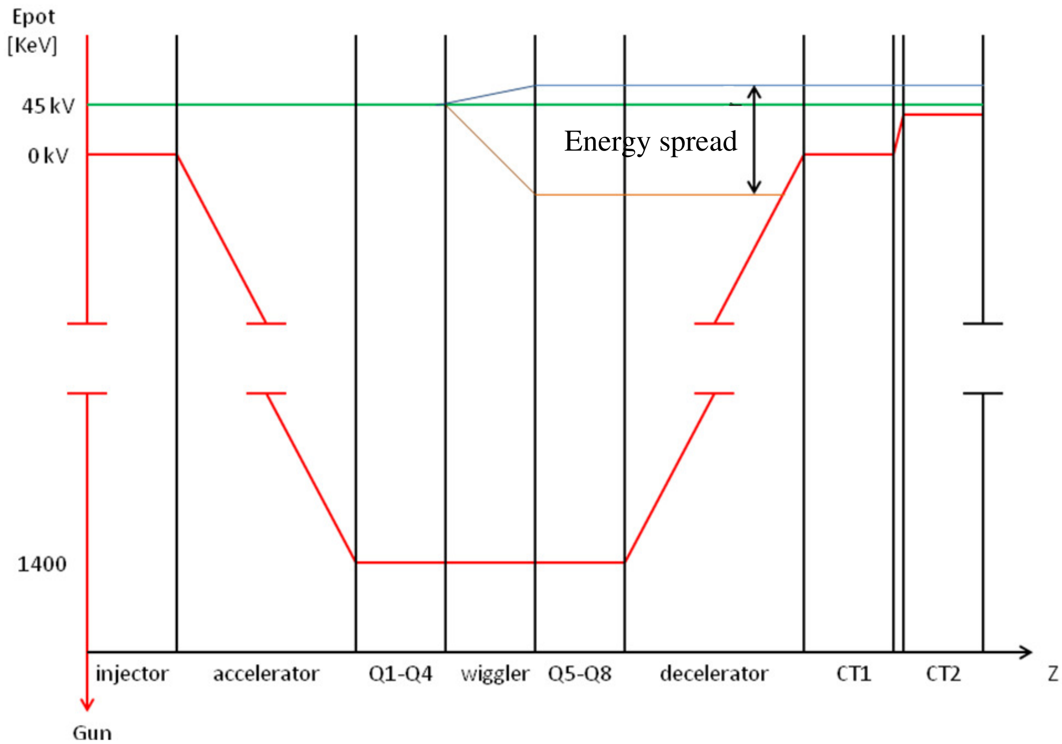

Fig.4.9 Diagram of the e-beam energy along the FEL beam-line

In order to measure the electron beam spectrum at the end of the FEL beam line the voltage on the CT1 and CT 2 was controlled using the power suppliers mentioned above. In order to prevent a breakdown only three values of the voltage was used on power supply connected toCT1 (5, 10, and 15 kV). For each specific voltage on CT1, the voltage on power supply, connected to CT2 was changed from 0 kV to -65 kV with step by 5 kV. The result of the experiment shown at Fig. 4.10 a,b,c.

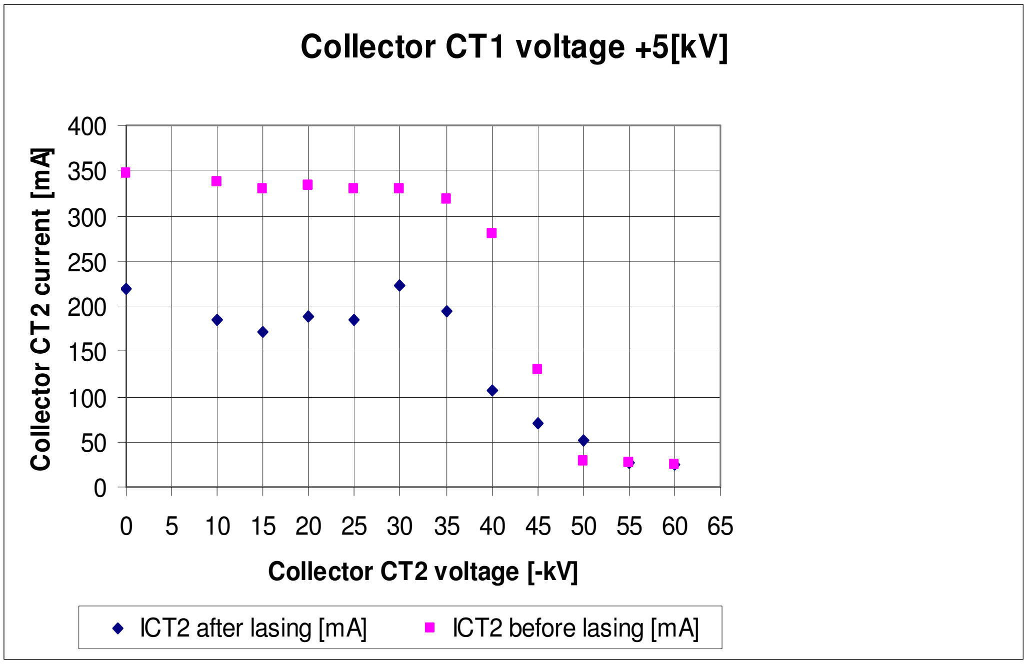

Fig. 4.10a collector CT1voltage +5[kV]

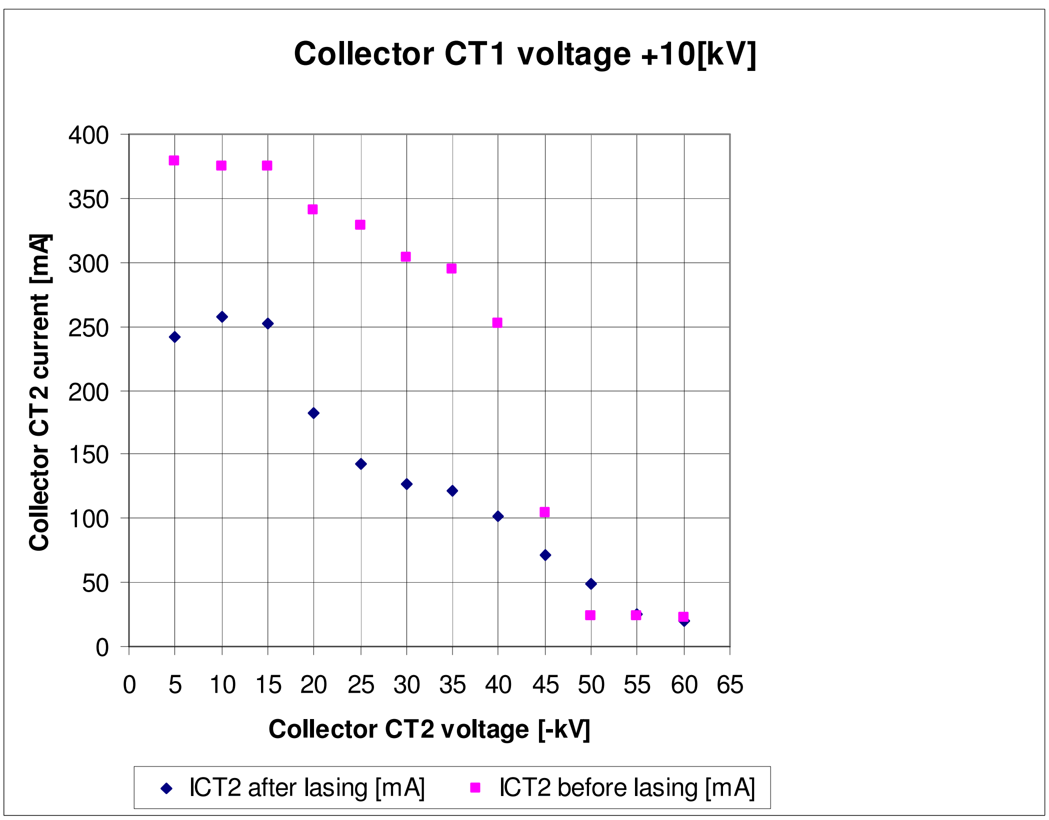

Fig. 4.10b collector CT1voltage +10[kV]

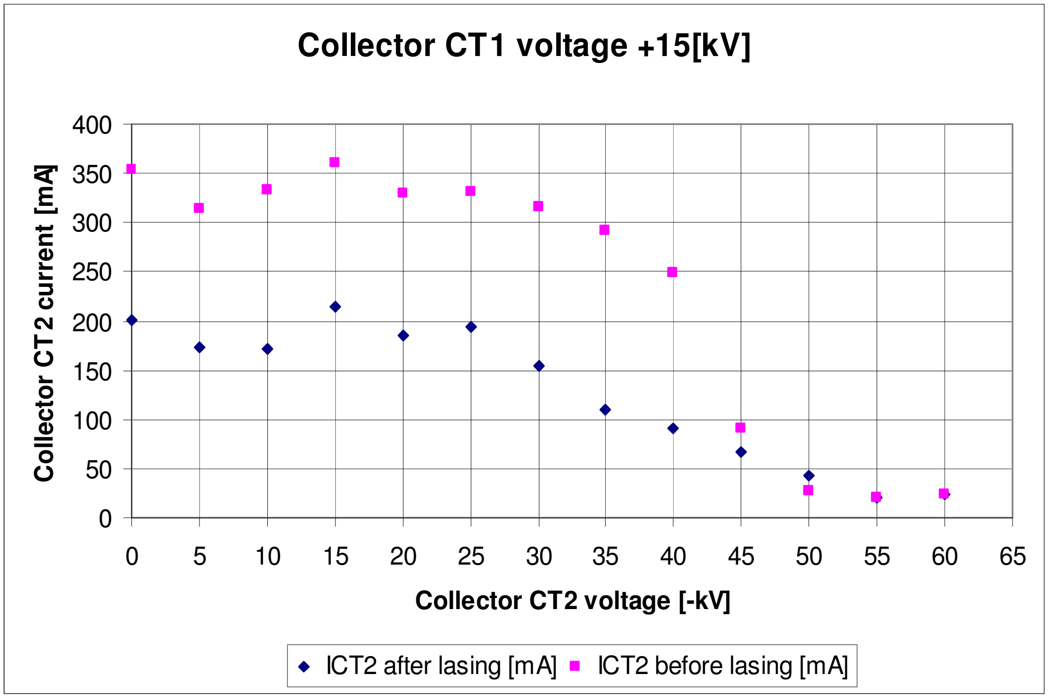

Fig. 4.10c collector CT1voltage +15[kV]

Fig. 4.10 Results of the electron beam current measurements with two-stage collector

The following phenomena were observed:

1) The current measured at the collector CT2 during the lasing is always less, than current measured before lasing in all measurements, because of the spent energy during the lasing. It happens due electrons backscattering into the deceleration tube.
2) We can see that the energy of the electron beam falls with CT2 negative voltage, but not sharp because of space-charge effect.

We can conclude that the electron beam transport from the deceleration tube to the collector is space-charge dominated, and therefore the electron current measurement is difficult and it is impossible to perform quantity analysis of the electron beam spectrum.

Chapter 5 Simulation and analysis of the spectral characteristics of spontaneous and laser radiation emission in the Israeli EA-FEL

One of the important properties of FELs its the ability to generate high power radiation within a wide tunable frequency range. By varying the electron beam energy in the range 1.3-1.44 MeV we tuned the FEL lasing radiation frequency was tuned between 80 GHz to 110 GHz. The tuning range is limited by the resonator frequency dispersion on one hand and by the e-beam energy depression of e-beam on the other hand.

The basic FEL operating parameters are predicted using the analytical expressions. Those and the results of FEL 3-D simulations (using the FEL3D code (Pinhasi Y. 1995)) match well the measured spectral characteristics of the FEL. The electron trajectories and the beam transport were calculated using GPT simulations in the space-charge dominated regime as well**.**

The basic FEL parameters including spontaneous and stimulated emission power are calculated. The effects of the electron beam emittance and of betatron oscillations on the FEL gain and lasing frequency are studied.

5.1 Spontaneous emission

The theory of spontaneous emission of the FEL resonator was developed by Pinhasi (Pinhasi Y. Lurie Y. 2002). According to this theory a random electron distribution in the e-beam causes fluctuations, (identified as shot noise) in the beam current. Electrons passing through a magnetic undulator emit partially coherent radiation, (undulator synchrotron radiation). The electromagnetic fields excited by each electron add incoherently, resulting in a spontaneous emission having a power spectral density (Pinhasi Y. Lurie Y. 2002):

$$\frac{dP_{sp}(L_w)}{df} = \tau_{sp} P_{sp}(L_w)\mathrm{sinc}^2\left(\frac{1}{2}\theta L\right) \tag{5.1}$$

where $P_{sp}(L_w)$ is the value of the spontaneous emission total power, $\tau_{sp} = \left|(L_w/v_{z0}) - (L_w/v_g)\right|$ is the slippage time and θ is the detuning parameter (v_{z0} is the axial velocity of the accelerated electrons and v_g is the group velocity of the generated radiation). The spontaneous emission null-to-null bandwidth is approximately $2/\tau_{sp} \approx 2(f_0/N_w)$. In a FEL, utilizing a magneto-static planar wiggler; the total power of the spontaneous emission is given by :

$$P_{sp}(L_w) = \frac{1}{8}\frac{eI_0}{\tau_{sp}}\left(\frac{a_w}{\gamma\beta_{z0}}\right)^2 \frac{Z}{A_{em}} L_w^2 \tag{5.2}$$

where $Z \approx 2\pi f\, \mu/k_z$ is the "mode impedance", and I_0 is the DC beam current. The expected value of the total spontaneous emission power generated in the resonator is given by $P_{sp}(L_w)/I_0 = 60\,\mu\mathrm{WA}^{-1}$.

At the resonator output, the spontaneous emission spectrum generated inside the resonator is modified by a Fabry–Perot spectral transfer function (Pinhasi et. al. 2003):

$$\frac{dP_{out}}{df} = \frac{T}{\left(1-\sqrt{R}\right)^2 + 4\sqrt{R}\sin^2\left(\frac{1}{2}k_z L_c\right)} \cdot \frac{dP_{sp}(L_w)}{df} \tag{5.3}$$

where L_c is the resonator (round-trip) length, R is the total power reflectivity of the resonator, T is the power transmission of the out-coupler and $k_z(f)$ is the axial wavenumber of the waveguide mode. The calculated spectrum of the spontaneous emission power of the present EA-FEL has a null-to-null bandwidth of 18 GHz.

The maxima of the resonator transfer function is given by $k_z(f_m) \cdot L_c = 2m\pi$ (where m is an integer), which defines resonant frequencies f_m of the longitudinal mode. The free-spectral range (FSR) (the inter-mode frequency separation) is given by $\mathrm{FSR} = v_g / L_c = 113\mathrm{MHz}$. The transmission peak is $T/(1-\sqrt{R})^2 = 1.6$ with full-width half-maximum (FWHM) bandwidth of $\mathrm{FWHM} = \mathrm{FSR}/F = 7.76\mathrm{MHz}$; where $F = \pi\sqrt[4]{R}/(1-\sqrt{R}) = 14.56$ is the Finesse of the resonator. The spectral line-shape of the spontaneous emission power, calculated at the resonator output of the EA-FEL, is shown in Fig. 5.1

The noise equivalent bandwidth is defined as the bandwidth of an ideal band-pass filter producing the same noise power at its output. The noise equivalent bandwidth of any single resonant longitudinal mode is $B = (\pi/2)\mathrm{FWHM} = 12.2\,\mathrm{MHz}$. Consequently, the spontaneous emission power of mode m is given by

$$P_{sp}^{out}(m) = \frac{T}{\left(1-\sqrt{R}\right)^2} \cdot \left.\frac{dP_{sp}}{df}\right|_{fm} B \tag{5.4}$$

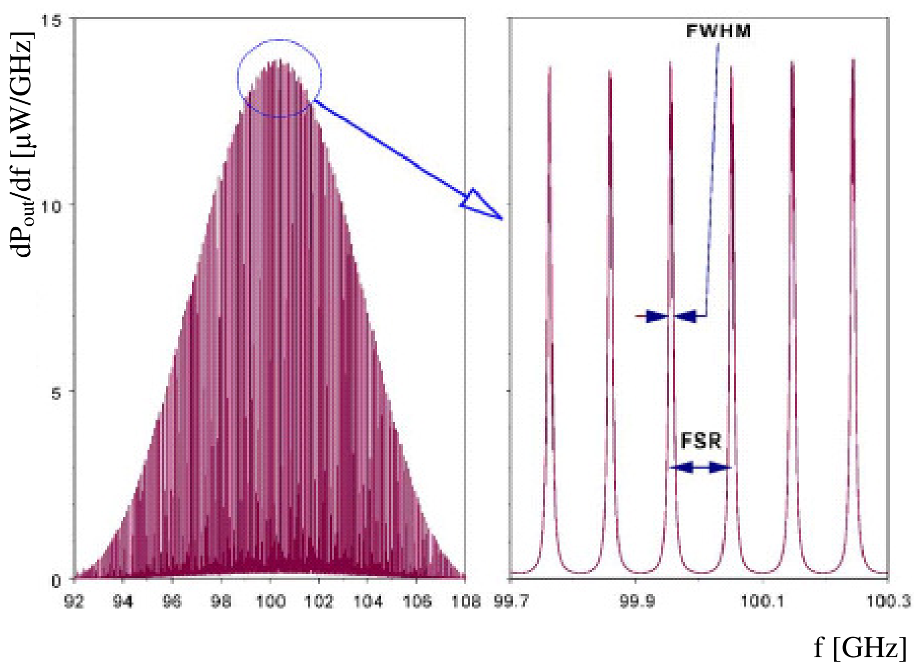

Fig. 5.1 Spontaneous emission power spectrum at resonator output

The typical bandwidth of the generated spontaneous emission power spectrum (Gover et al. 2004) is $1/\tau_{sp}$ = 9GHz. The number of longitudinal modes within the spontaneous emission bandwidth is then $N_{\mathrm{mod}es} = (1/\tau_{sp}) \cdot (1/FSR) \cong 80$. Thus the total spontaneous emission power measured at the output of the resonator is given as follows:

$$P_{out}^{sp} = N_{\mathrm{mod}es} P_{sp}^{out} m \cong \frac{T}{(1-R)^2} \cdot P_{sp}(L_w) \tag{5.5}$$

Using Eq. (5.2), we expect for 2A spontaneous emission power $P_{sp} \cong 120\,\mu$W to be radiated inside the resonator. From (5.5), the power emitted from the resonator out-coupler is reduced to $P_{out}^{sp} = 24\,\mu$W. The attenuation of the wave-guiding system, which delivers the power from the resonator, located inside the high-voltage terminal, to the measurement apparatus was measured to be 10dB.

Consequently, the spontaneous emission power expected at the detector is 2.4 μW (Gover et al. 2004).

5.2 Saturation power

At saturation the efficiency of energy extraction from an electron beam is given in terms of number of wiggler periods N_w by the approximate formula $\eta_{\mathrm{ext}} \approx \frac{1}{2\mathrm{Nw}} = 2.5\%$. The stimulated emission radiation power ΔP generated inside the resonator at steady state is therefore given by

$$\Delta \mathrm{P} = \eta_{\mathrm{ext}} \mathrm{E}_{\mathrm{k}} \mathrm{I}_0 / \mathrm{e} \tag{5.6}$$

which for beam current of I_0=2A, E_k=1.4MeV is ΔP~70kW. The power transmitted through the out-coupler is given by:

$$P_{out} = \frac{T}{1-R} \Delta P \tag{5.7}$$

and evaluated to be P_{out}=14kW for our system see Fig.2.1. Considering the attenuation of the transmission system, 1.4kW is expected at the detector.

Thus the FEL basic operating parameters calculated for our FEL are summarized in table 5.1.

Table 5.1 Basic calculated parameter of the FEL oscillator

Parameter	Symbol	Calculated value
Free-spectral range	FSR	113 MHz
Full-width half-maximum	FWHM	7.76 MHz
Finesse	F	14.56
Number of longitudinal modes	N_{modes}	80
Spontaneous emission output power	P_{out}^{sp}	24 μW
Stimulation emission output power	P_{out}	14kW

5.3 Study of emittance effect on the EA-FEL gain using of FEL 3D and GPT simulation codes

In order to predict the relation between emittance and FEL gain we used GPT code (Pulasr 2004) and a previously developed 3D, non-linear, single frequency code FEL 3D (Pinhasi Y. 1995). In this code it fields described in the frequency domain as an expansion in terms of transverse eigenmodes of the resonator. Assuming a uniform cross-section resonator, the total electromagnetic field at every plane z, can be expressed as sum of a set of waveguide transverse eigenmodes $\boldsymbol{\varepsilon}_q(x,y)$ with amplitudes $C_q(z)$:

$$\tilde{\mathbf{E}}(\mathbf{r}) = \sum_q C_q(z)\,\boldsymbol{\varepsilon}_q(x,y)\,e^{-jk_{zq}z} \tag{5.8}$$

Here the time-domain field is

$$\mathbf{E}(\mathbf{r},t)=\mathrm{Re}\left\{\tilde{\mathbf{E}}(\mathbf{r})\,e^{+j2\pi f_s t}\right\} \tag{5.9}$$

and $C_q(z)$ is the amplitude coefficient of transverse mode q, which can be obtained from the excitation equation:

$$\frac{d}{dz}C_q(z)=-\frac{1}{2N_q}e^{+jk_{zq}z}\iint\tilde{\mathbf{J}}(\mathbf{r})\cdot\boldsymbol{\varepsilon}_q^{\,*}(x,y)\,dx\,dy \tag{5.10}$$

In a single path amplifier model, the power of the electromagnetic field point z is given by:

$$P_{EM}(z)=\sum_q |C(z)|^2\,\frac{1}{2}\mathrm{Re}\{N_q\} \tag{5.11}$$

here N_q is the mode normalization power of the q mode.

In the theoretical model of FEL 3D (Pinhasi Y. Lurie Y. 2002) the electron beam consist of a number of sample charged quasi-particles, distributed in the beam volume. Therefore the excitation current can be given in the form:

$$\mathbf{J}(\mathbf{r},t)=-\sum_i q_i\,\mathbf{v}_i\,\delta(x-x_i)\,\delta(y-y_i)\,\delta[z-z_i(t)] \tag{5.12}$$

or in the frequency domain:

$$\tilde{\mathbf{J}}(\mathbf{r})=-2\sum_i q_i\frac{\mathbf{v}_i}{v_{zi}}\delta(x-x_i)\,\delta(y-y_i)\,e^{-j2\pi f_s t_i(z)} \tag{5.13}$$

Substitution of the simulated excitation current (5.12) into the excitation equation (5.10) enables one to re-write it as follows:

$$\frac{d}{dz}C_q(z)=\frac{1}{N_q}\sum_i\frac{q_i}{v_{zi}}\mathbf{v}_i\cdot\boldsymbol{\varepsilon}_q^{\,*}(x_i,y_i)\,e^{+j\left[k_{zq}z-2\pi f_s t_i(z)\right]} \tag{5.14}$$

In Eq. (5.12)-(5.14) q_i, $\mathbf{v}_i$ and $\mathbf{r}_i \equiv \{x_i, y_i, z_i\}$ are the charge, the velocity and the coordinates of particle number i;

$$t_i(z) = t_{0_i} + \int_0^z \frac{1}{v_{zi}(z')} dz' \tag{5.15}$$

Equation 5.15 is the time when for particle i arriving at point z.

The dynamics of each of the particles in the simulation is described by the force equation:

$$\frac{d\mathbf{v}_i}{dz} = -\frac{1}{\gamma_i}\left\{\frac{e}{m}\frac{1}{v_{zi}}\left[\mathbf{E}(\mathbf{r}_i,t) + \mathbf{v}_i \times \mathbf{B}(\mathbf{r}_i,t) + \mathbf{v}_i \frac{d\gamma_i}{dz}\right]\right\} \tag{5.16}$$

where the relativistic factor γ_i is found from

$$\frac{d\gamma_i}{dz} = -\frac{e}{mc^2}\frac{1}{v_{zi}}\mathbf{v}_i \cdot \mathbf{E}(\mathbf{r}_i,t) \tag{5.17}$$

Figure 5.2 displays schematically an FEL operated as an oscillator. For thus case part of the radiation emitted by the beam in a single path is reflected by mirrors and returned to the interaction region, and is forced to interact with new electrons in the driving current. The total electromagnetic field, emitted after N such round-trips of the radiation in the resonator, may be found from:

$$\tilde{\mathbf{E}}_{tot}(\mathbf{r}) = \sum_q C_{qN}^{tot}(z)\, \boldsymbol{\varepsilon}_q(x,y)\, e^{-jk_{zq}z} \tag{5.18}$$

Here the mode coefficient of the total field are given by

$$C_{qN+1}^{tot}(0) = \sum_q \rho_{qq'} C_{q'N}(z = L_w) \tag{5.19}$$

where $\rho_{qq'}$ are complex reflection coefficients, expressing the intermode scattering of transverse mode q', to mode q, due to the resonator mirrors. The coefficients of the field emitted after n round trips of the radiation at linear range are defined by the recursion relation:

$$C_{qN+1}(z=0)=\Gamma\, C_{qN}(z=L_w)\, e^{-jk_{zq}L_c} \tag{5.20}$$

where Γ is small signal gain.

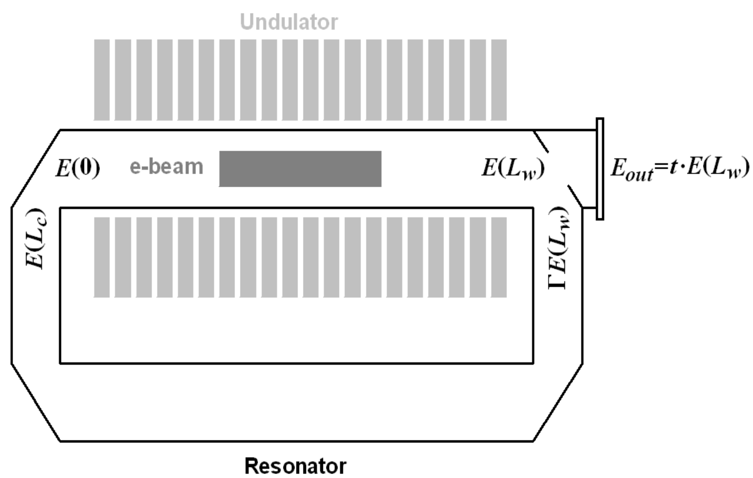

Fig. 5.2 Scheme of FEL operation in oscillator regime

The above equations form a closed set of non-linear equations, which enables the FEL 3D code to calculate both the radiated field and the trajectory of electrons up to saturation. The single frequency FEL 3D code does not fully describe the real oscillation build-up process in the resonator, since it does not include the multi-frequency longitudinal modes competition process. However if the oscillator arrives to single mode operation at saturation FEL 3D simulation provides adequate description of the radiative power extraction at saturation.

The initial particle distribution at the wiggler entrance that was used for FEL 3D simulation of the EA-FEL was generated with GPT code. The subroutine for a Gaussian distribution was employed as shown at Figure 5.3. The distribution in figure 5.3 models the initial electron distribution for the typical TAU-FEL (according to GPT model) electron beam parameters at the position of screen S_2 near the wiggler entrance. The parameters, used in the FEL 3D simulation are: beam energy $E = 1.4\text{MeV}$, emittance $\varepsilon = 3\pi \cdot \text{mm} \cdot \text{mrad}$ (see section 5.3) electron beam radius $r = 2\text{mm}$ (measured on screen S_2).

Signal path small signal gain calculations were carried out for various emittance values (Figure 5.4). The Figure 5.4 shows the FEL small signal gain dependence on emittance values; the other parameters are taken from Table 2.1. The red line corresponds to the measured emittance value ($\varepsilon = 3\pi \cdot \text{mm} \cdot \text{mrad}$) and its maximal gain value is G=2.8. As seen the emittance, has a significant influence on the FEL gain. So it is necessary to keep optimal electron beam propagation through the accelerator section. A non optimal electron-optics set-up can lead not only to physical damage of the wiggler and waveguide, but also to FEL gain reduction and to significant lowering of the FEL power (Volshonok M. and Gover A. 2007).

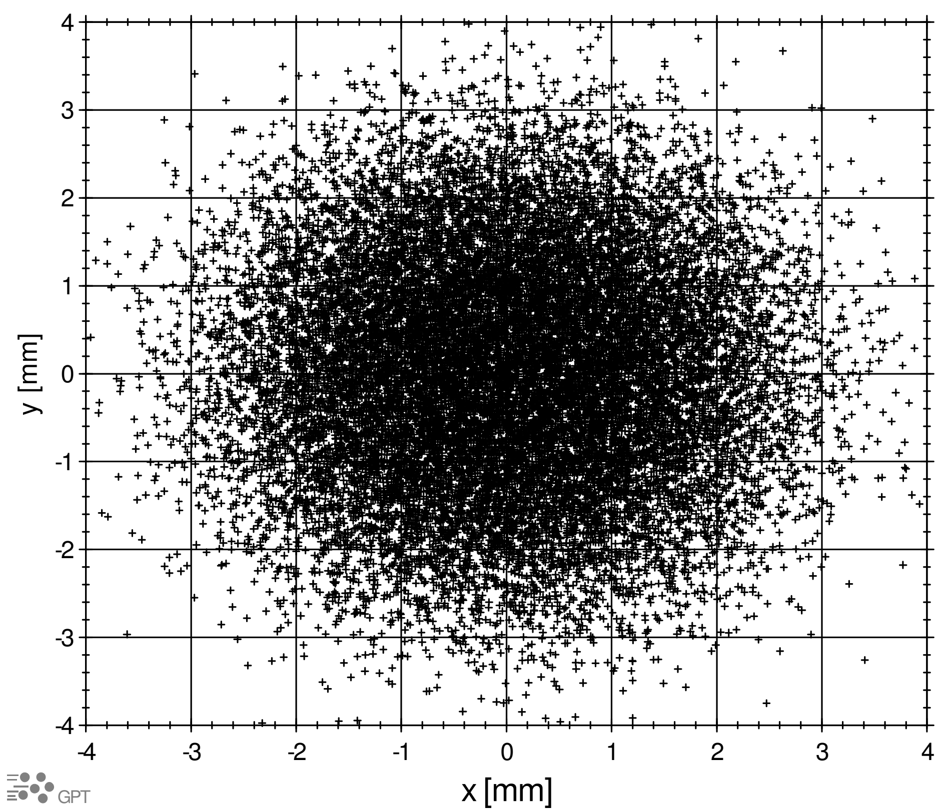

Fig. 5.3 Simulation electron distribution at the wiggler entrance with coordinates

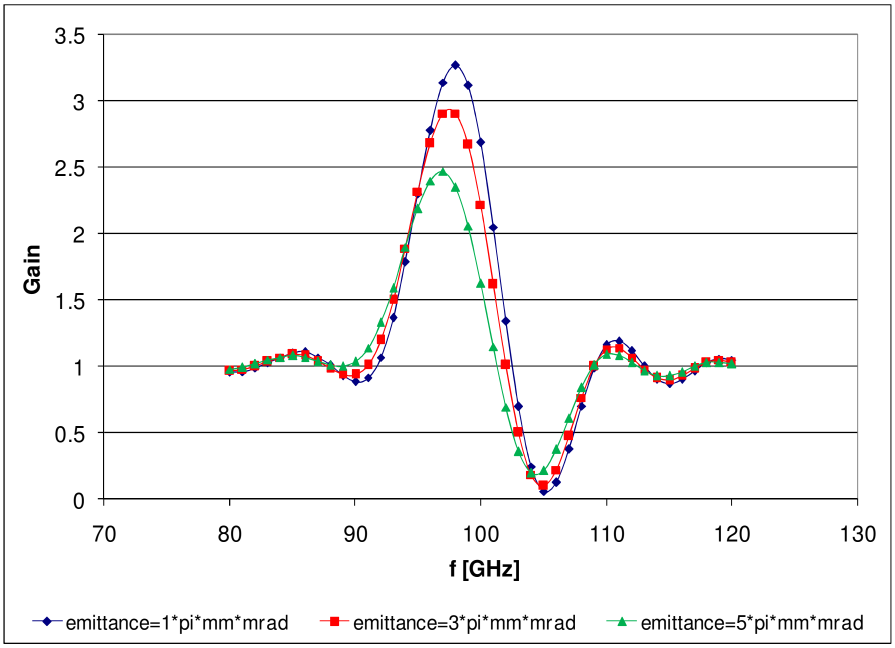

Fig 5.4 Electron beam emittance influence on the FEL gain

5.4 Effects of non optimal electron beam injection into the wiggler

The beam quality requirements inside the wiggler are in general stringent: The beam transport in the low and high energy sections is affected by space-charge and may provide emittance growth. The stray magnetic fields which were described in Chapter 2, steering errors and space-charge forces lead to non optimal condition of the e-beam at the wiggler entrance. Non-optimal beam injection into the wiggler leads to electron beam betatron oscillations, scalloping, and axial velocity spread and reduction.

In order to realize optimal electron beam propagation conditions inside the wiggler the electron beam has to keep the following parameters derived earlier in (Gover A., et al 1984): wiggling amplitude, and beam radii $X_{w,}$, r_{bx0}, r_{by0}. We calculate these parameters, according to (2.14, 3.4, and 3.5) for the TAU-FEL (table 2.1) and measured emittance $\varepsilon = 3\pi \cdot \mathrm{mm} \cdot \mathrm{mrad}$: X_w=*1.66mm*, r_{bx0}=*0.37mm,* r_{bx0}=*0.68mm*. In order to test the analytical calculation of the optimal wiggling amplitude we start an ELOP simulation with the single electron "omitted" from the wiggler center, where theoretically, due to symmetry, the electron should have its maximum wiggling amplitude. Setting at this point $x=-X_w=-1.68mm$, the electron should propagate in an ideal wiggler without betatron oscillation, along the wiggler axis. The electron motion was simulated with ELOP in the positive (+z) and negative (-z) propagating directions and its trajectory is shown in Fig. 5.5.

The following step taken is to check the calculated value for the optimal beam radii r_{bx0}, r_{by0}. We start now a multiple electrons beam at $z=0$, with the beam center sample electron set in coordinates $x=-X_w$, y=0. ELOP simulation without space-charge effect was carried out in the $-z$ direction with the given emittance and the calculated optimal beam radii given above. The sample electron trajectories of the beam are shown at Fig. 5.6. We can see that the electron beam propagates without scalloping, keeping constant width in both x and y dimensions. This simulation verifies the calculation of the optimal beam parameters in ideal wiggler.

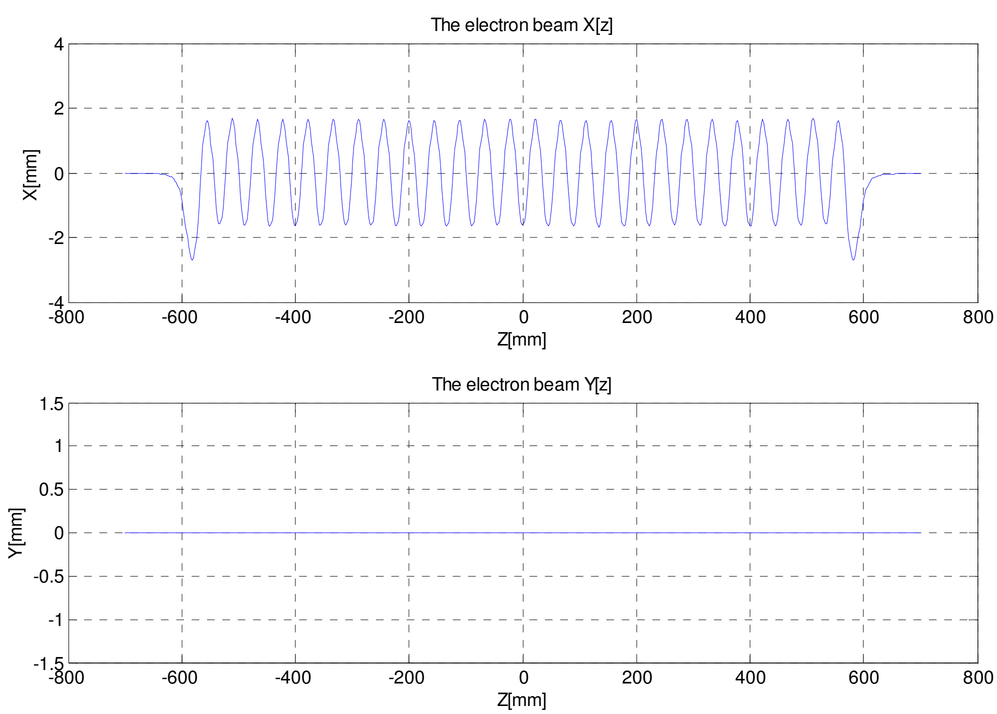

Fig. 5.5 On-axis single electron propagation indie the wiggler

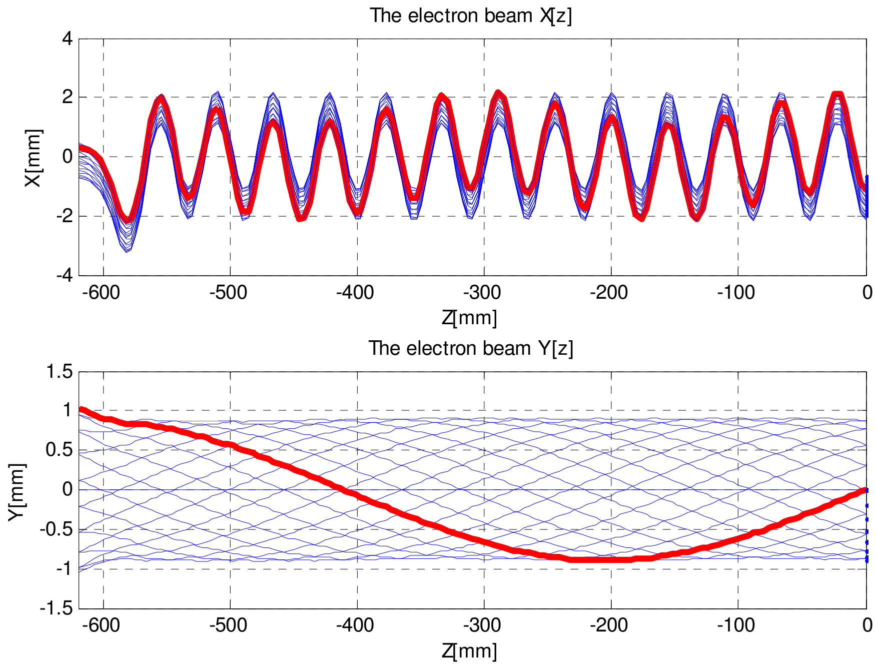

Fig. 5.6 Optimal electron beam propagation inside the wiggler

The effect of non-ideal beam injection into the wiggler was studied by simulations using the ELOP code developed at Tel-Aviv University (Abramovich A 2001). The effects are shown in Figs. 5.7, 5.8.

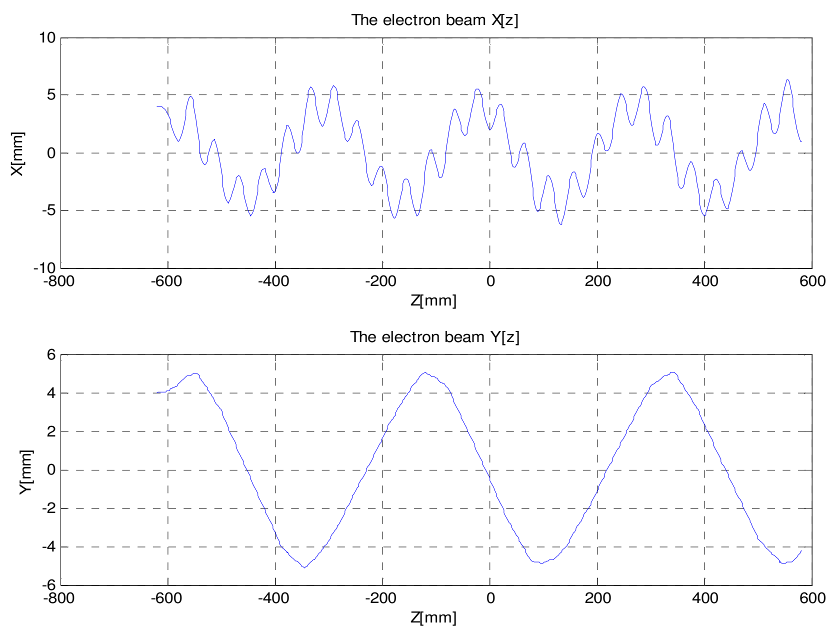

Fig. 5.7 Betatron oscillation of the single off-axis electron inside the wiggler

Fig 5.7 shows the betatron oscillation of a single electron. In this case the particle does not just wiggle around the axis as in Fig. 5.5, but experiences betatron oscillation with wavelength $\lambda_{\beta x} = 2\pi/k_{\beta x}$ in the *x* direction and $\lambda_{\beta y} = 2\pi/k_{\beta y}$ in the *y* direction, as shown in Fig. 5.7. The betatron wavelength can be calculated from the analytical expressions 2.13, 2.15.

Fig. 5.8 produced with ELOP simulation (no space-charge effect) shows the result of non optimal injection of the electron beam, into the wiggler. We can see scalloping of the electron beam, namely, periodic change of the electron beam radii during the propagation. In the next chapter we will study the effect of this non optimal matching on the FEL lasing frequency.

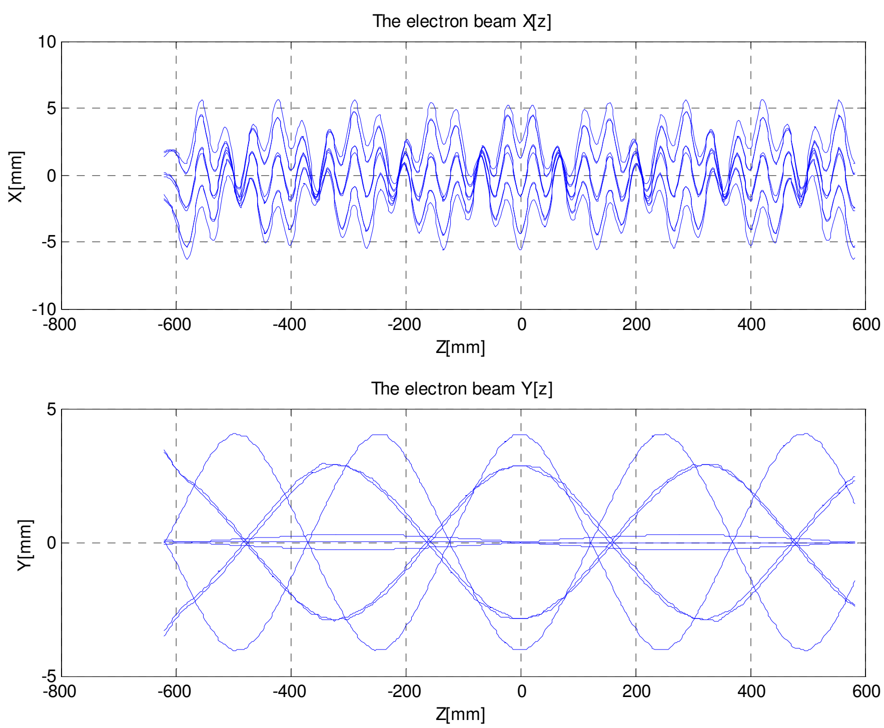

Fig. 5.8 Electron beam scalloping effect

5.5 Effect of imperfect electron beam transport through the wiggler on FEL lasing frequency

The off-axis injection of the electron beam or injection not at the waist, or with non-optimal radius according to formulas (3.4-3.5), produces excessive betatron oscillation and consequently beam scalloping and electron axial velocity reduction.

As was previously shown (Gover A., et al 1984), the axial electron velocity averaged over the synchrotron oscillation depended on total electron velocity, the velocity of the wiggling and the betatron oscillation amplitude (5.21). Increasing the betatron oscillation amplitude, decreases the average electron axial velocity:

$$v_{z0} \equiv v_z^2 - v_x^2 - v_y^2 = v^2 - \frac{1}{2}v_w^2 - \left(v_{x0}^2 + v_{z0}^2 k_{\beta x}^2 x_0^2\right) - \left(v_{y0}^2 + v_{z0}^2 k_{\beta y}^2 y_0^2\right) \qquad (5.21)$$

Where x_0, y_0, v_{x0}, v_{y0}, - the amplitudes of the betatron oscillation.

We analyze this effect using the ELOP simulation code. The average electron axial velocity was calculated from the simulation results (Fig 5.9-5.12). For sample electrons injected at different injection off-axis conditions: $\mathrm{v}_{z0} = \frac{z - z_0}{t(z)}$.

The FEL single mode lasing frequency in a resonator of multiple longitudinal modes is expected to take place at maximum single-path gain frequency this was calculated from an analytical expressions (Jerby E.and. Gover A. 1985).

In that paper it was shown, that in a waveguide resonator the maximum-gain frequency dependence on beam velocity is given by:

$$f_{\max} = \frac{\gamma_{z0}^2 \beta_{z0} c}{2\pi}\left(k_w + \frac{\overline{\theta}_{\max}}{L_w}\right)\cdot\left[1 \pm \sqrt{\beta_{z0}^2 - \frac{(2\pi f_{co})^2}{\left[\gamma_{z0}\left(k_w + \overline{\theta}_{\max}/L_w\right)c\right]}}\,\right] \qquad (5.22)$$

$\overline{\theta}_{\max}$ - the maximal gain of detuning parameter,

f_{co} - the cutoff frequency of the resonator waveguide

$\overline{\theta} = \left(\omega/\mathrm{v}_{z0} - k_z(\omega) - k_w\right)\cdot L$

We can estimate the average velocity of electrons injected into the wiggler off-axis by using ELOP simulation results. Using ELOP we calculated the average axial velocity of off-center electrons and the corresponding maximal gain frequency (Eq. 5.22) for the following examples (emittance ε=3π·mm·mrad, accelerating voltage V=1.4MeV):

a) Single electron at the envelope of the *x-z* trajectories of an optimally injected beam Figs. 5.6, 5.9, its path is marked in red.
b) Single electron with maximal (for the apertures of our system) vertical off-axis injection (Δy=4mm) Fig. 5.10a, b.
c) Single electron with maximal (for apertures of our system) horizontal off-axis injection (Δx=4mm) Fig. 5.11a, b.
d) Single electron having maximal vertical and horizontal off-axis injections (Δy=4mm, Δx=4mm) Fig. 5.12

The average axial velocity of the electrons is given by the blue curve. The simulation results of calculations are summarized it Table 5.1

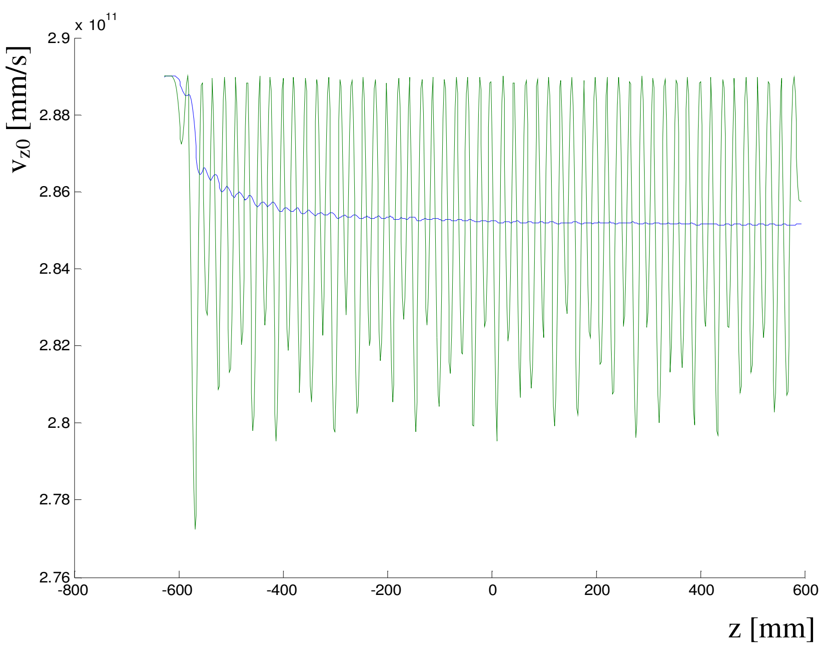

Fig. 5.9 ELOP calculation of the axial velocity of the single electron at the envelope of an optimally injected beam

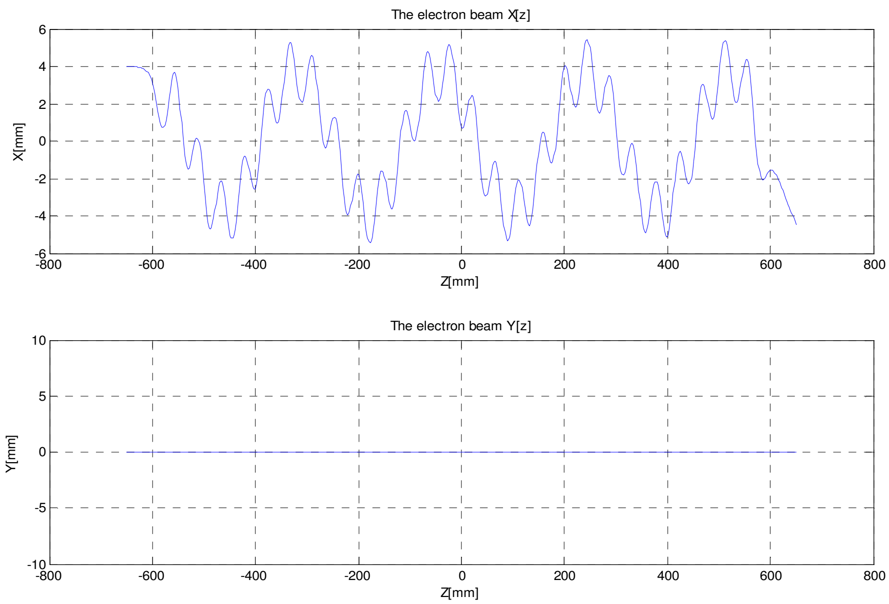

Fig. 5.10 (a) ELOP calculation of the of the single off-axis (x=4mm) electron trajectory

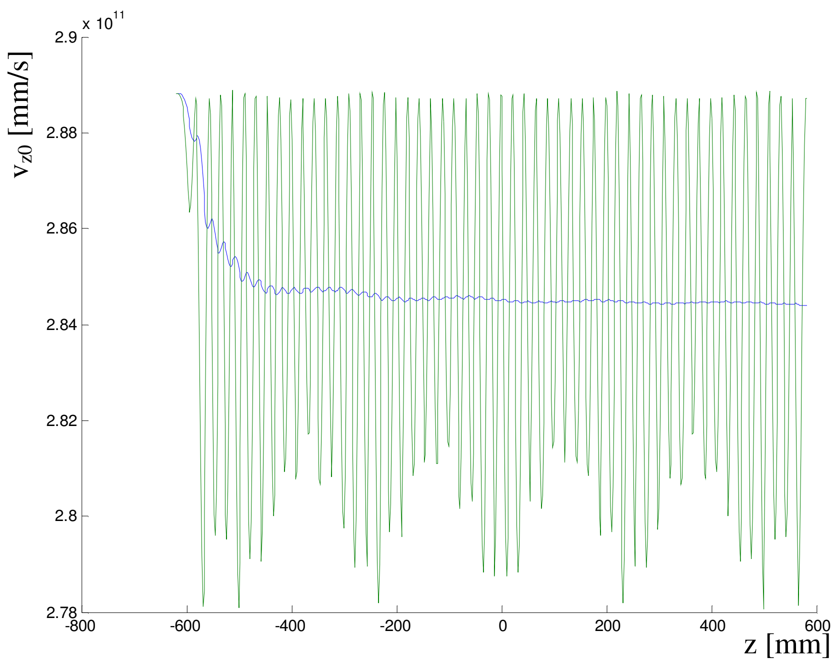

Fig. 5.10 (b) ELOP calculation of the axial velocity of the of the single off-axis (x=4mm) electron

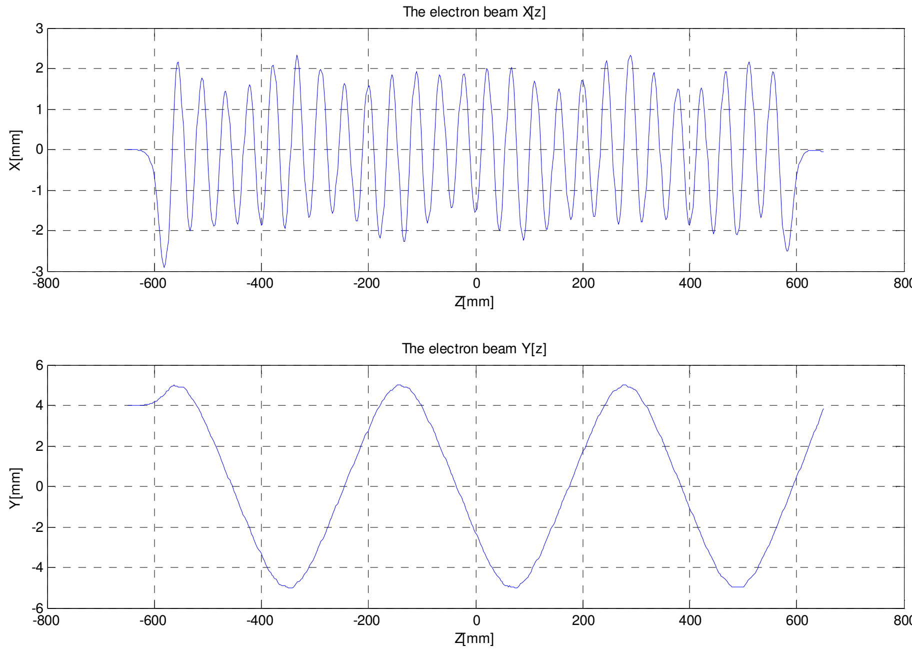

Fig. 5.11 (a) ELOP calculation of the of the single off-axis (y=4mm) electron trajectory

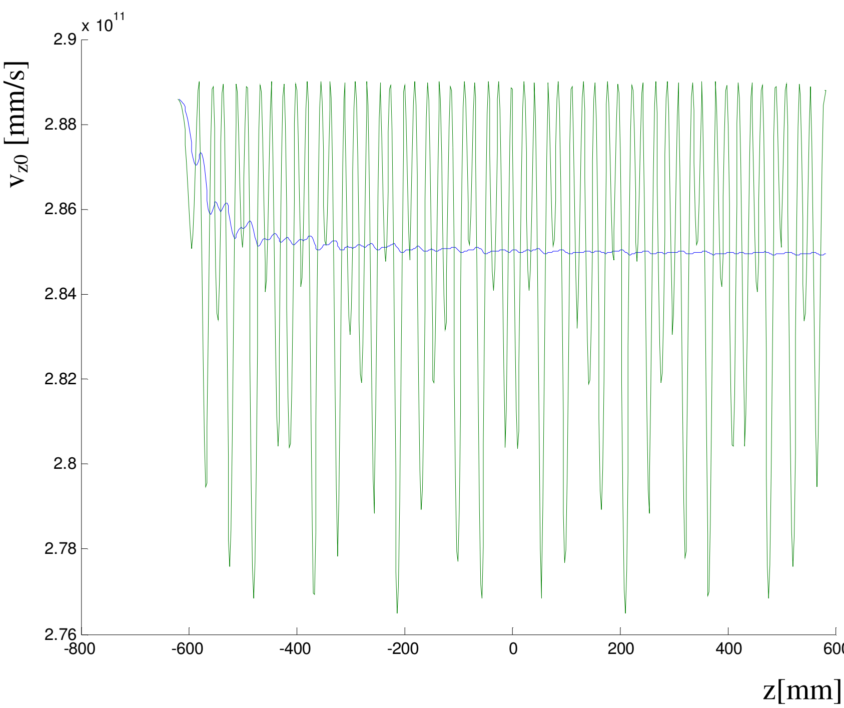

Fig. 5.11(b) ELOP calculation of the axial velocity of the of the single off-axis (y=4mm) electron

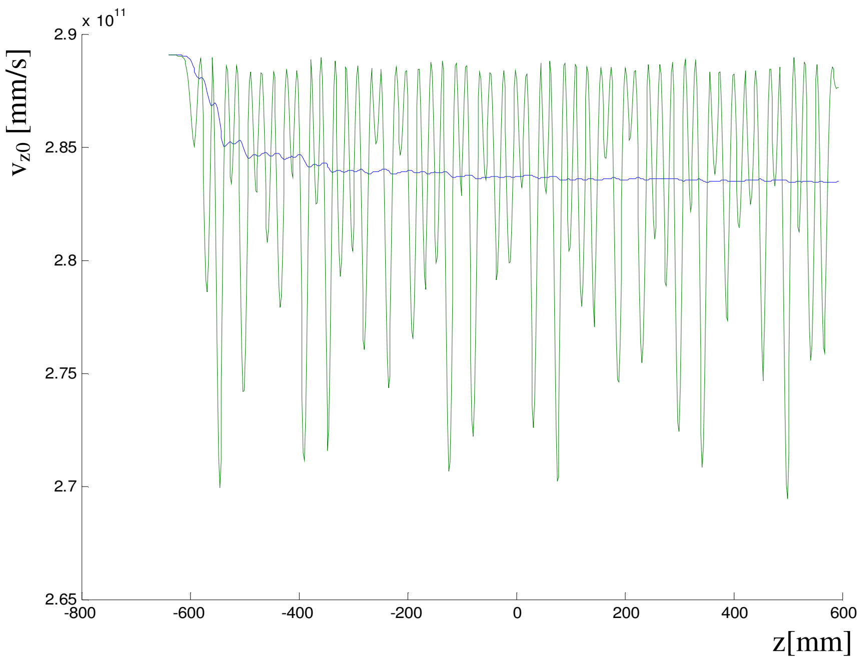

Fig. 5.12 ELOP calculation of the axial velocity of the of the single off-axis (x=4mm,y=4mm) electron

Table 5.2 Influence of the electron axial velocity on the FEL lasing frequency

	Accelerating energy [MeV]	Electron axial velocity [m/s]	FEL radiation frequency [GHz]
Optimal injection envelope	1.4	$2.8519 \cdot 10^8$	102
Vertical 4mm mismatch	1.4	$2.8455 \cdot 10^8$	97
Horizontal 4mm mismatch	1.4	$2.8450 \cdot 10^8$	96
Vertical and horizontal 4mm mismatch	1.4	$2.8361 \cdot 10^8$	88.5

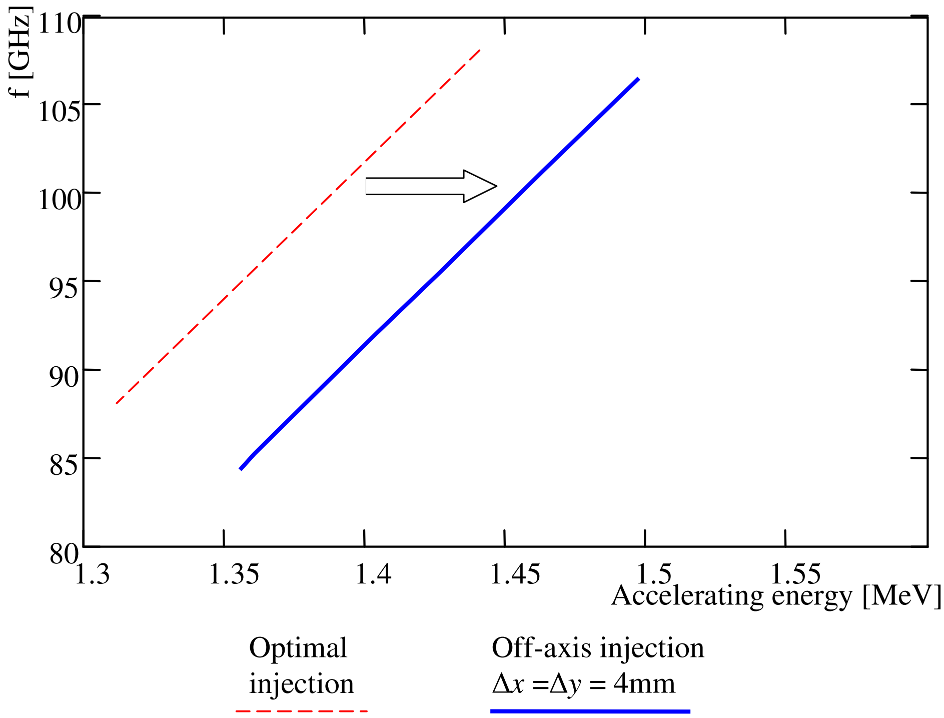

Fig. 5.13 FEL lasing frequency shift due to off-axis electron displacement

Fig. 5.13 shows the FEL lasing frequency down-shift, that corresponds to electron most extreme (x=y=4mm) off-axis injection. We can see, that the FEL lasing frequency curve shifts to a lower frequency range (Volshonok M. and Gover A 2007). This calculation matches well the measured FEL lasing frequencies as will be described in section 6.2 Fig.6.4.

Chapter 6 Measurement of characteristics of the EA-FEL radiation

In the present FEL, the millimeter -wave radiation in resonator is separated from the electron beam by means of a perforated Talbot effect reflector (Kapelevich B et al. 2003, Gover A., et al. 1984). A quasi-optic system transmits the out-coupled radiation power through a window in the pressurized gas accelerator tank and to the user's rooms by means of a corrugated overmoded waveguide.

The measurements were performed by two means: (a) power measurements using a *W*-band detector Millitech DXP-10; (b) spectral measurements using a HP-423 detector, heterodyne mixer of Hughes-47496H-100 with local oscillator (LO) from a HP-8797D network analyzer. In both cases, a Tektronix TDS-784A oscilloscope was used to monitor the output. The input signal was attenuated in order to scope with the limited dynamic range of the detectors and prevent breakdown of the detectors. The experimental set-up is presented at Fig 6.1.

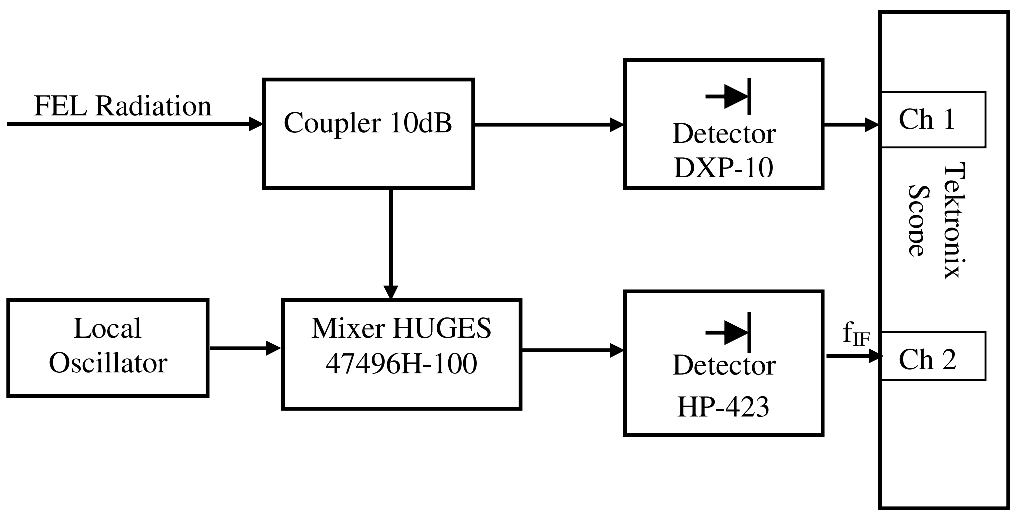

Fig. 6.1 Experimental set-up for the FEL frequency measurements

A W band downconverter, based on waveguide mixer and stable local oscillator (LO), produces on the scope the intermediate frequency (IF):

$$f_{IF} = f - f_{LO} \tag{6.1}$$

where f_{LO} is the local oscillator (LO) frequency. There is no distinction in the measurement between negative and positive frequencies, and what is seen on the oscilloscope is a signal of frequency $|f_{IF}|$.

6.1 Spontaneous and stimulated emission power

The accelerating voltage was varied from 1.3 MV to 1.5 MV in order to tune the FEL radiation frequency in the W-band. The electron beam current passing through the wiggler was measured to be 2A (99.9% of the injected current).

A spontaneous emission power of 2.0 μW was measured at the detector, that corresponds to 2.4 μW expected at the detector according to calculation in Chapter 5, Table 5.1. The traces shown in Figure 6.2 show the electron beam current pulse and the signal obtained at the detector video output correspond to the measured spontaneous emission RF power.

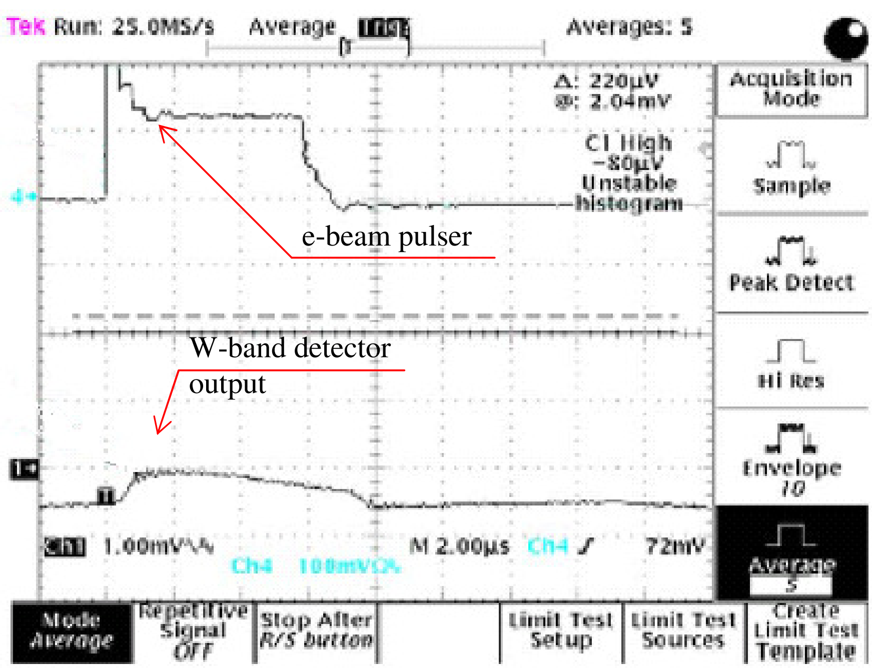

Fig. 6.2 Spontaneous emission power measurements

First lasing of the TAU EA-FEL using the configuration shown in Fig. 2.1 was observed by us in august 2003 (Gover et. al 2004). Figure 6.3 shows maximal measured radiation at the end of the optical transmission line. The Maximal measured power was 900W at 97.2GHz.

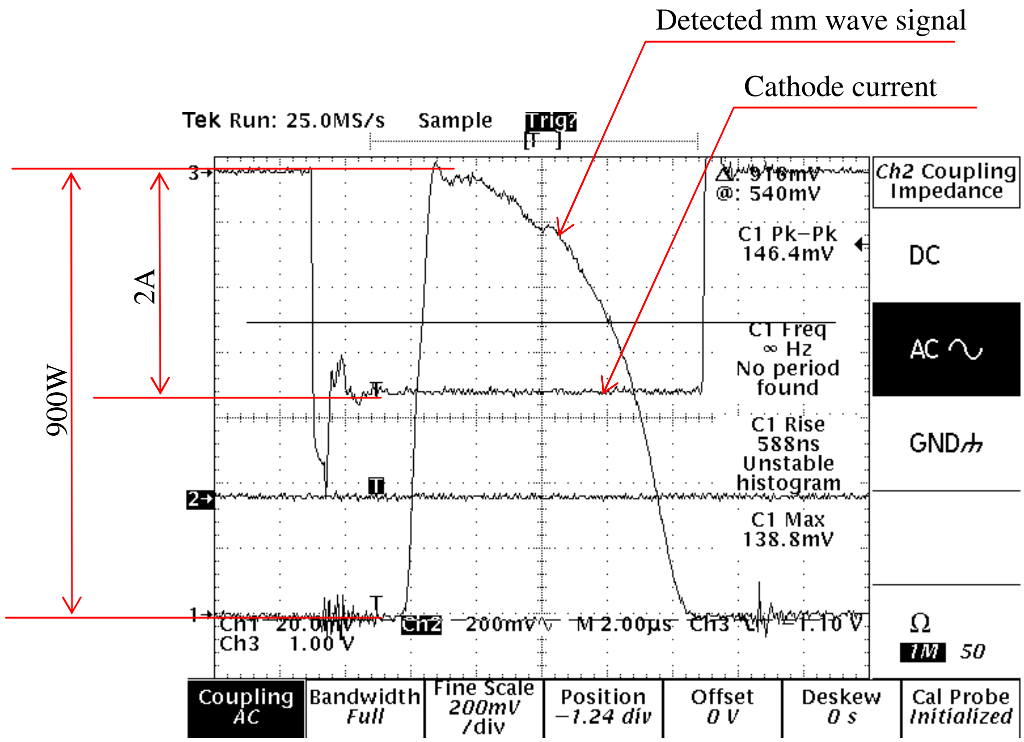

Fig. 6.3 The maximal measured power of the FEL radiation

6.2 Frequency tunability range

In order to measure the FEL tunability range the accelerating voltage of the FEL was varied from 1.3 MV to 1.5 MV, and the FEL radiation frequencies were measured using the setup shown in Fig. 6.3, the FEL tunability range was measured to be between 84GHz – 107GHz. The results of the FEL frequency measurements for different electron energy values (tunability range) are summarized in Table 6.1 and displayed in Fig. 6.4. These results agree well with calculations of the FEL frequency, performed using the analytical expression (5.22) with the v_{z0}, γ_{z0} calculated with consideration of the velocity reduction effect due to off-axis beam entrance into the wiggler (section 5.4). The velocity of the single electron was calculated for vertical and horizontal off-axis injections (Δy=4mm, Δx=4mm) Fig. 5.12

Table 6.1 FEL frequency tunability range

Accelerating voltage [kV]	Measured frequency [GHz]	Calculated frequency [GHz]
1.355	84.45	84.32
1.360	85.13	85.18
1.404	93.51	92.0
1.427	97.2	95.6
1.463	99.92	101.3
1.496	106.5	106.5

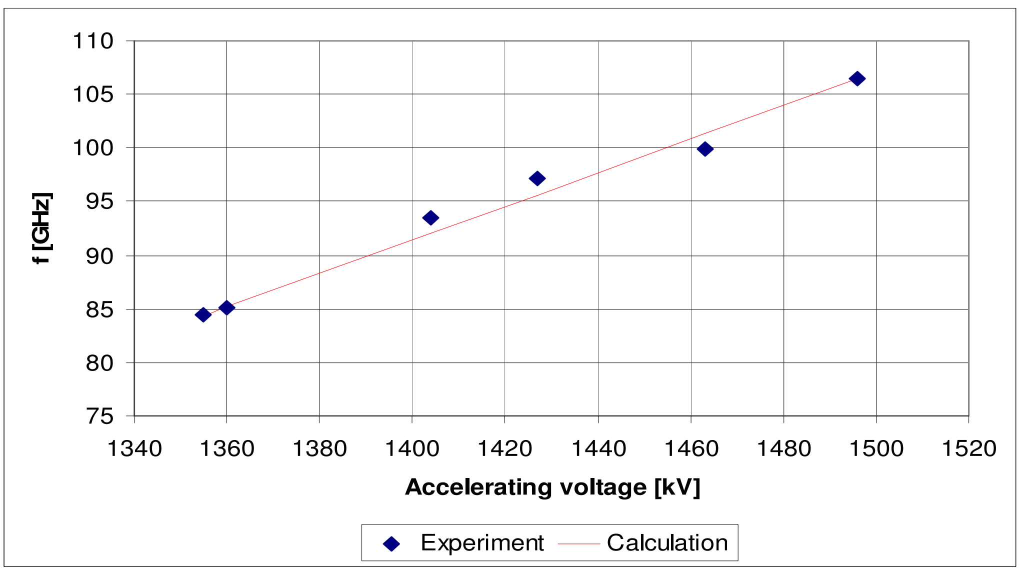

Fig. 6.4 FEL frequency tunability range

6.3 Chirp effect and the inherent spectral width at single mode lasing operation

The EA-FEL differs from other types of FEL primary in their capability shave a capability to operate with long electron beam pulses; their pulse duration is presently tens of microseconds long, much longer than the cavity recirculation time. Consequently, their spectral line width does not need to be Fourier-transform-limited, due to short pulse (micro-bunch) structure. Furthermore, since the FEL is a homogeneously broadened laser, a non-linear mode competition process, taking place at the saturation regime, normally drives the EA-FEL oscillator to single mode operation. Firstly single mode operation of the EA-FEL was demonstrated by (Elias et al 1986). Once single mode operation is attained, in an EA-FEL oscillator, the spectral linewidth is fundamentally limited by finite time Fourier transform broadening. These give extremely narrow linewidth limit, and a prospective for attaining a highly coherent and bright spectroscopic source tunable over a wide spectral region.

In this section we report measurements results of the EA-FEL single mode operation and inherent spectral width. The measurements are supported by the FEL3D simulations showing a good agreement with the measurements.

A single-mode lasing was observed in most measurements after a short period of 1 μs. This was expected because of the ''homogeneous broadening'' (Gover A. and Sprangle 1981) nature of FEL, in the cold beam regime. Figure 6.5 presents typical experimental data. On the oscilloscope screen the IF signals looks perfectly sinusoidal (Fig 6.5a) verifying the single mode operation during the laser pulse. However, this display does not slow small frequency variation (chirp) which is present in the radiation pulse spectrum. The chirp effect appears due to the electron beam current leading of the resonator. It is there are measured effect, but may possible be used for spectroscopic applications. For accurate measurement of the very narrow spectrum of the laser radiation we employed two different methods of data processing:

1) We performed the so-called *I/Q* analysis. The obtained oscilloscope signal was multiplied by $sin(\omega_0 t)$ and $cos(\omega_0 t)$, with ω_0 corresponding to an arbitrary chosen frequency (169.0 MHz). These multiplied signals I and Q were subjected to low-pass filters of 15 MHz bandwidth. Then, amplitude I^2+Q^2 and phase deviation

arctg(Q/I) were extracted, and the frequency deviation $\Delta f(t) = f - f_0$ was obtained (Fig 6.5a) as the time derivative of the phase deviation :

$$\Delta f(t) = \frac{1}{2\pi}\frac{d}{dt} arct\left[\frac{Q(t)}{I(t)}\right] \qquad (6.2)$$

2) To resolve the spectral evolution of the FEL, we employed a "running-window" fast Fourier transformation (FFT) on the IF signal. This time-frequency analysis performs a localized FFT on windowed section of the signal with spectral resolution of $\sim 1/\mathrm{T_w}$,where $\sim 1/\mathrm{T_w}$ is the (effective) window width.

The results of FEL3D simulation are presented in Fig. 6.5d. We define the inherent spectral width of the laser radiation as the linewidth of the wave when the spectral broadening due to the chirp is eliminated. To obtain the inherent spectral width we performed a linear time-stretching transformation $t' = t(1 + tf_1 / f_0)$. This eliminates the chirp from the chirped signal: $\sin[(\omega_0 + \omega_1 t)t] = \sin(\omega_0 t')$. The chirp rate parameter used was f_1= 0.35 MHz/μs as follows from the slope of the experimental curve in Fig. 6.5. The Fourier spectrum of the transformed signal is shown in Fig. 6.5c, exhibiting an inherent spectral linewidth (FWHM) of 0.2 MHz (in comparison with 2.0 MHz FWHM of the original chirped signal spectrum). The spectrum width is somewhat higher than the pulse-duration Fourier transform limited value (0.1 MHz) because the actual chirp is slightly nonlinear in time at the end of the pulse. The measured linewidth value of $\Delta \mathrm{f} / \mathrm{f} \cong 2 \cdot 10^{-6}$ is to our knowledge a record narrow linewidth measured until now for FELs. Based on theory a, narrower inherent linewidth (Socol Y. et. al 2005) value should be possible with longer pulse operation; this will allow very high resolution single pulse spectroscopy (see Chapter 7)

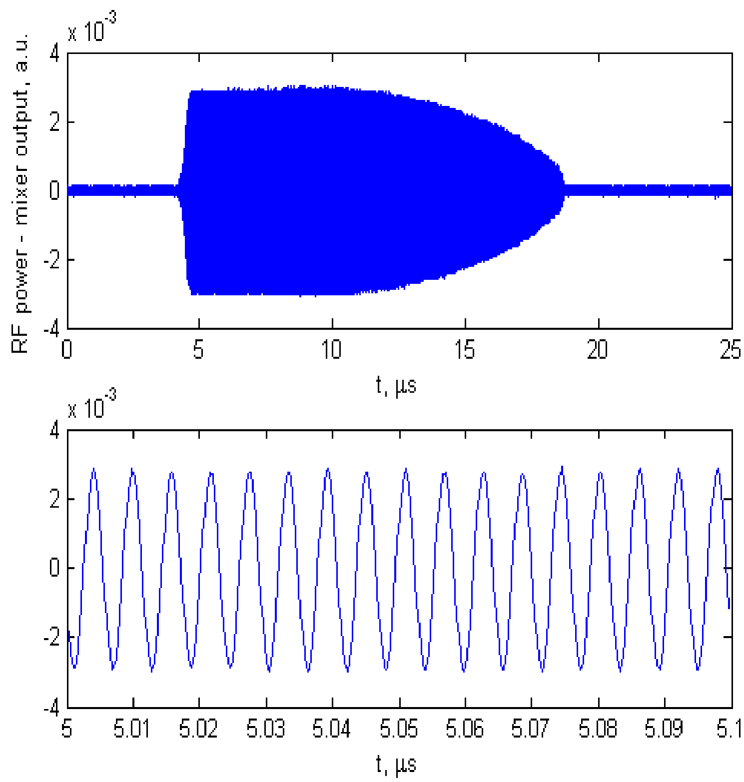

Fig. 6.5 (a) FEL Single-mode operation. Original oscillogram

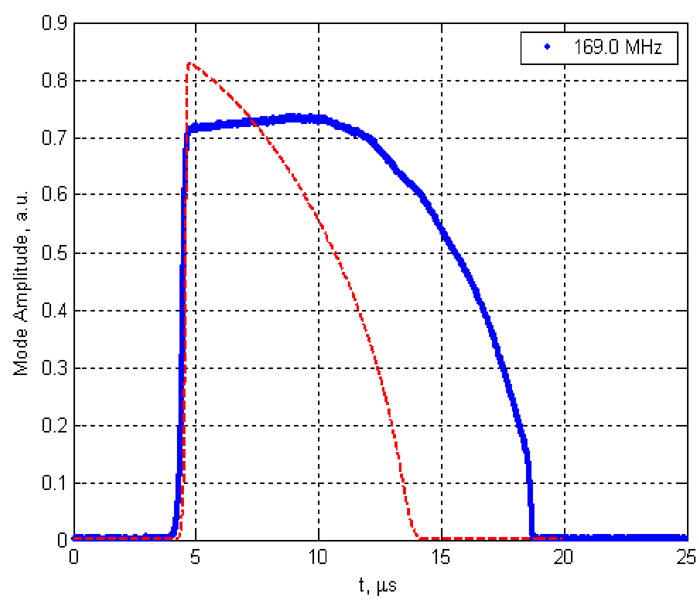

Fig. 6.5(b) Mode amplitude at single-mode operation.. The mode frequency is 84 401 MHz. In the I/Q analysis the low-pass filter is set to 15 MHz bandwidth

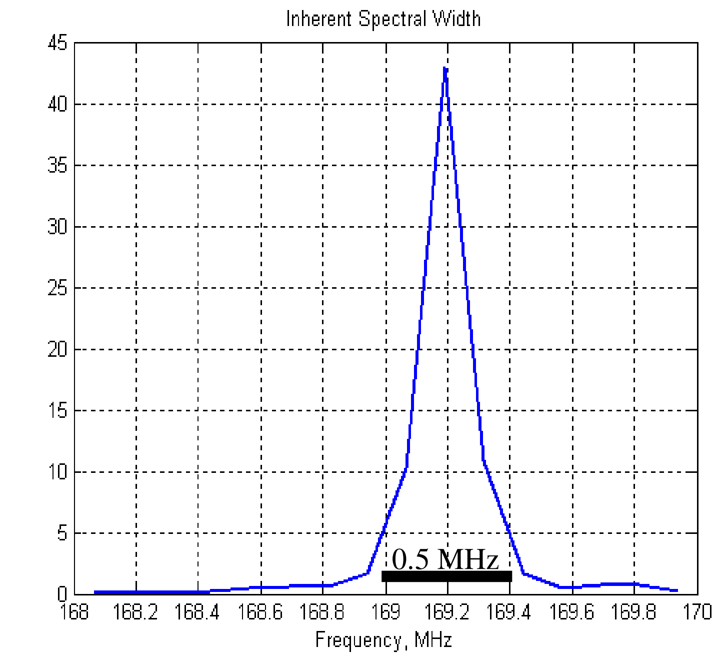

Fig. 6.5(c) Single-mode operation. Inherent spectral width, after numerical elimination of the chirp (0.2 MHz)

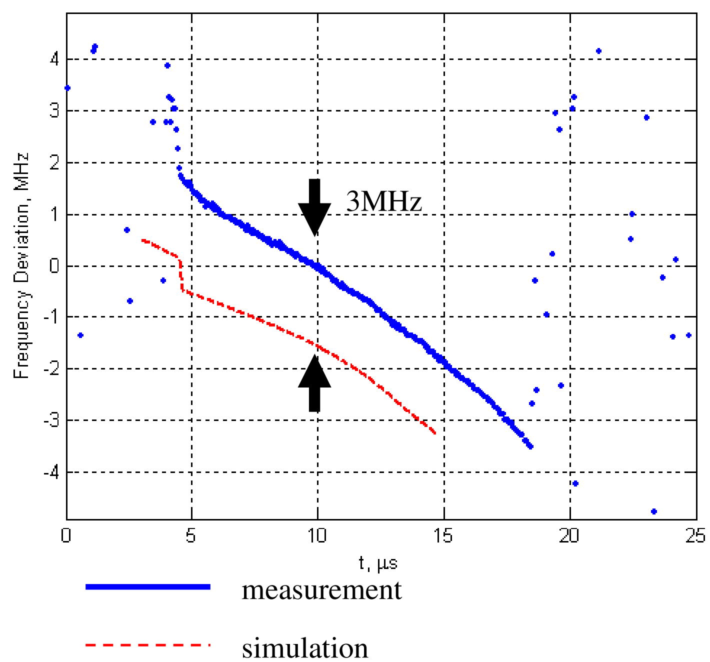

Fig. 6.5 (d) Single-mode operation. Momentary frequency deviation obtained by a time derivative of the phase deviation. Data measured (continuous line) and simulated (dotted line). The chirp rate is approximately 0.35 MHz/µs in both cases

In Fig. 6.6 we show a different ways of processing of the IF data. A spectrogram in the *ω-t* phase space was computed by employing a running window Fourier transform (Abramovich et al. 1999) of 1 μs width. This window makes it possible to observe the spectrum chirp, which agrees well with the 0.35 MHz/μs estimate, but the short time window used in our measurements limits the measurable bandwidth to 1 MHz correspondently to 1 μs window. We eliminated the chirp digitally by applying to the recorded data the time-stretching transformation described earlier, and used a time window of 10 μs to obtain the spectrogram of Fig. 6.6 (top). In this case, the bandwidth is window limited to 0.1 MHz, enabling the determination of the ‘‘inherent’’ mode linewidth as 0.27 MHz.

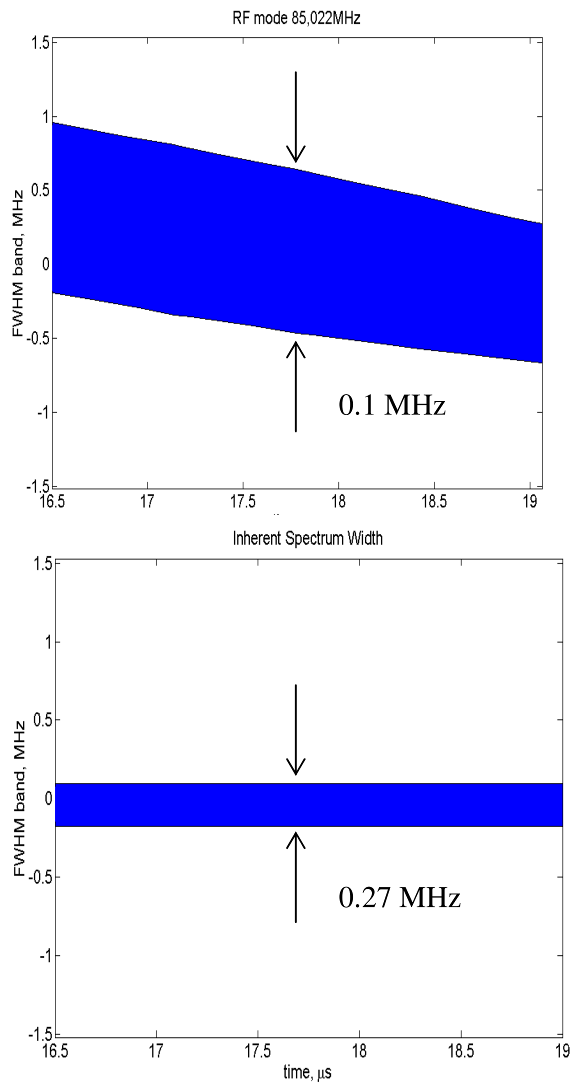

-

Fig 6.6 Spectral FWHM of a rf mode. Local oscillator frequency is 85 022 MHz. Top: initial data; bottom: after the digital chirp elimination. Time window is 1 and 10 µs respectively

6.4 Mode competition and mode hopping during lasing pulse due to high voltage droop

When the terminal voltage droop is moderate, the mode competition process winds up with single mode laser operation (Fig. 6.5b). However, if the droop rate is high enough, so that the gain curve drifts to lower frequencies until there is no net gain at the frequency of the built up laser mode, it decays, and new single mode may build up. Such dynamics observed in some cases (Fig. 6.7). It can be observed from the amplitude curves of the numerically filtered frequencies [Fig. 6.7(c)] that the first mode (85 021 5 MHz) decays when the second mode (83 676 5 MHz) grows.

We attribute this ''mode-hopping'' effect to large accelerating-voltage droop (Danly B. et. al 1990, Abramovich A. et.al. 1999, Urbanus W.1990). The voltage droop is due to electron beam current leakage at the high voltage (HV) terminal. The high voltage drift rate as measured by a capacitive pickup sensor was usually ~07–0.9 kV/μs, resulting in 7 to 30 kV voltage deducting during the observed pulses of 10–25 μs. We relate this phenomenon to what is called "relaxation oscillations" in quantum lasers (Yariv A. 1985). In a more general context this phenomenon may be connected also to ''load pull'' in the theory of nonlinear circuits (Itoh Y. and Honjo. K. 2003). In our case we observed a damped relaxation mode (see Landau L and Lifshitz E. 2003, Sec. 25) due to relatively high round-trip loss of the resonator. We should mention that our results were obtained using imperfect beam transport with a 1-stge collector. Future improvement of the electron beam transport may permit longer radiation pulses.

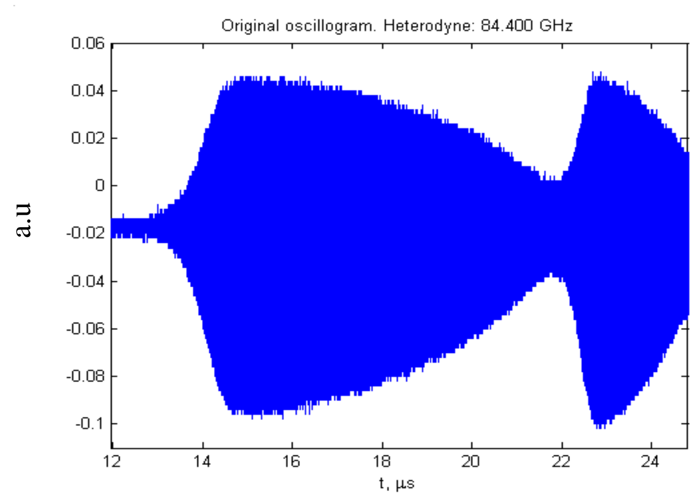

Fig.6.7a Mode hopping associated with the accelerator-voltage droop (IF data)

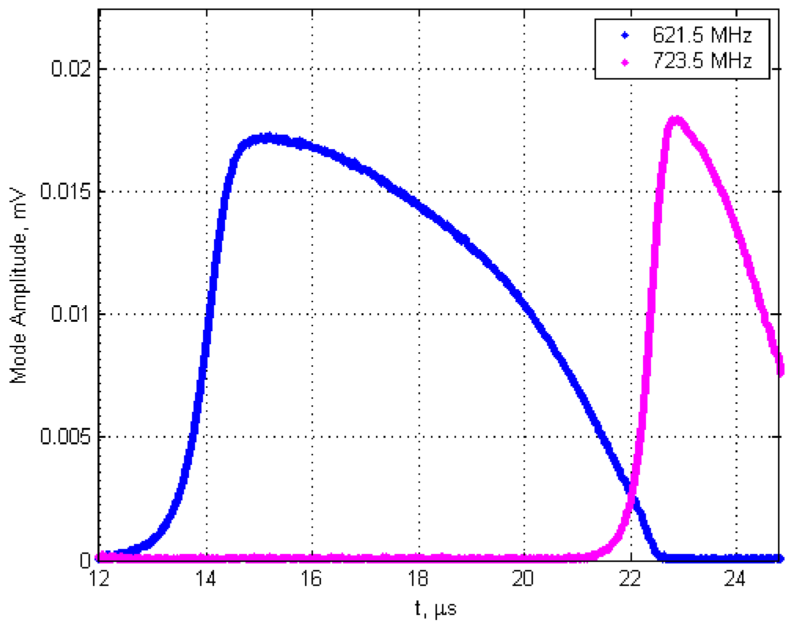

Fig.6.7b Mode hopping associated with the accelerating-voltage drop. Growth and decay of two modes

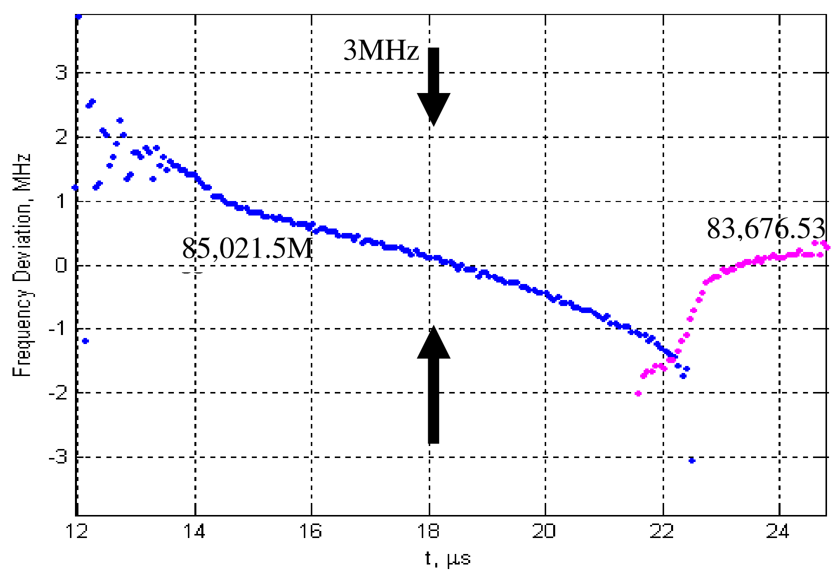

Fig.6.7c Mode hopping associated with the accelerating-voltage drop. Isolated frequency chirp measurement of the two modes (here $f_2 < f_{LO} < f_1$). The chirp direction in both modes is the same (frequency decreases with time). The chirp is seen as positive for the 83 676.5 MHz mode because the mode frequency f_m, is below that of the local oscillator f_{LO}: $f_m < f_{LO}$ =84 400 MHz. Therefore the intermediate frequency $f_{IF} = f_m - f_{LO}$ is negative (aliasing effect)

6.5 Measurements and calculations of the lasing frequency chirp during high voltage droop

In all measurements, the IF signal exhibited monotonous chirp (either negative or positive).In some cases, even within the same radiation pulse, the IF frequency chirp trend changed sign as in Fig. 6.7c. To explain this, note that the chirp of the laser frequency due to voltage droop should be always negative (because of the frequency pulling effect as explained next). However the IF chirp may appear negative or positive. The reason is that $f_{IF} = |f - f_{LO}|$ is defined positive. When f drops down, f_{IF} drops down with f as long as $f > f_{LO}$, but it grows up when f drops down when $f < f_{LO}$ (which appears a positive f_{IF} chirp). This aliasing effect is demonstrated by the experiment that is recorded in Fig. 6.9 and explained in Fig 6.8.

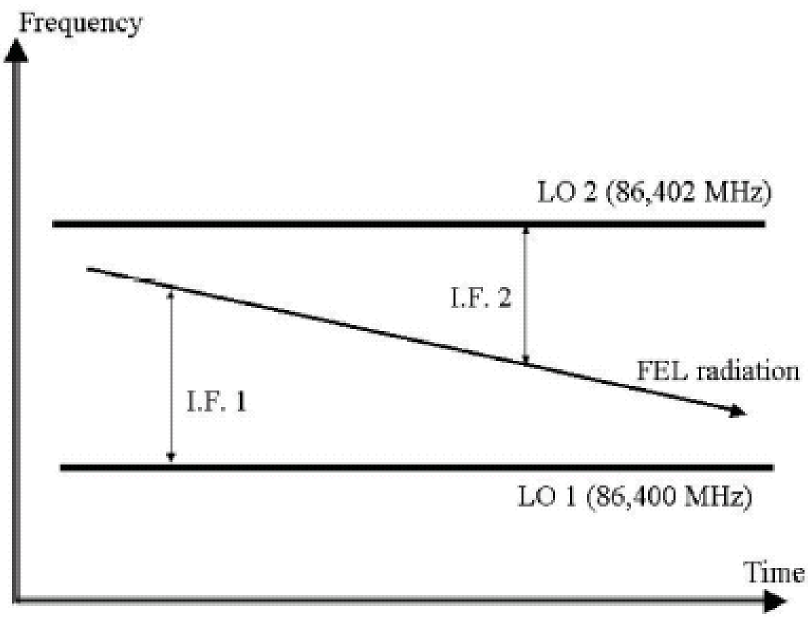

Fig. 6.8 Aliasing and chirp direction. If the radiation has negative chirp (frequency drops down with time), the intermediate frequency (IF) signal will exhibit negative chirp only when its frequency f is higher than that of the local oscillator (LO): $f > f_{LO}$. When $f < f_{LO}$ IF signal will exhibit a positive chirp

Figure 6.9 shows two oscillograms of the radiation, taken with the heterodyne mixer (LO) frequency set at two close frequencies: (a) 86 400 MHz and (b) 86 402 MHz, enabling the accurate determination of the single-mode radiation frequency f = 8 401 ± 1 MHz. At a heterodyne (local oscillator-LO) frequency f_{LO} = 86 400 MHz<f, the intermediate frequency (IF) decreases with time (left-hand oscilogram), and for f_{LO} = 86 402 MHz>f – the IF increases with time (right-hand oscilogram). Both measurements confirm, as expected, the negative direction of the laser chirp, i.e., that the laser radiation frequency decreases with time.

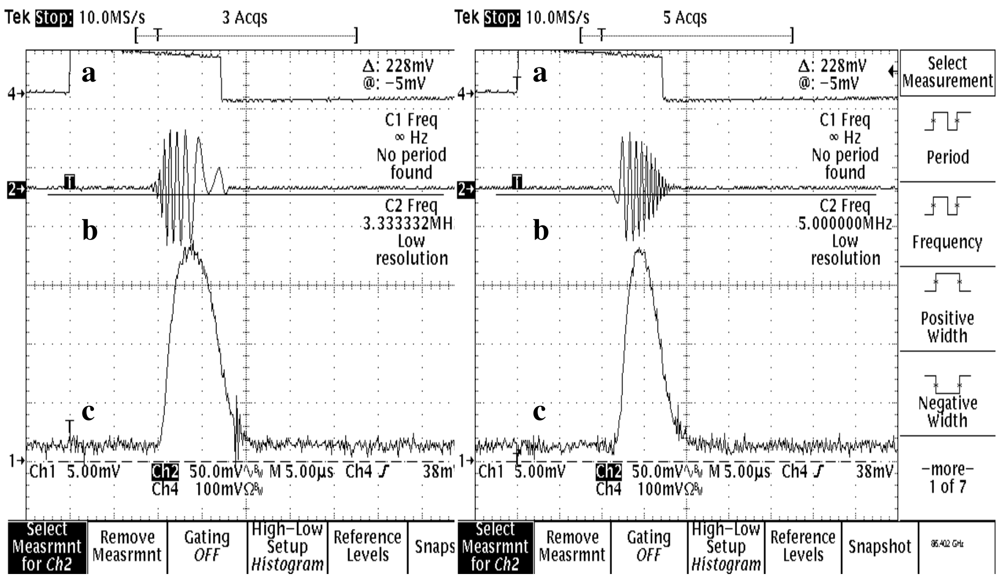

Fig. 6.9 Direct manifestation of the negative direction of the radiation chirp. Top trace: (a) e-beam current pulse. (b) heterodyne intermediate frequency (IF) output. (c) total W-band power. The local oscillator (LO) frequency f_{LO} is set very close to laser frequency: Left: f_{LO} = 86 400 MHz-the IF frequency decreases with time. Right: f_{LO} = 86 402 MHz-IF increases with time

We associate the exhibited down-shift frequency chirp effect with the drift of the gain curve due to the beam energy drop during the pulse (see Fig. 6.10.). The chirp can be explained then as a time varying ‘‘frequency-pulling’’ effect (Yariv A. 1985) of the laser oscillator.

We analyze here the chirp effect in terms of the basic theory of frequency pulling in laser oscillators

Namely, for resonator eigenmode frequency f_m, resonator mode linewidth (FWHM) $f_{1/2}$, maximum-gain frequency $f_{\max}$ and gain bandwidth Δf, the pulled oscillation frequency f:

$$f - f_m = \left(f_{\max} - f_m\right) \cdot \Delta f_{1/2} / \Delta f \tag{6.3}$$

In our case this frequency-pulling shift varies with time (chirps) due to the drift of the gain curve associated with the accelerator voltage drop during the pulse (Fig. 6.10).
The gain frequency drift rate is:

$$\frac{df_{\max}}{dt} = K \frac{dV}{dt} \tag{6.4}$$

where

$$K = \frac{e}{mc^2} \frac{df_{\max}}{d\gamma} \tag{6.5}$$

is the sensitivity of the maximum-gain frequency $f_{\max}$ to voltage drop. In a waveguide resonator the dependence of the maximum-gain frequency on beam energy is given by (5.21).

Calculating $d_{f\max}/d\gamma$ from the slope of the curve in Fig. 6.11 we evaluated Eq. (6.5) (high energy approximation) for our operating parameters: K = 156 MHz/kV. The FWHM bandwidth of the FEL gain Δf was calculated using the FEL3D code that performs 3D solution of particle motion equations coupled to Maxwell equations, using a space-frequency domain model. The calculations yielded Δf = 6.0 GHz. The resonator eigenmode linewidth $\Delta f_{1/2}$ was measured (in the ''cold'' resonator) to be $\Delta f_{1/2}=f_0/Q$=17 MHz (Q factor of 5 $\times 10^3$ at 86 GHz). The voltage drop rate was measured to be 0.7 kV/µs. The model-calculated chirp rate Eq. (6.3) is therefore:
df/dt = 0.3 MHz/μs.

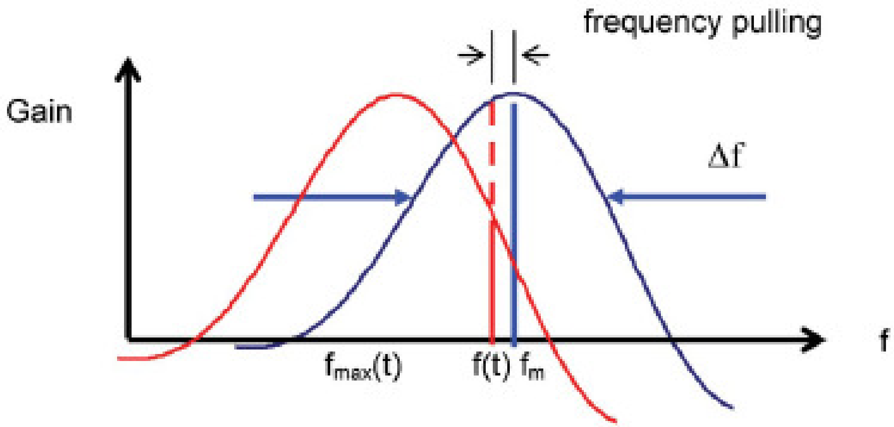

Fig. 6.10. The frequency-pulling effect. At t = t_1 (right-hand curve), it is assumed that the radiation is built up in the resonator so that the dominant mode m is excited at the maximum-gain frequency: f_m= $_{fmax}(0)$. As the gain curve shifts to lower frequencies (left-hand curve) $_{fmax}(t_2)$ < $f_{max}(t_1)$, there is a corresponding down-shift in the stored radiation frequency f <f_m due to the frequency-pulling effect

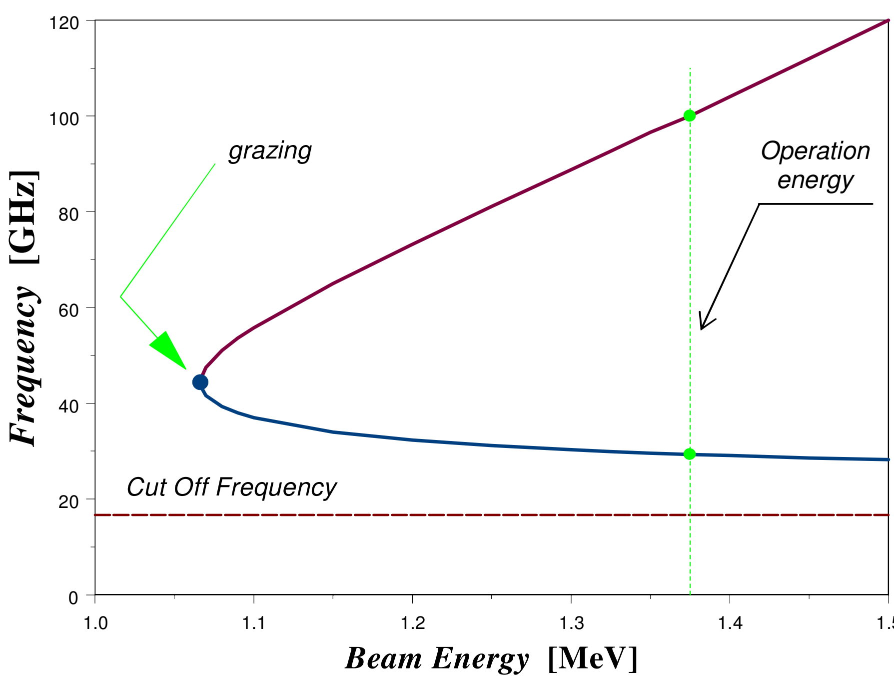

Fig. 6.11. Israeli FEL frequency dependence on the beam accelerating energy $(\gamma - 1)mc^2$

This value is in excellent correspondence with the experimental measurement, taking into account the limited accuracy of the parameters involved in the calculation:

$df/dt = 0.3$ MHz/μs

The experimentally measured chirp behavior agrees well also with results of FEL3D simulation (see Fig. 6.5d). The simulated instantaneous frequency (dashed curve) was calculated by evaluating the rate of phase accumulation change in each roundtrip traversal of the oscillation buildup (Pinhasi Y. 1995). The beam energy γ at each traversal was updated in the code in accordance to the measured voltage drop rate 0.7 kV/μs.

Chapter 7 Proposal for applications of post-saturation dynamics control in EA-FEL

We have seen that, HV terminal voltage droop in EA-FEL produces a frequency chirp in the emitted single mode lasing radiation. We believe that in future development of the EA-FL it may be possible to control the voltage droop rate and even reverse its trend (voltage ramping). Based on this observation we describe here two possible applications of such accelerator voltage control during the saturation:

(1) Speeding up the saturation process (in a finite pulse duration this provides a enhancement of energy extraction).
(2) Single pulse swept-frequency coherent spectroscopy.

7.1 Saturation process control in EA-FEL

We are looking for the efficiency and therefore power enhancement due to energy tapering for the parameters of the Israeli EA-FEL (we only describe an example of step energy ramping after saturation at lower energy). The oscillation build-up dynamics are presented in Fig. 7.1. All calculations were made using FEL3D for a single frequency. The result for a constant electron energy (1.42 MeV)) is shown in green. For the same frequency, the case of reaching early saturation at lower energy (higher gain), and then reaching higher saturation level with a single step increase of the electron energy is shown as the red curve. For an initial energy of 1.4 MeV saturation is obtained. Then after 50 round trips an electron beam energy increase step is applied (to 1.42 MeV). We see that if we start right away with the higher energy (green curve) the same saturation level is reached but only35 round trips later (because of the lower small signal gain of this higher energy). So we propose to use this method for speeding the build-up process to saturation in pulsed EA-FEL (Volshonok M et. al 2006). For finite pulse this enables achievement of enhancement of the EA-FEL energy extraction efficiency. In the Israeli EA-FEL it was impossible in present configuration to realize this experiment.

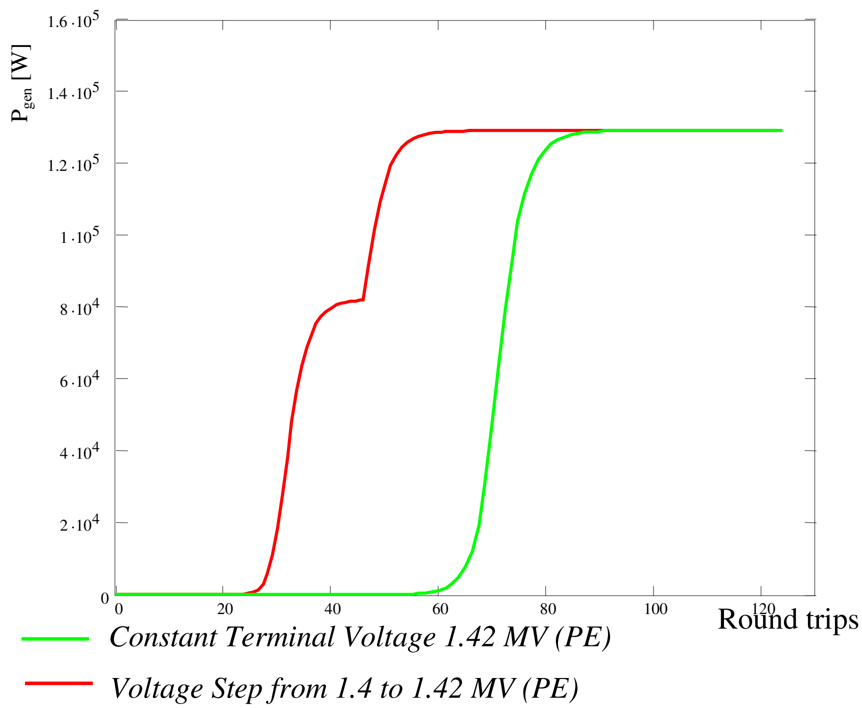

Fig. 7.1: The oscillation build-up in the EA-FEL with constant electron energy and with a step increase in the beam energy during the pulse after reaching saturation

7.2 A proposed single pulse sweep spectroscopic application with the EA-FEL

Since an EA-FEL can produce radiation pulse of extremely high inherent spectral purity (Socol et. al 2005), it may be used for spectroscopic applications. An interesting possibility is to perform single pulse spectroscopy-namely, to use the radiation chirp effect, observed and explained in section 5.8 as a frequency sweeper (Fig. 7.2). Let us estimate the feasible parameters for such an application.

For spectroscopic application there are two significant parameters: sweep range and spectral resolution. The sweep range depends on the frequency-pulling effect process. Based on Eq. (6.3) (see Fig. 7.2), the sweep (uniform chirp) range is

$$\Delta f_{sweep} = \Delta f_{hop} \Delta f_{1/2} / \Delta f \tag{7.1}$$

where the cold resonator FWHM linewidth is given for a Fabri-Perot resonator (Yariv A.1985); the notation is different there by

$$\Delta f_{1/2} \approx \Delta f_{FSR} (1 - R_{rt}) / 2\pi \tag{7.2}$$

Δf_{FSR} is the free spectral range between the modes of the resonator, and we assumed $1-R_{rt} << 1$ (R_{rt} is the round-trip reflectivity factor of the resonator including losses and out-coupling factors).

The parameter Δf_{hop} is the range of permissible shift of the FEL gain curve during the lasing pulse during which the lasing condition $g = (P_{out} - P_{in}) / P > 1 - R$ is retained, and beyond which the laser would hop and lase at a different resonator mode and frequency or would cease lasing altogether.

$$\Delta \mathrm{f}_{\mathrm{hop}} = \mathrm{f}_{\mathrm{max}} - \mathrm{f}\big|_{\mathrm{g=1-R}} \tag{7.3}$$

Clearly (see Fig. 7.2), this range is greater the higher the gain and the lower the factor $1-R_{rt}$. On the other hand the resonator mode linewidth $\Delta f_{1/2}$ Eq. (7.3) grows in proportion to $(1-R_{rt})$. There is therefore an optimal value of $1-R_{rt}$ for which Δf_{sweep} Eq. (7.2) can be maximized (in Fig. 7.2 it corresponds to a state of maximal area of the shaded rectangle).

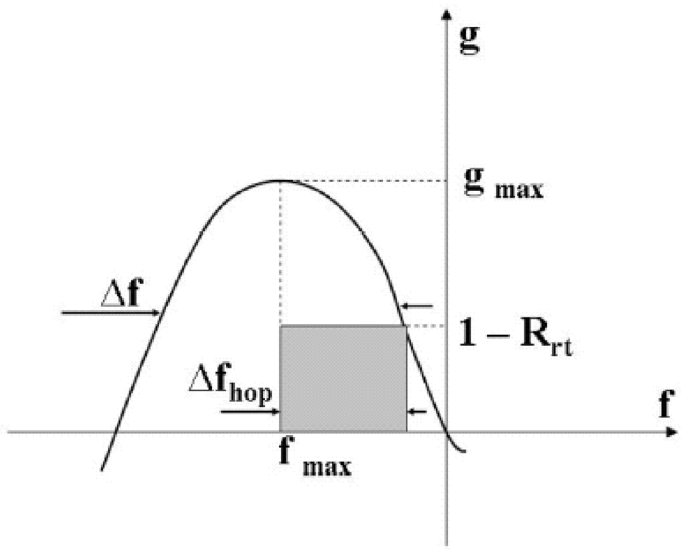

Fig. 7.2. Frequency shift Δf_{hop} is the range in which the lasing condition $g>1–R_{rt}$ is retained. Beyond this limit the laser would hop to lase at a different resonator mode or cease lasing altogether. This range is greater the higher the gain and the lower is the factor $1–R_{rt}$. The optimal value of $1–R_{rt}$ maximizing Δf_{sweep} corresponds to a state of maximal area of the shaded rectangle

In Fig. 7.3 we present the scaling of Δf_{sweep} as a function of the maximum gain g_{max} of the FEL (calculated numerically with FEL 3D), assuming operation in the low gain regime ($g<1$). The free spectral range used was the experimentally measured Δf_{FSR} = 115 MHz. Note that the experimentally measured chirp range ~3 MHz (see Fig. 6.5d) falls within the sweep range estimated in Fig. 7.3.

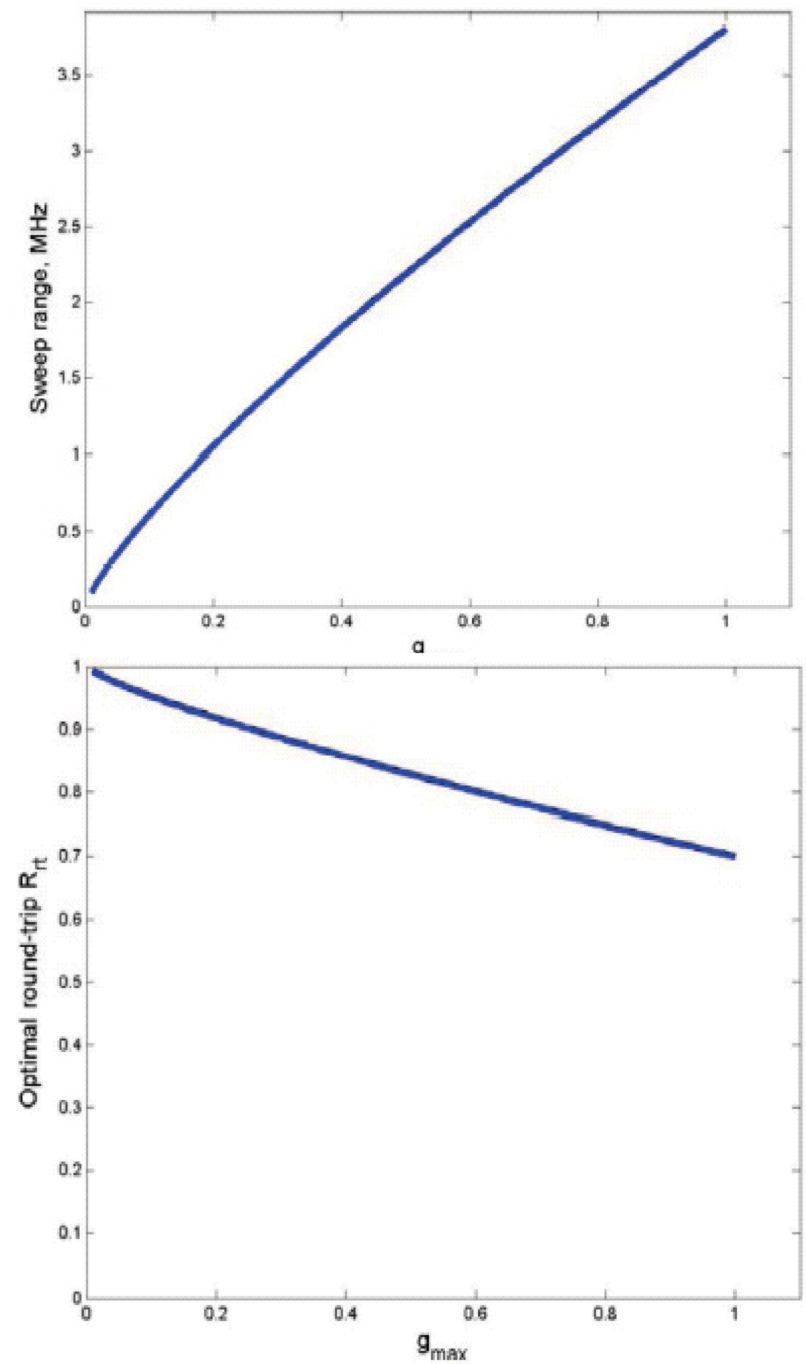

Fig. 7.3. The scaling of Δf_{sweep} and optimal round-trip reflectivity R_{rt} as functions of the maximum gain g_{max} of the FEL $g = (P_{out} - P_{in}) / P_{in}$, assuming operation in the low gain regime (g<1). The free spectral range used was the experimental measured Δf_{FSR} =115MHz. Note that the experimentally measured chirp range ~3 MHz see Fig. 6.5d) falls within the estimated sweep range

Another important parameter for spectroscopic applications is the spectral resolution. Here we distinguish between coherent and incoherent detection of the chirped FEL radiation signal and of the transmitted signal. In Fig. 7.4a the detection process is described in the time-frequency phase-space. The center frequency of the coherent radiation pulse $E_i(t)$ is chirped during the pulse time t_p:

$$f(t) = f_0 - f_1 t \tag{7.4}$$

where $f_1 = \Delta f_{\text{sweep}}/t_p$ is the chirp rate. The inherent spectral width of the FEL radiation is very narrow, and assumed to be Fourier transform limited:

$$\Delta f_{inh} = 1/t_p \tag{7.5}$$

When the FEL chirped radiation pulse is transmitted through an optical sample of complex transmission factor $t(f)$ and the optical power is detected (incoherent detection), the time dependence of the detected power replicates the transmission spectrum of the sample $t(f)$ (Figs. 7.4a and b). If we wish to resolve a resonant transmission line of the sample of width δf_{res} the sweep rate must be slow enough so that the sweep time through the transmission line $\delta t = f_1 \delta f_{\text{res}}$ is long (steady state approximation) relative to the polarization decay time $1/\delta f_{\text{res}}$ of the transmitted signal. This sets a limit on spectral resolution for incoherent detection:

$$\delta f_{res} = \sqrt{f_1} = \sqrt{\left(\Delta f_{sweep} / t_p\right)} \tag{7.6}$$

We can take advantage of our ability to detect coherently both the FEL incoming signal and the transmitted signal using heterodyne detection as described above Fig. 7.4c. Use of the full recorded data (amplitude and phase) of $E_i(t)$ and $E_0(t)$, the full (complex) value of the transmission factor $t(f)$ can be obtained after Fourier transformation $\mathbf{F}\{\}$ of the recorded signals

$$t(f) = \mathbf{F}\{E_0(t) / \mathbf{F}\{E_i(t)\} \tag{7.7}$$

The spectral resolution in this case is Fourier transform limited and given by the inherent linewidth value

$$\Delta f_{res} = 1/t_p \qquad (7.8)$$

Table 7.1 lists resolution limits for a sweep range of 5 MHz and several planned values of pulse duration for both the incoherent and coherent schemes.

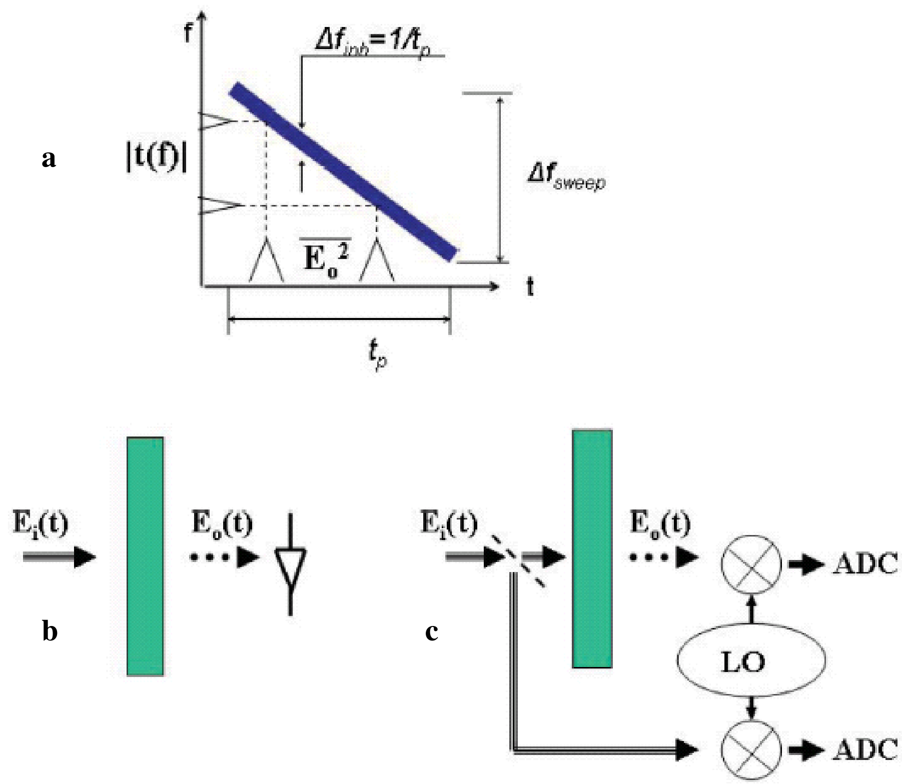

Fig. 7.4 (a) The detection process in time-frequency phase space. The center frequency of the coherent radiation pulse $E_i(t)$ is chirped during the pulse time t_p: $f(t) = f_0 - f_1 t, f_1 = \Delta f_{sweep} / t_p$ is the chirp rate. (b) Incoherent detection - the spectral resolution is low (see Table 7.1). (c) Coherent detection. LO is local oscillator, ADC is analog-to-digital converter. The spectral resolution is pulse time Fourier limited

Table 7.1 Resolution limits for a sweep range of 5 MHz and for several pulse duration times. For coherent measurements, the resolution is limited by the inherent linewidth. For incoherent, it is considerably worse and scales as the inverse square root of the pulse duration

Pulse time, μs	Sweep rate f', MHz/ μs Sweep range5 MHz	Resolution $\delta f_{res,}$ kHz	
		Coherent (complex)	Incoherent (scalar)
10	0.5	100	700
100	0.05	10	200
1000	0.005	1	70

Chapter 8 Summary and Conclusions

This thesis described experimental and theoretical research carried out on the Israeli EA-FEL. The experimental investigation was carried out in the FEL User Facility

The theoretical work was carried out with the aid of a number of computer codes (some existing and some developed by us).

Existing codes for the calculation of e beam transport such as the E-GUN, and GPT electron tracing codes have some limitations in their use. The GPT code does not enable electron transport calculation in electron guns .The E-GUN code can not provide electron beam transport calculation in structures with non cylindrical symmetry (i.e. also for our case). A new code that we developed GUNDIST to provide coupling between the E-GUN code and GPT code; the output E-GUN data is used as an input into GPT simulations thus enabling computation of electron beam transport for various geometries.

We also investigated electron beam transport inside the wiggler using the ELOP and the GPT codes. In order to pass the wiggler without betatron oscillation and scalloping, the electron beam has to be injected at the wiggler entrance with special initial conditions. Most computer codes use random phase-space distribution of the electrons as the initial electron distribution in the beam transport calculations Use of such of distribution requires a very large number of the electrons which significantly increases the computer calculation time. By use of an algorithm, developed in this work that allows use of a uniform electron distribution on the 4-D phase space ellipsoid we reduced the required calculation time by factor of about ten. The results obtained using our algorithm gave results which were in very good agreement with the results of the formerly used time consuming code. The simulation codes that we used for electron beam transport simulation provided results which were in good agreement with experiment data.

Computer simulations predicted that the FEL lasing frequency depends on the electron betatron oscillations inside the wiggler. By use of the ELOP code and previously developed analytical expressions we found, that non optimal electron beam injection into the wiggler leads to betatron oscillations and scalloping of the electron beam inside the wiggler. These in turn lead to a lasing frequency reduction and to a shift in the FEL tunability range to a lower frequency range.

We simulated and described the effect of space-charge on the electron beam transport in the high energy section of the FEL. This effect was not described in previous works. The space-charge effect in the FEL high energy section leads to electro beam betatron oscillation and scalloping, and affects the FEL gain, lasing frequency and tunability range.

The effect of electron beam emittance on the FEL gain was studied using the FEL 3D code and the GPT code. We used the GPT data as an input into the FEL 3D code which enabled to show the effect of emittance on FEL gain. We show that the non optimal electron beam transport, leads to the emittance grows and therefore to significant FEL gain reduction.

The electron beam transport was monitored experimentally using diagnostic screens, which allowed measurement of the electron beam cross-section. Pearson coils enabled measurement of the electron beam current at different positions along the beam line. The use of properly coupled simulation codes, described above, enabled simulation of the electron beam transport along the whole FEL beam-line. The electron beam cross-section dimensions along the beam-line were optimized using the same codes in order to insure beam transport free of betatron oscillations and of scalloping inside the wiggler region.

The performance and voltage-current characteristics of the electron gun were measured and compared to results given by the E-GUN simulation code. The stray magnetic fields in the injector section were measured and canceled by opposite magnetic fields in order to improve the electron beam transport in that section.

The electron beam emittance was measured in the FEL accelerator section using the “pepper pot technique” The measured data was used as and input parameter in the simulation codes described above.

Spontaneous and stimulation radiation power and the tunability range of the FEL were measured; the measurements correlated well with simulations.

Inherent spectrum width for optimal conditions was measured using a heterodyne technique. The measured line width value of $\Delta f / f \cong 2 \cdot 10^{-6}$ is to our knowledge a record narrow line width measured until now for FELs.

Mode competition during high voltage droop was observed experimentally as well as radiation frequency variation (chirp). These effects were predicted accurately by FEL 3D calculations.

We made proposals in regard to FEL efficiency enhancement and for chirp control. We proposed a scheme for enhancement of radiation energy and for higher power extraction by proper tapering of the FEL accelerating voltage. The proper tapering of beam energy as function of time is predicted on the basis of calculations performed using the pendulum approximation approach.

We also proposed spectroscopic application of EA-FELs

References

[1] A. Abramovich, et al., *Appl. Phys. Lett*. 71 (1997) 3776.

[2] A. Abramovich et al., *Nucl. Instrum. Methods Phys. Res.,*Sect. A 407, 16 (1998).

[3] A. Abramovich et al., *Phys. Rev. Lett*. 82, 5257 (1999).

[4] A. Abramovich, M. Canter, A. Gover, J. Sokolovski Y.Yakover, Y. Pinhasi I. Schnitzer, *J.* Shiloh, *, Phys.Rev. Lett.* 82 6774. (1999)

[5] A. Abamovich *PhD dissertation*, Tel-Aviv university (2001)

[6] A. Averbuch et. al., *Numerical Algorithms*, 15 287 (1997)

[7] M. Billardon et al., *Phys Rev. Lett*., 51, 1652 (1983)

[8] M.Cohen *PhD dissertation*, Tel-Aviv university (1995)

[9] D. Deacon et al., *Phys Rev. Lett*., 38, 892, (1977)

[10] B. G. Danly et al., *Phys. Rev. Lett*. 65, 2251 (1990).

[11] P. Efthimion *Phys. Rev. A*, 16, 633, (1977)

[12] L. Elias, *Nucl. Instrum. Meth. Phys. Res. A* 237, 203 (1985)

[13] L. Elias, et al., *IEEE J. of Quan. Elect.*, QE-23, 1470 (1987)

[14] L. Elias, *Phys Rev. Lett*., 36, 710, (1976)

[15] L. Elias, J. Ren-Chau Hu, G. Ramian, *SPIE* 453 (1983)

[16] L. Elias G.Ramain J. Hu J, A. Amir *Phys. Rev.Lett*., 57,424 (1986)

[17] B. Ferguson and X. C. Zhang, *Nat. Mater*. 1, 26 (2002).

[18] A. Gover, et al. *Basic design considerations for the free electron laser driven by electron beams from RF accelerators*, Ed. K. Button Academic Press (1984)

[19] A. Gover *Lasers*: *Free Electron Lasers*, *Encyclopedia of Modern Optics,* Elsevier, Oxford, (2005)

[20] V.L. Grananshtain, I.Alexoff, *High power microwave sources*, Artech House, Boston (1987)

[21] A.Gover., Friedman A., Drobot A. *Laser Focus World*, 95, October (1990)

[22] A. Gover, E. Jerby, H. Kleinman, I. Ben-Zvi, B.V. Elkonin,A. Fruchtman, J.S. Sokolowski, B. Mandelbaum, A.Rosenberg, J. Shiloh, G. Hazak, O. Shahal, *Nucl. Instr.and Meth. A* 296 720 (1990).

[23] A. Gover, Faingersh, A. Eliran, M. Volshonok,, *Nucl. Inst. and Meth in Phys. Res. A* 528, 23 (2004).

[24] A. Gover *et al.*, in Proceedings of the FEL 2005 Conference,

[25] A.Gover and Sprangle, *IEEE J. Quantum Electron*. 17 1196 (1981)

[26] A. Gover, A. Amir, L. Elias, *Phys. Rev. A 35,* 164 (1987)

[27] K.Hallbach, *Nucl. Instrum. Meth. Phys. Res. A* 169, 1 1980

[28] W.B. Herrmannsfeldt., *E-GUN Electron optics and gun design program*, Stanford Uviversity (1988)

[29] S. Humphries, *Charged particle beams,* A Wiley (1990)

[30] Y. Itoh and K. Honjo, *IEICE Trans. Electron.* E86C, 108 (2003).

[31] J. Jacson, *Classical Electrodynamics*, John Wily and sons, New Yorc, NY, (1962)

[32] E. Jerby, A. Gover, *IEEE J. Quantum Electron.* 21,1041 (1985).

[33] Z. Jiang *et al.*, Appl. Phys. Lett. 76, 3221 (2000).

[34] P. Kapitza, P.A.M Dirac, *Proc. Cambr. Phil. Soc*., 29, 297, (1933)

[35] B. Kapelevich, A. Faingersh, A. Gover, *Microwave and Optical technology Lett.* 36, 303, (2003)

[36] G. Kuliapanov, *Nucl. Instrum. Meth. Phys. Res. A* 296, 1 (1990)

[37] A. Kugel, *Msc Thesis* Tel-Aviv University (1996)

[38] I. Langmuir, *Positive Ion Currents from the Positive Column of Mercury Arcs Science*, Volume 58, Issue 1502, pp. 290-291(1923)

[39] L. D. Landau and E. M. Lifshitz, *Mechanics* Butterworth-Heinemann, Oxford, (2003), 3rd ed.

[40] S. Matsuyama, et al., *Nucl. Instrum. Meth. Phys. Res. A* 348, 34 (1994)

[41] T. Marshall et al. *Appl. Phys. Lett*. 31, 320, (1977)

[42] J. Madey *J. Appl. Pys*., 42 1906, (1971)

[43] I. Merhasin, A. Abramovich, Y. Pinhasi, A. Gover, *Nucl. Instrum. Meth. Phys. Res. A* 407, 350 (1998)

[44] H. Motz , Nakamura, *Annals of Physics*, 7, 84, (1959)

[45] H. Motz, R. Whitehurst *J. Appl. Phys*., 22 826 (1953)

[46] R. Pantell et al. *J. Quan. Elect*., 4 905, (1968)

[47] R. Palmer, *J. Appl. Phys*., 43 3014, (1972)

[48] R. Philips, *Trans. IRE El. Dev*., 7, 231, (1960)

[49] Y. Pinhasi, Yu. Lurie, *Phys. Rev. E* 65 026501 (2002).

[50] Y. Pinhasi, Yu. Lurie, A. Yahalom, *Nucl. Instr. and Meth. A* (2003),

[51] Y. Pinhasi, *Int. J. Electron*. 78, 581 (1995).

[52] W.H. Press et. al 1992. *Numerical recipes in C*, Cambridge University Press (1996)

[53] Pulsar, *General Particle tracer, User Manual* (2004)

[54] Saldin E. et al. *Nucl. Instrum. Meth. Phys. Res. A* 445, 178 (2000)

[55] Smith T., *Nucl. Instrum. Meth. Phys. Res. A* 296, 33 (1990)

[56] M. Tecimer, *PhD dissertation*, Tel-Aviv university (2004)

[57] THz Imaging and Sensing for Security Applications, *Proc. SPIE Int. Soc. Opt. Eng. Vol. 5070, edited by R. L. Hwuand D. L. Woolard SPIE-International Society for OpticalEngineering, Bellingham, WA*, (2003).

[58] W. H. Urbanus et al., *Phys. Rev. Lett*. 89, 214801 (2002).

[59] Valentini M. *PhD dissertation* FOM (1997)

[60] M. Volshonok, O. Adam, *FEL 2003* Conf. Proceeding

[61] M. Volshonok, E. Dyunin A. Gover, "*8th Israeli Conf. On Plasma Science and Applications, Ariel. 2005* Proceeding

[62] M. Volshonok, E. Dyunin A. Gover *resented at the 8th Israeli Conf. On Plasma Science and Applications, 2006, Ein-Gedi.* Proceeding

[63] M. Volshonok, :*FEL 2007* Conf. Proceeding

[64] I. Yakover, Y., Pinhasi A. Gover, *Nucl. Instrum. Meth. Phys. Res. A* 445, 260, (1996)

[65] A. Yariv, *Optical Electronics* Holt Rinehart and Winston,Austin, TX (1985), 3rd ed., Sec. 6.2-5.

Appendix A

GUNDIST simulation code (based on MATLAB)

```
function egun2gpt_fin(filename,N_Rays,N_e);
% Translates E-gun data to GPT input file
% see 'egun2gpt.m' for usage


MM=1e-3; % 1mm=1e-3 m

% Get data from E-gun file
filetxt=[filename,'.txt'];
data  =load(filetxt);
count =data(:,1);
Radius=data(:,3);
z     =data(:,4);
Energy=data(:,5);
alfa  =data(:,6);

smpl=sqrt(rand(N_e,1));
ray=ceil(smpl*N_Rays); % yields linear distr. of 'ray'

phi=rand(N_e,1)*2*pi;    % random angle

Energy_rest=511*10^3; %eV
gamma=Energy/Energy_rest+1;
beta=sqrt(gamma.^2-1)./gamma;



xe=Radius(ray).*cos(phi)*MM;
ye=Radius(ray).*sin(phi)*MM;
ze=z(ray)*MM;
betax=beta(ray).*sin(alfa(ray)).*cos(phi);
betay=beta(ray).*sin(alfa(ray)).*sin(phi);
betaz=beta(ray).*cos(alfa(ray));
GPT_data=[xe,ye,ze,betax,betay,betaz];

% Write data to GPT file
fmt='startpar("wcs","I", ';
fmt=[fmt,' %g*mm, %g*mm, %g*mm, %g, %g, %g); \n'];

fid=fopen([filename,'_gpt.in'],'wt');
fprintf(fid, fmt, GPT_data');
fclose(fid);
```

```
function egun2gpt_pre(filename,Num,Ray);
% Translate E-gun data to GPT data
% Insert pre_convert('filename', data nuber ,number of the rays)

fileout=[filename,'.out'];

filetxt=[filename,'.txt'];

fidin=fopen(fileout,'rt');
I=0;
Marker=0;
while (1)
   L=fgets(fidin);
   if(L==-1)
      disp('Error');break;
   end
     I=findstr(L,'Final');
     if (I>0)
       Marker=Marker+1;
       if (Marker==Num)
          fidout=fopen(filetxt,'wt');
          for count=1:Ray
             L=fgets(fidin);
             N=str2num(L);
             fprintf(fidout,' %g %g %g %g %g %g %g %g %g\n' ,N);
          end
          fclose(fidout);
          break
       end
     end
 end
fclose(fidin);
```

```
function egun2gpt(filename,Out_index,EGUN_rays,N_e);
% Converts E-GUN output data to GPT input file
% Usage: pre_convert('egun_file', Out, EGUN_rays,N_e)
% 'egun_file': *.out file name WITHOUT extension
% Out        : EGUN out-file may contain several data structures.
%              "Out" specifies which one to be taken.
% EGUN_rays  : N of rays in EGUN output
% N_e        : N of electrons in GPT input
% Example    : egun2gpt('ac43',2,25,48)
%              Reads 2-nd data structure from 'ac43.out'
%              and creates GPT file 'ac43_gpt.in',
%              starting 25 electrons
egun2gpt_pre(filename,Out_index,EGUN_rays);
egun2gpt_fin(filename,EGUN_rays,N_e);
delete([filename,'.txt']); % auxillary file, created by egun2gpt_pre
```

Appendix B

BEAMDIST simulation code (based on MATLAB)

```
% BEAMDIST: Algorithms for preparing sample electron distribution for ELOP

function BEAMDIST

Z0=-2680;              %Z  - start point [mm]
F=0;                   %F  - inverse of focusing length (mm^-1)(>0 if beam is focused, <0 - if beam is
defocused)
Xb=7.5;                %Xb - initial beam radius [mm]
Yb=7.5;                %Yb - initial beam radius [mm]
alfaXb=2.93;           %alfaXb -  half width initial angular spread
alfaYb=2.93;           %alfaYb - half width initial angular spread
F=F*1000;

plc='c:\ELOP\BEAMDIST.D';   %  common name of starting files

A(1)=Z0;
A(2)=0;
A(3)=0;
A(4)=0;
A(5)=0;
A(6)=0;
B=create_focus(F,A);
plcs=strcat(plc,'0');
save(plcs,'B','-ASCII');
N=5;
j_fail=1;
i1=0;
Q1(1:16,1:4)=0;
while i1<=sqrt(N)
   i2=0;
   while i2<=sqrt(N)
      i3=0;
      while i3<=sqrt(N)
         i4=0;
         while i4<=sqrt(N)
            if i1^2+i2^2+i3^2+i4^2==N
               Q=[i1 i2 i3 i4];
               j2=1;
               for k1=1:2
                  for k2=1:2
                     for k3=1:2
                        for k4=1:2
                           Z=[(-1)^k1,(-1)^k2,(-1)^k3,(-1)^k4];
                           Q1(j2,:)=Q.*Z;
                           j2=j2+1;
                        end
                     end
                  end
               end
               for j2=1:16
                  j3=j2+1;
                  flag=0;
                  while j3<=16
```

```
                if Q1(j3,:)==Q1(j2,:)
                    flag=1;
                end
                j3=j3+1;
            end
            if flag==0
                A(1)=Z0;
                A(2)=Q1(j2,1)*Xb/sqrt(N);
                A(3)=Q1(j2,2)*alfaXb/sqrt(N);
                A(4)=Q1(j2,3)*Yb/sqrt(N);
                A(5)=Q1(j2,4)*alfaYb/sqrt(N);
                A(6)=0;
                B=create_focus(F,A);
                plcs=strcat(plc,num2str(j_fail));
                save(plcs,'B','-ASCII');
                j_fail=j_fail+1;
            end
        end
      end
      i4=i4+1;
    end
    i3=i3+1;
  end
  i2=i2+1;
 end
 i1=i1+1;
end


function res=create_focus(F,A)
res(1)=A(1);
res(2)=A(2);
res(3)=A(3)-F*A(2);
res(4)=A(4);
res(5)=A(5)-F*A(4);
res(6)=A(6);
return
```

Appendix C

The procedure for determination of the wiggler "virtual entrance point"

Based on previously developed computer program: ELOP (Merhasin I. 1998), we summarize the procedure for calculating the e-beam dimensions at relevant locations along the transport line from the acceleration tube exit (screen S_1) , through the wiggler, up to the deceleration tube entrance.

The procedure is based on a model of a Gaussian (or Eliptical) distribution of a finite emittance e-beam in (x, y, α_x, α_y) phase space. Space charge effects are neglected (Gover et. al 1984).

In particular the best match for the saturation fields of the magnets was found to be:

Wiggler: B_{s0} = 8094 Gs

Long magnets: B_{s0} = 8480 Gs

The procedure for computing the electron beam is as follows:

1. The beam parameters preparation program is run to determine: X_w, r_{bx0}, r_{by0}.
2. The optimal center electron trajectory is found by running ELOP from starting point z=0 to z =-700 mm and z=+700 mm with initial conditions:

   $X(0) = -X_w, \quad \alpha_x(0) = 0, \quad Y(0) = 0, \quad \alpha_y(0) = 0$
3. The values of $X(0)$, and possibly the correction magnets parameters can be slightly changed until perfect on-axis propagation is obtained in and out of the wiggler.
4. ELOP is run from z = 0 to z = ± 700 for a given emittance value with initial beam parameters r_{bx0}, r_{by0} calculated in step 1. These parameters can also be slightly adjusted until scallop-free beam propagation (in both x and y dimensions) is obtained inside the wiggler.
5. The beam is now propagated up to the screens positions z (S2) = -719mm, z (S3) = + 813mm, and the optimal beam spot dimensions on the screens are determined. See Figs. 1,2.
6. The virtual waist size and position of the beam entering the wiggler is found by starting the beam from the final position (z = -719mm) of the previous ELOP run

and propagating it forward up to z ~ -500mm while all the wiggler magnets are extinguished. The waist sizes W_{0x}, W_{0y} and positions Z_{wx}, Z_{wy} can be measured accurately after reading the data of the drawing with Matlab or Mathematica. See Figs. 3, 4.

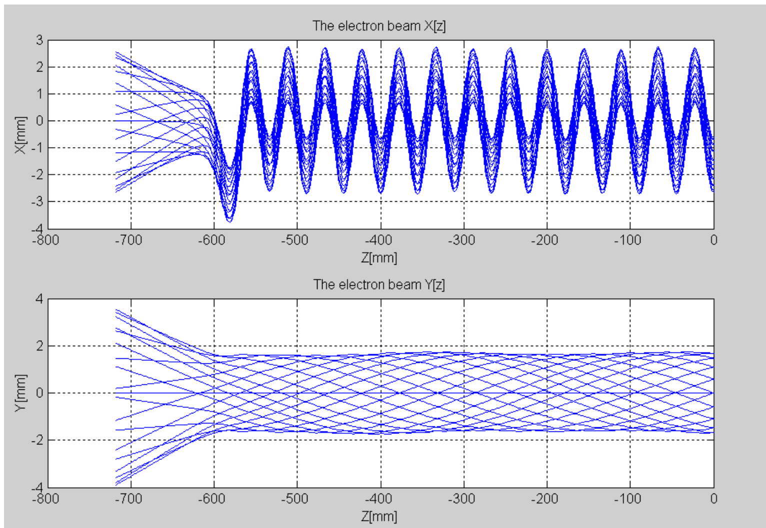

Fig.1 Beam diameter on S2. $\varnothing_X$=5.2mm, $\varnothing_Y$=7.5mm. Start point Z=0, end point Z=-719

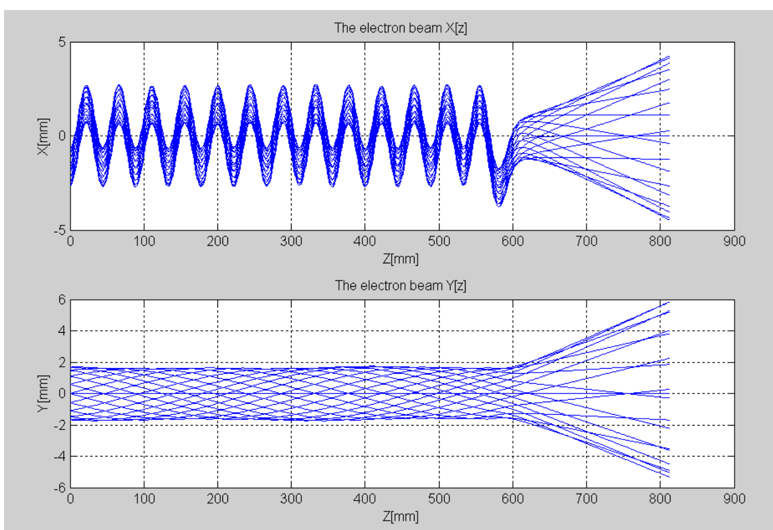

Fig.2 Beam diameter on S3. $\varnothing_X$=8.7mm, $\varnothing_Y$=11.2mm. Start point Z=0, end point Z=+813

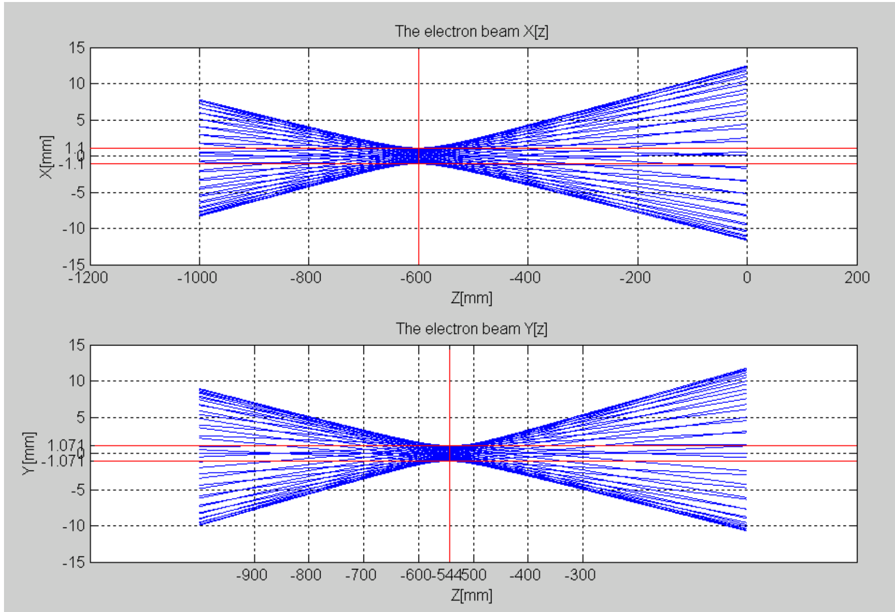

Fig.3 The beam virtual waist

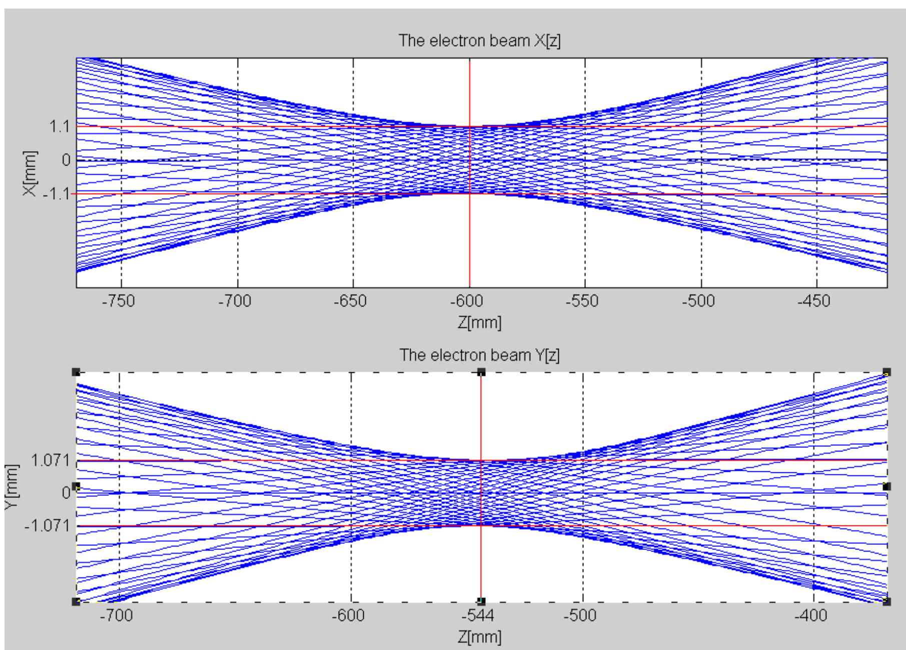

Fig.4 Determining the beam waist sizes $2 \cdot W_{0x}$=2.200mm, $2 \cdot W_{0y}$=2.142mm and waist positions Z_{wx}=-600mm, Z_{wy}=-544mm

Appendix D

<u>Comparison between GPT simulation and experiment in the acceleration section</u>

Table 1 The measurements of Dx made on S2 screen, (average error ~ 15%)

HV terminal voltage	Q1	Q2	Q3	Q4	Beam diameter, experiment DX	Beam diameter, simulation D	Error
[kV]	[A]	[A]	[A]	[A]	[mm]	[mm]	[%]
1428	0.405	-0.845	0.66	-0.19	4.41	3.49	20.86
1428	0.415	-0.845	0.66	-0.19	4.41	4.54	2.95
1427	0.415	-0.845	0.66	-0.19	4.41	4.69	6.35
1426	0.415	-0.845	0.66	-0.19	4.41	4.87	10.43
1420	0.405	-0.845	0.66	-0.19	3.78	4.04	6.88
1418	0.405	-0.845	0.66	-0.19	3.78	3.6	4.76
1426	0.405	-0.855	0.66	-0.19	3.15	3.33	5.71
1421	0.405	-0.855	0.66	-0.19	3.15	3.66	16.19
1413	0.405	-0.855	0.66	-0.19	3.15	3.34	6.03
1415	0.405	-0.835	0.66	-0.19	5.04	4.36	13.49
1425	0.405	-0.835	0.66	-0.19	5.67	4.4	22.4
1425	0.405	-0.845	0.66	-0.19	3.78	3.77	0.26
1424	0.405	-0.845	0.67	-0.19	3.36	3.74	11.31
1422	0.405	-0.845	0.65	-0.19	3.78	3.63	3.97
1425	0.405	-0.845	0.65	-0.19	4.095	3.75	8.4
1420	0.405	-0.845	0.66	-0.19	3.99	4.04	1.25
1418	0.405	-0.845	0.66	-0.2	3.15	3.89	23.49
1420	0.405	-0.845	0.66	-0.2	3.78	3.74	1.06
1422	0.405	-0.845	0.66	-0.18	3.78	4.03	6.61
1424	0.405	-0.845	0.66	-0.18	3.15	3.45	9.52
1426	0.405	-0.845	0.66	-0.18	4.41	3.6	18.37
1422	0.405	-0.845	0.66	-0.19	4.41	3.97	9.98
1425	0.405	-0.845	0.66	-0.19	4.41	3.77	14.51

1420	0.405	-0.845	0.66	-0.19	5.04	4.04	19.84
1421	0.415	-0.845	0.66	-0.19	4.41	5.11	15.87
1425	0.305	-0.845	0.66	-0.19	13.1	10.1	22.90
1425	0.405	-0.845	0.66	-0.19	5.04	3.77	25.2
1426	0.405	-0.845	0.66	-0.19	5.04	3.57	29.17
1425	0.405	-0.845	0.66	-0.19	5.04	3.77	25.2
1423	0.405	-0.845	0.66	-0.19	4.725	3.44	27.19
1423	0.415	-0.845	0.66	-0.19	3.78	4.58	21.16
1422	0.415	-0.845	0.66	-0.19	5.04	4.8	4.76
1424	0.415	-0.845	0.66	-0.19	5.04	4.76	5.55
1421	0.305	-0.845	0.66	-0.19	13.44	10.62	20.98
1420	0.405	-0.845	0.66	-0.19	4.41	3.44	21.99
1422	0.405	-0.845	0.66	-0.19	5.04	3.97	21.23
1423	0.405	-0.845	0.66	-0.19	4.41	3.44	21.99
1421	0.405	-0.845	0.66	-0.19	5.04	3.98	21.03
1420	0.405	-0.845	0.66	-0.19	5.04	4.04	19.84
1422	0.305	-0.845	0.66	-0.19	12.6	9.54	24.28
1421	0.305	-0.845	0.66	-0.19	14.5	10.62	26.75
1422	0.405	-0.845	0.66	-0.19	5.04	3.97	21.23
1414	0.405	-0.845	0.66	-0.19	5.04	3.85	23.61
1421	0.405	-0.845	0.66	-0.19	5.04	3.98	21.03
1417	0.405	-0.845	0.66	-0.29	5.04	3.68	26.98
1419	0.405	-0.845	0.66	-0.29	5.04	3.56	29.36
1423	0.405	-0.845	0.66	-0.29	3.78	3.56	5.82
1421	0.405	-0.845	0.66	-0.09	5.67	4.73	16.58
1422	0.405	-0.845	0.66	-0.09	6.3	4.53	28.09
1423	0.405	-0.845	0.66	-0.09	6.3	4.61	26.82
1421	0.405	-0.845	0.66	-0.19	5.67	3.98	29.80
1422	0.405	-0.845	0.66	-0.19	5.04	3.97	21.23

Table 2 The measurements made of Dx on S2 screen, (average error ~ 18%)

HV terminal voltage	Q1	Q2	Q3	Q4	Beam diameter, experiment DY	Beam diameter, simulation D	Error
[kV]	[A]	[A]	[A]	[A]	[mm]	[mm]	[%]
1428	0.405	-0.845	0.66	-0.19	8.825	8.73	1.08
1430	0.405	-0.845	0.66	-0.19	9.07	8.61	5.07
1428	0.415	-0.845	0.66	-0.19	9.07	7.37	18.74
1427	0.415	-0.845	0.66	-0.19	10.08	8.15	19.15
1426	0.415	-0.845	0.66	-0.19	10.08	7.72	23.41
1422	0.395	-0.845	0.66	-0.19	7.56	9.89	30.82
1425	0.395	-0.845	0.66	-0.19	8.06	10.4	29.03
1426	0.395	-0.845	0.66	-0.19	7.56	9.8	29.63
1420	0.405	-0.845	0.66	-0.19	7.305	8.42	15.26
1418	0.405	-0.845	0.66	-0.19	7.05	8.34	18.3
1421	0.405	-0.855	0.66	-0.19	9.07	10.3	13.56
1419	0.405	-0.835	0.66	-0.19	7.56	6.79	10.18
1415	0.405	-0.835	0.66	-0.19	7.05	7.42	5.25
1425	0.405	-0.835	0.66	-0.19	7.05	7.04	0.14
1425	0.405	-0.845	0.66	-0.19	7.39	8.58	16.10
1424	0.405	-0.845	0.67	-0.19	7.56	8.26	9.26
1425	0.405	-0.845	0.65	-0.19	7.555	8.94	18.33
1420	0.405	-0.845	0.66	-0.19	7.39	8.42	13.94
1418	0.405	-0.845	0.66	-0.2	7.56	8.41	11.24
1420	0.405	-0.845	0.66	-0.2	7.81	8.49	8.71
1422	0.405	-0.845	0.66	-0.18	8.06	8.72	8.19
1424	0.405	-0.845	0.66	-0.18	7.56	8.61	13.89
1426	0.405	-0.845	0.66	-0.18	7.56	8.83	16.8
1422	0.405	-0.845	0.66	-0.19	8.56	8.79	2.69
1425	0.405	-0.845	0.66	-0.19	7.805	8.58	9.93
1421	0.405	-0.845	0.66	-0.19	9.57	8.56	10.55
1423	0.405	-0.845	0.66	-0.19	8.06	8.76	8.68
1420	0.405	-0.845	0.66	-0.19	8.06	8.42	4.46
1421	0.415	-0.845	0.66	-0.19	8.73	7.31	16.26
1425	0.405	-0.845	0.66	-0.19	7.56	8.58	13.49
1423	0.405	-0.845	0.66	-0.19	8.57	8.76	2.22
1426	0.405	-0.845	0.66	-0.19	8.57	8.9	3.85

1425	0.405	-0.845	0.66	-0.19	7.56	8.58	13.49
1423	0.405	-0.845	0.66	-0.19	6.972	8.76	25.64
1423	0.415	-0.845	0.66	-0.19	10.1	7.7	23.76
1422	0.415	-0.845	0.66	-0.19	8.06	7.83	2.85
1424	0.415	-0.845	0.66	-0.19	8.06	7.44	7.69
1422	0.395	-0.845	0.66	-0.19	8.565	9.89	15.47
1423	0.395	-0.845	0.66	-0.19	8.06	9.81	21.71
1420	0.405	-0.845	0.66	-0.19	7.56	8.76	15.87
1422	0.405	-0.845	0.66	-0.19	7.555	8.79	16.35
1423	0.405	-0.845	0.66	-0.19	7.559	8.76	15.89
1421	0.405	-0.845	0.66	-0.19	7.56	8.56	13.23
1420	0.405	-0.845	0.66	-0.19	7.555	8.42	11.45
1422	0.405	-0.845	0.66	-0.19	8.06	8.79	9.05
1418	0.405	-0.845	0.66	-0.19	8.31	8.34	0.36
1424	0.405	-0.845	0.66	-0.19	7.56	9.72	28.57
1421	0.405	-0.845	0.66	-0.19	7.56	8.56	13.23
1423	0.405	-0.845	0.66	-0.19	8.06	8.76	8.68
1417	0.405	-0.845	0.66	-0.29	10.6	10.73	1.22
1419	0.405	-0.845	0.66	-0.29	10.6	10.17	4.06
1423	0.405	-0.845	0.66	-0.29	8.06	9.51	17.99
1421	0.405	-0.845	0.66	-0.19	7.05	8.56	21.42
1422	0.405	-0.845	0.66	-0.19	7.305	8.79	20.33

אוניברסיטת תל-אביב
הפקולטה להנדסה ע״ש איבי ואלדר פליישמן
בית הספר לתארים מתקדמים ע״ש זנדמן סליינר

הפעלה יציבה ויעילה בהספק גבוה של לייזר אלקטרונים חופשיים – בעל מאיץ אלקטרוסטאטי

חיבור לשם קבלת התואר ״דוקטור לפילוסופיה״

מארק וולשונוק

הוגש לסנט של אוניברסיטת תל-אביב

אייר תשע״א

אוניברסיטת תל-אביב
הפקולטה להנדסה ע״ש איבי ואלדר פליישמן
בית הספר לתארים מתקדמים ע״ש זנדמן סליינר

הפעלה יציבה ויעילה בהספק גבוה של לייזר אלקטרונים חופשיים – בעל מאיץ אלקטרוסטאטי

מארק וולשונוק

חיבור לשם קבלת התואר ״דוקטור לפילוסופיה״
הוגש לסנט של אוניברסיטת תל-אביב

עבודה זו נעשתה באוניברסיטת תל-אביב בפקולטה להנדסה
בהדרכת פרופ׳ **אברהם גובר**

אייר תשע״א

עבודה זו נעשתה

ב**אוניברסיטת תל-אביב**

ב**פקולטה להנדסה**

בהדרכת

פרופ' **אברהם גובר**

תקציר

מחקר תיאורטי וניסיוני בלייזר אלקטרונים חופשיים – בעל מאיץ אלקטרוסטאטי (EA-FEL) של אוניברסיטת תל-אביב והמרכז האוניברסיטאי אריאל - מוצג בעבודה זו. עבודה זו מתחילה בסקירה ספרותית של מתקני FEL כולל ה-EA-FEL הישראלי. עבודה זו כוללת מחקר תיאורטי וניסיוני של חלקי ה-EA-FEL כגון: תותח האלקטרונים (אנרגיה נמוכה), המאיץ האלקטרוסטאטי (אנרגיה גבוהה), קטע האצת האלקטרונים ואיסופם.

מהלך קרן האלקטרונים של EA-FEL על חלקיו השונים מנותח בסימולציות באמצעות מספר קודים שונים במטרה למצוא את פרמטרי ההפעלה למעבר אופטימלי של אלומת האלקטרונים במסלולה. התוצאות הניסיוניות נמצאו תואמות בצורה טובה את תוצאות הסימולציות המוקדמות.

מספר שיפורים בקוד הסימולציות מוצעים בעבודה זו על מנת לייעל את השימוש בו. השפעת איכות הולכת אלומת האלקטרונים על ההגבר, העוצמה ותדר הלזירה של ה – FEL נחקרה ומפורטת בעבודה זו.

בעבודה זו מתוארת העבודה הניסיונית והמדידות שנעשו ב – EA-FEL עם ווגלר 2kG ובמיוחד את אלו הקשורות בתותח האלקטרונים (45 kV/2A) ואלמנטי האלקטרון-אופטיקה במקטעים בעלי אנרגיה נמוכה וגבוהה. נמדדו השדות המגנטיים החיצוניים בתותח האלקטרונים. מדידות אלו סייעו בהערכת השינויים הנדרשים במסלול הקרן באינג׳קטור על מנת לשפר את הולכת אלומת האלקטרונים לתוך מקטע ההאצה.

בנוסף מתוארות מדידות ומחקר מסלול קרן האלקטרונים במאיץ, ונמדד פיזור הזוויות של אלומת האלקטרונים ($3\pi\cdot$mm$\cdot$mrad). חקרנו את השפעת פרמטרי הולכת קרן האלקטרונים, על הפליטה הספונטנית והמאולצת של עוצמת ה – FEL.

בנוסף, בוצעו מדידות ניסיוניות ומחקר תיאורטי על התהליך והתנאים לפעולה באופן יחיד וכתוצאה משינויים באנרגיית אלומת האלקטרונים בזמן הלזירה. רוחב ספקטרום הקרינה של האופן היחיד של קרינת הלייזר בזמן שינויי באנרגית האלומה נמדד (900W את 97.2GHz) , והתוצאות הניסיוניות הושוו לאלו שנחזו על ידי הסימולציות.

תחום התדרים האפשרי של EA-FEL הישראלי וההסחה בתדירות בזמן הפולס נמדדו אף הם את 80-110GHz. התלות של האפקטים הללו בקצב הירידה במתח הסופי נמדד והושווה לתוצאות הסימולציה.

מספר הצעות הועלו במטרה להגביר את עוצמת קרינת ה-FEL באמצעות שיפורים בהולכת אלומת האלקטרונים ושינוי מבוקר במתח במקטע המתח הגבוה כאשר הלייזר ברוויה. שימושים בשינויי מתח מבוקר בEA-FEL הישראלי (לקבלת קצב שינוי רצוי בתדר) לטובת אפליקציות ספקטרוסקופיות הוצעו.

תוכן עניינים